Title

Assembly of Extracellular Matrix Hydrogel Arrays and Phosphorylated Intrinsically Disordered Protein Brushes

Author

Lei, Ruoxing

Publication Date

2020

Peer reviewed|Thesis/dissertation

Assembly of Extracellular Matrix Hydrogel Arrays and Phosphorylated Intrinsically Disordered Protein Brushes

By

Ruoxing Lei

A dissertation submitted in partial satisfaction of the

requirements for the degree of

Doctor of Philosophy

in

Chemistry

in the

Graduate Division

of the

University of California, Berkeley

Committee in charge:

Professor Matthew B. Francis, Co-Chair
Professor Sanjay Kumar, Co-Chair
Professor Michael A. Marletta
Professor John E. Dueber

Spring 2020

Assembly of Extracellular Matrix Hydrogel Arrays and Phosphorylated Intrinsically Disordered Protein Brushes

By: Ruoxing Lei

Abstract

Assembly of Extracellular Matrix Hydrogel Arrays and Phosphorylated Intrinsically Disordered Protein Brushes

by

Ruoxing Lei

Doctor of Philosophy in Chemistry

University of California, Berkeley

Professor Sanjay Kumar, Co-Chair

Professor Matthew B. Francis, Co-Chair

Living cells sense and respond to the biophysical cues of extracellular matrix (ECM) in a complex and reciprocal manner. Towards a comprehensive understanding of the regulatory roles of matrix biophysical properties, there is an emerging need for high-throughput matrix platforms that enable parallel culture of cells in various matrix conditions, and for systems biology approaches that can investigate cell-ECM interactions in a parallelized fashion. We provide an overview of recent progress in developing synthetic biomaterial platforms to probe cell-ECM interactions in a high-throughput manner and to profile such interactions at the systems level. We then describe a multi-well hyaluronic acid (HA) array platform in which cells are cultured on combinatorial arrays of gels spanning a range of elasticities and adhesivities. We validated the platform by recapitulating expected relationships between matrix stiffness, adhesivity and cell mechanosensing in human mesenchymal stem cells (hMSCs). We also showed that on this platform, hMSCs maintain the capability of adipogenesis and osteogenesis, and inguinal white adipose tissue (WAT) cells were capable of developing into beige adipocytes. This hydrogel array platform provides a versatile tool for dissecting molecular mechanisms of cell-ECM interactions.

Intrinsically disordered proteins (IDPs) play central roles in numerous cellular processes. While the structure and function of many IDPs are regulated by multisite phosphorylation, biophysical insights into the relationship between the modifications and structure are limited. The challenge calls for paradigms in which IDP conformational responses can be measured in the context of controlled phosphorylation. By engineering the disordered neurofilament heavy subunit sidearm domain (NFH-SA), we established recombinant NFH-SA (rNFH-SA) brushes on glass that can be controllably phosphorylated *in situ* with pre-activated mitogen-activated protein kinase 1, and monitored brush conformations with atomic force microscopy. Phosphorylation induced significant brush swelling to an extent that strongly depends upon pH and ionic strength. The phosphorylated rNFH-SA brush was also dramatically condensed with micromolar concentrations of divalent cations. Our study demonstrates that multisite phosphorylation controls NFH-SA structure through modulation of chain electrostatics and points to a general strategy for engineering IDP-based interfaces that can be reversibly and dynamically modulated by enzymes.

Dedicated to my family and friends

Table of Contents

Acknowledgement

I would like to express my appreciation to my family, friends, mentors, and colleagues for their support during my 5 years of PhD studies at UC Berkeley. As the Covid-19 pandemic abruptly halted all research and disrupted life, I feel even more grateful that I have spent my graduate career here at Cal with so many wonderful people. These last few months of my PhD again reminded me of how fortunate I am to live and work in a supportive and inclusive community, especially during a global crisis.

Everything that I achieved in graduate school would have not been possible without the fundamental support from my advisor, Dr Sanjay Kumar. He took the great risk of accepting me into the lab and funding me, an international student from outside his department with no previous bioengineering background. He provided extensive mentorship as I stepped into the field of mechanobiology, of which I knew nothing before graduate school. He is always encouraging and inspiring, leading me through the scientific roadblocks with great insights from decades of expertise. In these last few months when we could not even meet in person, he continued to help with my writing and keep my graduation and upcoming transition on schedule. Sanjay has been a role model who has deeply affected me as a researcher and on a personal level.

I also appreciate all of my labmates and collaborators throughout my studies. Jess's mentorship gave me the foundation for starting in the lab and beginning the IDP project. Kayla has been a resourceful biomaterial expert, helping me through the hydrogel array project (and also training me in baking and cat-feeding skills outside the lab). Other senior members and postdocs including Elena, Mike, George, Jasmine, Joe, Phil and Stacey have all acted as great mentors on both research and non-research topics. Current members, Jieung, Junghwa, Andy, Eric, Erin, Kwasi, Emily, Vivien and Erika, are all fantastic colleagues and friends who have made lab routine a delightful experience. I enjoyed the collaboration with Garrett and Nicole on the array project as I learned so much exciting new science from them. It is also my pleasure to have mentored some brilliant undergraduate and rotation students, especially Kelly Wong, who helped lay the foundation of the array project. I give another special thanks to Kelsey and Katherine, who have both been awesome lab managers and kept everything running smoothly. While I do not have the chance to say goodbye to them in person, I miss the time we spent together and will remember everyone by heart.

I also thank my college research advisor, Dr Xing Chen, who is also a Berkeley Chemistry alumnus, for his mentorship and generous advice that helped prepare me for surviving graduate school. Thanks to the rigorous training that I received in the Chen Lab, my past research experience became an asset even after I switched to a different field.

It is my honor to have shared many marvelous memories with my Chinese friends at Berkeley: Xucheng, Luya, Xiang, Bingqi, Rui, Jing, Dan and Yicheng, and many more that I do not have space to mention here. We take care of each other like family members even when our real families are thousands of miles away. Finally, despite the geographic distance, my family in China continuous to support me. My greatest appreciation goes to my parents and my beloved husband, Haobo Yuan, for their unconditional love and trust across the Pacific Ocean for the past 5 years, which gave me courage and confidence to go through even the darkest moments.

Chapter 1

Getting the Big Picture of Cell-Matrix Interactions: High-Throughput Biomaterial Platforms and Systems-level Measurements

Abstract

Living cells interact with the extracellular matrix (ECM) in a complex and reciprocal manner. Much has been learned over the past few decades about cell-ECM interactions from targeted studies in which a specific matrix parameter (e.g. stiffness, adhesivity) has been varied across a few discrete values, or in which the level or activity of a protein is controlled in an isolated fashion. As the field moves forward, there is growing interest in addressing cell-matrix interactions from a *systems* perspective, which has spurred a new generation of matrix platforms capable of interrogating multiple ECM inputs in a combinatorial and parallelized fashion. Efforts are also actively underway to integrate specialized, synthetic ECM platforms with global measures of cell behaviors, including at the transcriptomic, proteomic and epigenomic levels. Here we review recent advances in both areas. We describe how new combinatorial ECM technologies are revealing unexpected crosstalk and nonlinearity in the relationship between cell phenotype and matrix properties. Similarly, efforts to integrate "omics" measurements with synthetic ECM platforms are illuminating how ECM properties can control cell biology in surprising and functionally important ways. We expect that advances in both areas will deepen the field's understanding of cell-ECM interactions and offer valuable insight into the design of biomaterials for specific biomedical applications.

A part of this chapter has been submitted as part of a peer-reviewed publication.

1.1. Introduction

Many cells within tissue are surrounded by a three-dimensional extracellular matrix (ECM), which is typically composed of proteins, polysaccharides, and proteoglycans. Historically, the ECM had been viewed as a passive scaffold that supports cell adhesion and tissue mechanics. However, it is now widely understood that the ECM profoundly regulates physiology and disease by providing a rich array of biophysical and biochemical cues that powerfully affect cell behavior.[1–4] The relationship between cells and the ECM is highly reciprocal, with cells deforming, digesting, and depositing matrix components. Cell-ECM interactions deeply regulate stem cell development,[5] tumor progression,[6,7] immune responses[8] and many other biological processes.

An important ongoing challenge in understanding and controlling cell-ECM interactions is the difficulty of presenting matrix cues to cells in a parallelized and multiplexed fashion, as is commonly done for soluble cues such as cytokines and small molecule effectors. The development of such platforms is as much a solid-state materials science problem as it is a cell biology problem, requiring combinatorial deployment of ECM-mimetic substrates of defined mechanics, adhesivity, and other properties. Moreover, while the synthetic ECM-mimetic materials used in culture platforms tend to be more scalable, tunable, and reproducible than their native counterparts, synthetic materials lack many of the structural and dynamic properties that regulate cell behavior in tissue.[9] Nonetheless, successful creation of combinatorial matrix platforms could both accelerate the field's understanding of cell-ECM crosstalk and serve as the basis for screening technologies.

In addition to permitting combinatorial presentation of ECM cues for discovery and screening, there is another level at which synthetic ECM fabrication and systems-level biology may be interfaced: The acquisition of high-content "omics" data from cells cultured on ECM scaffolds. Transcriptomic, proteomic, epigenomic, and other systems-level profiling in various ECM contexts all provide valuable high-level views of how matrix cues regulate biological processes such as metabolism, proliferation and apoptosis, both in normal and pathological systems. Systems-level measurements can often point to broad mechanistic patterns that are difficult or impossible to discern from candidate-focused studies. Synthetic ECM-mimetic materials have unique value in conducting omics measurements because they are typically more bio-inert than naturally-derived ECM materials, which contain a large number of both remnant cellular and ECM proteins.[10] However, obtaining these measurements in the context of synthetic ECM scaffolds is still non-trivial given that large cell numbers are often needed for statistical power and that DNA/RNA or protein sample extraction is difficult on 3D platforms since cells are much less accessible compared to those on 2D culture dishes.[11]

Despite these challenges, successful integration of synthetic matrix platforms and omics measurements is already yielding unprecedented mechanistic insight into cell-ECM interactions. In this review, we highlight recent progress in the development of high-throughput ECM platforms and in the application of systems biology to cells cultured in the context of synthetic biomaterials. We begin by discussing recently developed platforms that incorporate either single or combinatorial gradients of biophysical cues including matrix elasticity, ECM ligands and topography. We then focus on transcriptomic, proteomic and epigenomic level studies in mechanosensing events using biomaterial platforms.

1.2. High-throughput Biomaterial Platforms for Probing Cell-ECM Interactions

Broadly speaking, we focus on two varieties of high-throughput ECM platforms in this review: First, we consider platforms in which one ECM biophysical property is systematically varied, often with the goal of decoupling the regulatory effects of this property from others. Another important objective of these platforms is to sample many more property values than would normally be possible with individually fabricated materials, so as to more quantitatively capture how the material property influences cell behavior (e.g. linear vs. nonlinear relationship). We will focus on platforms with varying stiffness and surface topography as both properties have been heavily studied using synthetic biomaterials. Second, we consider combinatorial platforms, where the aim is to deploy two or more biophysical cues in a single platform, with the goal of identifying synergies or other relationships between the parameters. Both types of platforms can provide valuable insight for understanding cell mechanobiology and guiding cell and tissue engineering.

For systems in which a single ECM parameter is systematically varied, ECM stiffness is a natural focal point given the importance of ECM viscoelastic properties in controlling cell growth and death,[12–14] stem cell differentiation[15–17] and morphogenesis.[18–20] Stiffness gradients are ubiquitous in tissue physiology and disease, such as the transition between soft tissues to bone in joints and the interface between normal and tumor tissue. [21,22] Polymer hydrogels are a common scaffold for parallel deployment of a range of ECM stiffnesses within a single matrix material. Techniques such as photopatterning, layer-stacking, microfluidics and microprinting may be used to spatially control crosslinking level, thus generating stiffness gradients in the hydrogels. These fabrication approaches have been reviewed at length elsewhere.[23,24]

Recent trends in developing stiffness gradient hydrogels include achieving precise control of stiffness distribution as a function of location and designing complex gradients intended to more closely mimic tissue structures. A double polymerization process was recently introduced to create spatially linear stiffness distributions.[25] The hydrogel was composed of two sequentially polymerized, ramp-shaped acrylamide/bisacrylamide components, where the slope of the stiffness gradient was tuned by altering the percentage of acrylamide or bisacrylamide. This platform captured nonlinear relationships between stiffness and the localization of stiffness-sensitive proteins such as YAP, MRTF-A and MRTF-B in human adipose-derived mesenchymal stem cells (MSCs). Another system featured a two-layered polyacrylamide (PA) gel hybrid, in which the corrugated, fiber-like topography of the underlying hydrogel created effective mechanical gradients at the surface of the flat, superficial layer.[26] In this system, cells migrated parallel to the axis of the underlying fibers, which recapitulated ECM fiber-mediated contact guidance seen in tissue. Electrospinning has also recently emerged as a valuable tool for fabrication of parallelized ECM arrays, as exemplified by a recent study in which electrospun dextran vinyl sulfone (DexVS) fibers were arrayed into matrices with varying stiffness.[27] In contrast to non-fibrous culture substrates where soft matrices typically suppress cell spreading, fibroblasts in soft and deformable fibrous matrices exhibited increased spreading and focal adhesion formation. This observation is consistent with past studies indicating that nominally soft, fibrous ECMs

can promote a stiff-ECM phenotype if cells are allowed to remodel and bundle the constituent fibers to create a locally stiff environment.[28,29]

Surface topography determines how adhesion ligands align and are presented on the ECM, which significantly affects cell adhesion and tension [30] Topographically patterned biomaterials are widely used in tissue engineering to direct cell differentiation, migration, and morphogenesis.[31] For example, surfaces microtextured with poly(lactose-co-glycolide) pillars of various heights and spacings were recently applied to control the differentiation of rat MSCs. The use of tall micropillars produced sharp, "piercing" nuclear deformations, which in turn correlated with greater osteogenic and less adipogenic differentiation.[32] Topographically patterned ECM fabricated from dip-coated catecholic polyglycerol-based substrates have revealed a biphasic relationship between MSC osteogenic efficiency and interfacial roughness, with the roughness of optimal osteogenesis also maximizing nuclear YAP localization.[33] There is great interest in incorporating topographically patterned substrates into standard multi-well culture plates to facilitate bioassays. In one such effort, various "trench-grid" topographies were deployed in a 96-well plate platform to screen effects on T cell growth and function. An optimal geometry was identified that maximized T cell interleukin 2 secretion, particularly when coupled with pharmacologic inhibition of myosin II.[34]

There are many other examples of platforms for topographical control that employ polymer microfabrication techniques and thus have great potential for scaleup. We recently introduced a polydimethylsiloxane (PDMS) microchannel platform that allows contact-based AFM measurement of mechanical properties of cells migrating through confined spaces. Using this system, we showed that cells soften and rearrange their actomyosin networks as they squeeze through constructions.[35] In an important innovation relative to traditional, static ECM platforms, an optical embossing technique was recently exploited to create circular topographic patterns on azopolymer films while cells were migrating on these films. Cells showed evidence of adapting to newly introduced topographical features within two hours.[36]

Combinatorial platforms incorporate more than one ECM properties orthogonally on a single device to investigate the coupling effects of multiple cues on directing cell behaviors. Stiffness and adhesive ligand density are two properties that have perhaps received the most attention in these applications, in part because both often synergistically impact cell adhesion, migration, and other phenotypes.[37,38] Conducting photochemistry in ECM hydrogels through gradient photomasks is a versatile and effective way of creating spatial gradients within materials.[39] Often, the polymer backbone is decorated with photoreactive moieties and then exposed to UV or visible light in the presence of a gradient photomask to create gradients within the hydrogel. We developed a 2D hydrogel platform based on methacrylated hyaluronic acid (HA) modified with a UV-sensitive moiety, 4,5-dimethoxy 2-nitrobenzyl-aminothiol (DMNBAT), allowing orthogonal photoreactions triggered by UV and white light.[40] UV radiation through a printed photomask cleaved the DMNBAT groups to release free thiols for ECM protein conjugation, while transmitting white light through an orthogonally rotated photomask induced crosslinking between methacrylate groups to form a stiffness gradient (Figure 1.1A). We used this this platform to show that ECM stiffness and fibronectin density interact to regulate expression of miR18a, an oncogenic microRNA in

glioma cells (Figure 1.1B&C). By varying stiffness and ligand density in parallel, we were able to uncover unexpected inter-parameter interactions. For example, stiffness influenced miR18a expression at all fibronectin densities examined, whereas fibronectin density modulated miR18a only on stiff substrates. Combinatorial hydrogels may use a single photosensitive moiety if excess unreacted sites from the first round can further react in the second round. This strategy has been used with norbornene groups as the only reactive "handles" in both rounds of photopatterning.[41,42] Matrix stiffness and adhesive properties can also be controlled without photopatterning; for example, plasma oxidation has been used to introduce stiffness and wettability gradients to surfaces, which indirectly modulate protein adsorption.[43] Using this platform, the authors revealed distinct non-linear relationships between the engineered material properties and human MSC adhesion, spreading, nuclear size, and vinculin expression.

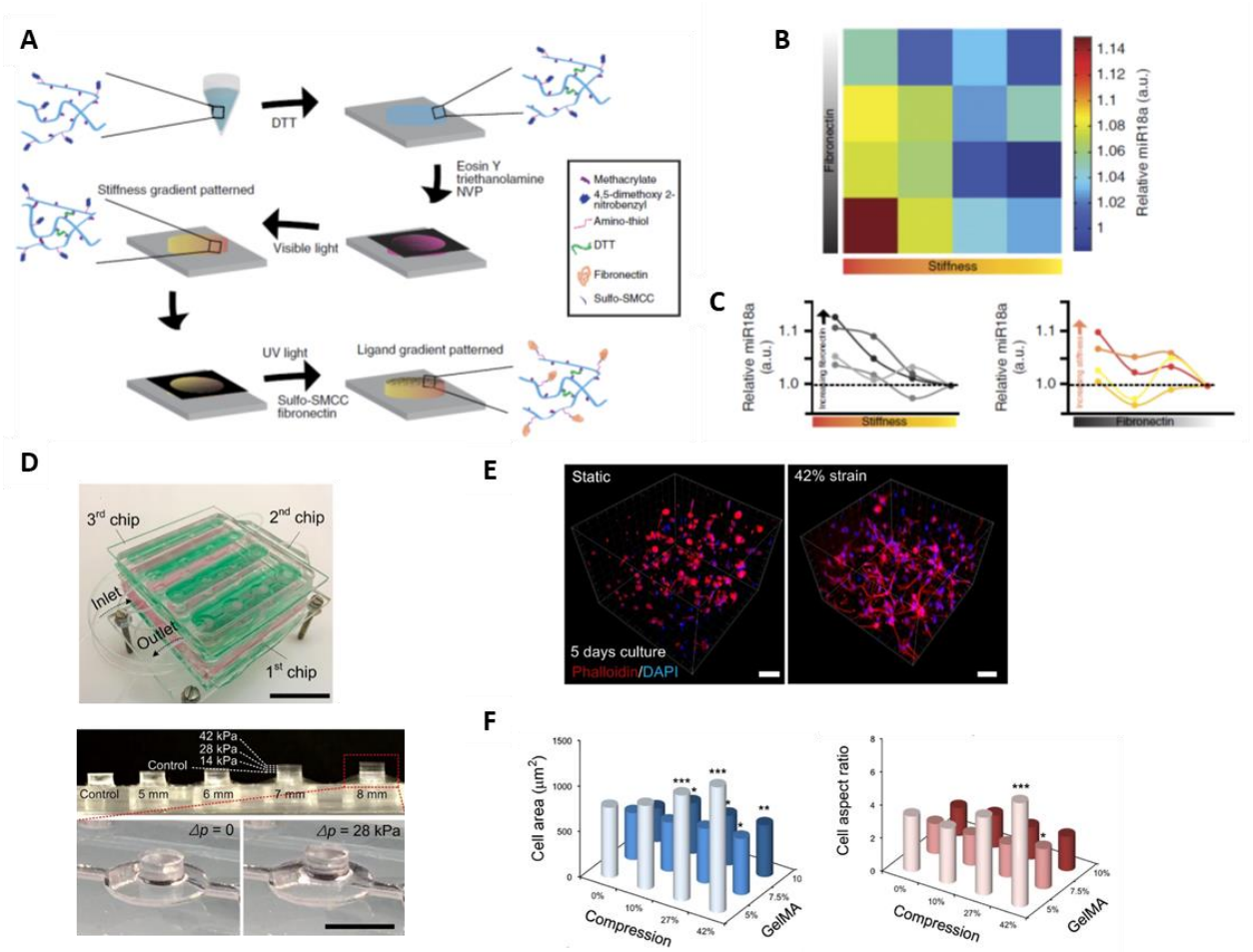

Figure 1.1. Combinatorial hydrogel platforms for studying cell responses to stiffness and adhesivity (A–C) or hydrogel composition and compression forces (D–F). (A) Dual gradient patterning of DMNBAT-HA-methacrylate hydrogel. (B) Heat map showing miR18a expression levels at 16 matrix stiffness-ligand combinations. (C) Iso-fibronectin curves (left) show that substrate stiffness regulates miR18a expression at all fibronectin densities tested. Similarly, iso-stiffness curves (right) show that fibronectin density only regulates miR18a expression at high

stiffness. (D) Photographs of a platform in which cells are placed in interconnected bioreactors (top) and subjected to mechanical force thorugh displacement of pressure-controlled posts (bottom). Scale bars = 5 mm (E) 3D reconstructed confocal photomicrographs of hMSCs in 5% GelMA hydrogel cultured under different strains. Scale bars = 100 μm. (F) 5% GelMA with 42% compression is optimal for cell spreading and elongation. (A–C) adapted with permission from Rape et al.[40] (D–F) adapted with permission from Seo et al.[44] Copyright (2018) American Chemical Society.

While most of the studies described above focus exclusively on modulating material properties, some approaches superimpose external dynamic mechanical loads on cells cultured on defined ECMs. In one notable example, coupling between biomaterial composition and dynamic mechanical compression in regulating human MSC osteogenesis was examined in 3D hydrogels.[44] Here, actuating posts were used to apply gradients of cyclic compressive strain, and GelMA concentration was used to vary ECM mechanics (Figure 1.1D). The authors found that a low percentage (5%) of GelMA coupled with a high magnitude (42%) of dynamic compression provided the optimal combination for cell spreading and osteogenic differentiation (Figure 1.1E&F), suggesting a coupling effect between hydrogel pore size and compressive strain. In another example, 3D miniaturized porous biomaterials were modified with 31 different protein formulations present in bone ECM, cell-cell junctions, and enamel and subsequently subjected to flow. This approach captured unexpected interplay between protein composition and dynamic flow in regulating MSC adhesion and alkaline phosphatase production.[45]

1.3. High-Throughput System Biology Analysis of Cell Mechanobiology on Biomaterial Platforms

Cell-ECM interactions can influence a wide variety of transcriptomic, proteomic, and epigenomic programs that can be challenging or impossible to appreciate from candidate-based studies. Therefore, it is important to integrate engineered biomaterials with systems-level measurements as a first step in understanding how ECM control and influence cellular responses.[46–49] We next highlight recent work on measuring how ECM biophysical properties influence transcriptomic programs, both at the level of mRNAs and non-coding RNAs. We also discuss more nascent but extremely promising efforts to extend these efforts to proteomic and epigenomic analysis.

To gain mechanistic insight into the interplay between bone morphogenetic protein 4 (BMP4) signaling and ECM mechanics in controlling the differentiation of glioblastoma (GBM) tumor initiating cells (TICs), we performed whole-genome RNA sequencing of GBM TICs on soft or stiff polyacrylamide hydrogels and in BMP4- or growth factor-supplemented medium.[50] Interestingly, whereas comparatively few transcripts were stiffness-sensitive in growth medium, many more transcripts were stiffness-sensitive in the presence of BMP4 (Figure 1.2A). The notion that BMP4 sensitizes GBM TICs to stiffness cues confirmed earlier work in which we showed that TICs are largely stiffness-insensitive under self-renewal conditions.[51] Surprisingly, pathway analysis revealed oxidative phosphorylation as one of the few intrinsically stiffness-sensitive systems (Figure 1.2B). We functionally confirmed this

finding by showing that oxygen consumption varies with stiffness under both self-renewal conditions and in the presence of BMP4 (Figure 1.2C). Transcriptomic analysis has also been applied to explore coupling effects between ECM parameters, in one example through RNA sequencing of stem cells on eight combinations of matrix stiffnesses, stress relaxation properties and adhesion ligand densities. In general, transcriptomic changes associated with one ECM property depended on the collective context provided by the other two properties.[52] Systems-level analyses can further reveal unexpected insights into therapeutic responses. For example, transcriptomic analysis of breast cancer cells on 2D/3D poly(ethylene glycol) (PEG) hydrogels and in uniform tumor spheroids enabled screens that uncovered synergies between MEK inhibition and the tyrosine kinase inhibitor sorafenib in reducing tumor burden in mouse xenograft models.[53]

Many non-coding RNAs regulate gene expression at the transcriptional and post-transcriptional level, and there is much interest in understanding how non-coding RNAs are regulated by ECM properties. In human MSCs, transcriptomic studies indicate that ECM stiffness upregulates miR-100-5p and miR-143-3p (Figure 1.2D). Subsequent functional studies implicated both miRNAs in promoting osteogenesis through mTOR pathway suppression (Figure 1.2E).[54] Such approaches have also proven valuable in studies of miRNA regulation of immunity and inflammation, including monocyte-to-macrophage differentiation, where a network of miRNAs was discovered to regulate macrophage behavior by influencing signaling through p53, integrins, and focal adhesions.[55] In still another study on stiffness-dependent differentiation of pluripotent stem cells, the long non-coding RNA (lncRNA) LINC00458 was found to increase on soft matrices, where it was necessary for endodermal lineage determination.[56] Finally, in vascular smooth muscle cells, matrix stiffening was found to enhance expression of the lncRNA MALAT1, which was then demonstrated to endothelial repair following vascular injury.[57]

An emerging extension of proteomic studies that is especially relevant to cell and tissue engineering is the examination of the matrisome, i.e. the complement of ECM and ECM-related proteins, including those secreted or deposited in the process of ECM remodeling.[58] Proteomic analysis of the matrisome in 3D hydrogels has helped elucidate regulatory functions of the pericellular matrix. One such study utilized stable isotope labeling with amino acids in cell culture (SILAC) to distinguish newly secreted proteins of human MSCs in hyaluronic acid and PEG diacrylate-based hydrogels.[59] ECM proteins composed >40% of all nascent proteins, with pericellular matrix deposition promoting adipogenesis on less cross-linked hydrogels. Label-free proteomic analysis has also been integrated with PEG hydrogel systems and has produced the observation that MSCs exhibit distinct collagen expression profiles under TGFβ1 or PDGF/EGF treatment. Here the analysis was facilitated by trypsin-degradable PEG hydrogels that allowed separate consideration of deposited ECM proteins and proteins from cell lysates.[60] Proteomic approaches are now being extended to study post-translational modifications on synthetic matrices.[61,62] For example, the nanoscale roughness of ZrO_x surfaces significantly alters the expression and phosphorylation profile of proteins that are involved in mechanotransduction and neuronal differentiation of neuro-like PC12 cells.[61] Surface nanostructures can also boost expression of anti-aging and anti-apoptotic proteins in human pancreatic β-cells, which are key to improving β-cell survival and differentiation.[62]

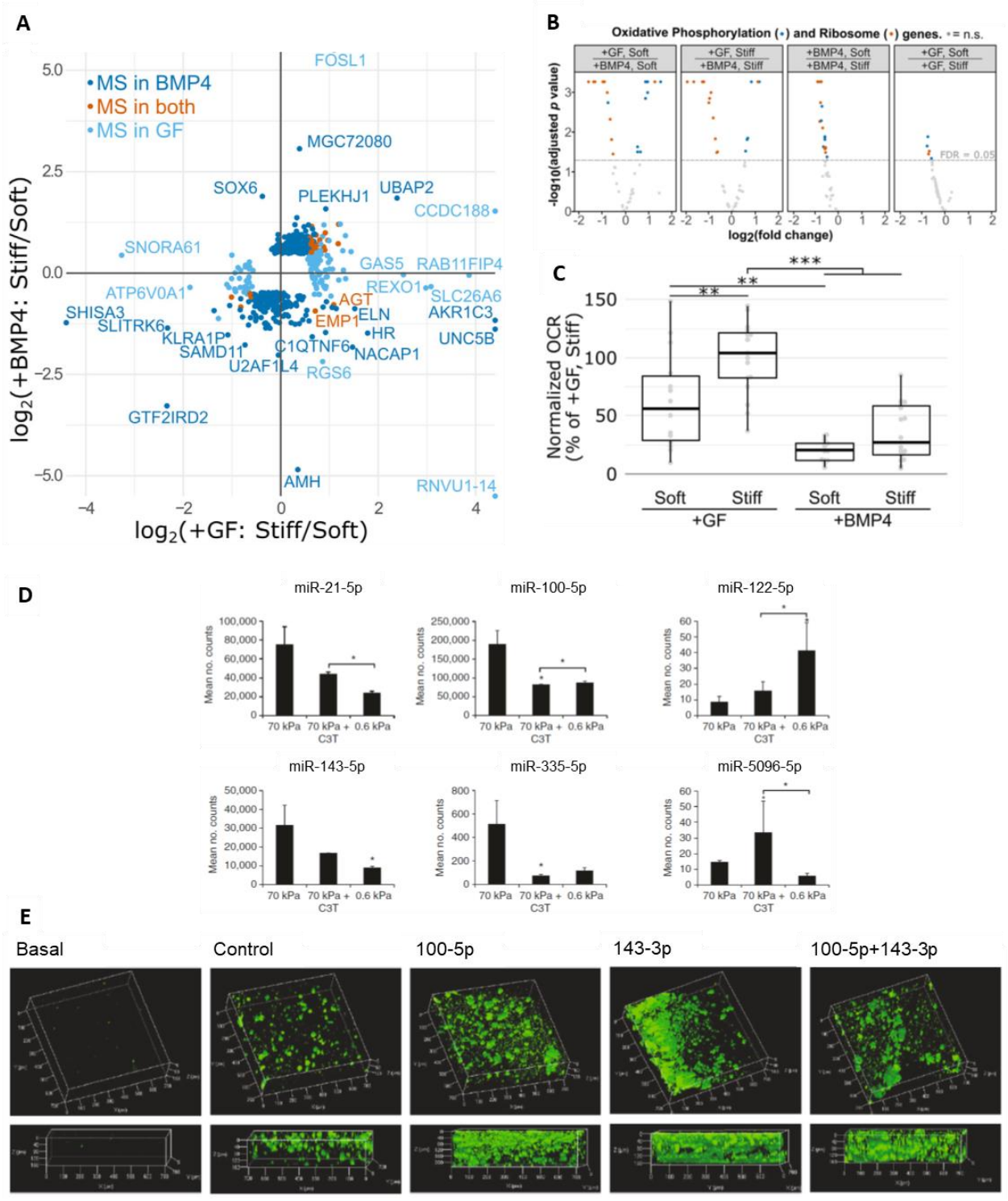

Figure 1.2. Application of RNA-seq analysis on synthetic hydrogels to identify mechanosensitive genes and miRNAs. (A) Changes in mechanosensitive (MS) genes for BMP4-treated cells versus growth factor-treated cells. (B) Ribosome protein expression is upregulated by both BMP4 treatment and matrix stiffening. BMP4 upregulates a few oxidative phosphorylation (OXPHOS) genes but its net effect is to downregulate OXPHOS genes, while stiffness universally upregulates OXPHOS genes. (C) Both stiff ECM and BMP4 treatment significantly increase basal oxygen

consumption rate (OCR). (D) Mean counts from miRNA sequencing of representative miRNAs whose expression is sensitive to ECM stiffness or RhoA inhibitor (C3T) (E) 3D projections of hydroxyapatite staining (green) showing a synergy in promoting MSC osteogenesis by miR-100-5p and miR-143-3p. (A–C) adapted with permission from Hughes et al.[50] (D–E) reproduced with permission from Frith et al.[54]

Perhaps the newest frontier in these systems-level studies involves the dissection of epigenomic responses to ECM cues. The mechanical microenvironment is increasingly recognized to induce epigenetic modifications through nuclear deformations that may follow alterations in cell cytoskeletal deformation.[63] In recent years, synthetic biomaterials have been introduced to study epigenomic responses to ECM biophysical signals, as matrix stiffness, topography, and applied mechanical forces have all been reported to alter the epigenome.[64,65] Culturing human MSCs on TiO_2 nanotubes with diameters of 70 nm promoted osteogenic differentiation, which is associated with enhanced methylation of histone H3 at lysine 4 (H3K4) in the promoter regions of osteogenic genes Runx2 and osteocalcin.[66] In a separate study using PEG-based hydrogels that can soften upon photodegradation, MSC histone acetylation was found to increase, and chromatin condensation was found to decrease, on stiff microenvironments.[67] Notably, these changes depended strongly on the duration of cell exposure to stiff ECM, implying that the acetylation events may serve as the basis for mechanical memory.

1.4. Conclusions and Future Outlook

Our understanding of cell-ECM interactions is rapidly evolving thanks to the emergence of biomaterial models that are increasingly compatible with systems-level analysis. High-throughput biomaterial platforms and integration of biomaterials with system-level "omics" measurements represent two key enabling tools. The continued advance of these approaches should greatly facilitate the development of technologies for cell and tissue engineering, disease modeling, and therapeutics.

One major challenge in the development of this new generation of ECM platforms is the need to balance experimental tractability against recapitulation of the complexities of tissue ECMs. Continued advances in polymer processing, 3D printing, and allied technologies should help make emerging ECM platforms more realistic, such as by incorporating fibrillar structures into hydrogels and introducing temporal control of matrix properties.[68,69] It will also be important to improve the compatibility of new ECM platforms with existing analytical assays and tools that were designed for standard culture plates and dishes, including plate readers and advanced optical and force microscopies.[34,35] As this review has indicated, interest in conducting system biology studies on synthetic biomaterials is high and rising, fueled in part by the rich and unexpected regulatory relationships these studies have already revealed. However, current efforts in this space are still often limited to manipulations of one property at a time (e.g. stiffness) and, even then, on discrete numbers of conditions. Moving forward, it will be valuable to combine both approaches described in this review, i.e. systems-level analysis on high-throughput biomaterial platforms. To reach this goal, real challenges must be overcome in terms of workflow design and management of the massive

data sets such efforts are likely to produce. It will also be important to ensure that the efficiency and sensitivity of the analytical techniques, including single cell RNA-seq and proteomics, are maintained when deployed in biomaterial platforms. Statistical tools such as combinatorial design of experiments and post hoc correlation analysis may also help narrow the combinatorial space of material conditions to consider.[49,70] If these challenges can be overcome, the field will be poised for a completely new era in which cell-ECM interactions can be connected in rich and surprising ways to broader aspects of cell physiology.

1.5. References

(1) Frantz, C., Stewart, K. M., and Weaver, V. M. (2010) The extracellular matrix at a glance. *J. Cell Sci. 123*, 4195–4200.

(2) Humphrey, J. D., Dufresne, E. R., and Schwartz, M. A. (2014) Mechanotransduction and extracellular matrix homeostasis. *Nat. Rev. Mol. Cell Biol. 15*, 802–812.

(3) Malik, R., Lelkes, P. I., and Cukierman, E. (2015) Biomechanical and biochemical remodeling of stromal extracellular matrix in cancer. *Trends Biotechnol. 33*, 230–236.

(4) Smith, L. R., Cho, S., and Discher, D. E. (2017) Stem Cell Differentiation is Regulated by Extracellular Matrix Mechanics. *Physiology 33*, 16–25.

(5) Vining, K. H., and Mooney, D. J. (2017) Mechanical forces direct stem cell behaviour in development and regeneration. *Nat. Rev. Mol. Cell Biol. 18*, 728–742.

(6) Wei, S. C., and Yang, J. (2016) Forcing through Tumor Metastasis: The Interplay between Tissue Rigidity and Epithelial–Mesenchymal Transition. *Trends Cell Biol. 26*, 111–120.

(7) Chen, J., and Kumar, S. (2017) Biophysical regulation of cancer stem/initiating cells: Implications for disease mechanisms and translation. *Curr. Opin. Biomed. Eng. 1*, 87–95.

(8) Upadhyaya, A. (2017) Mechanosensing in the immune response. *Semin. Cell Dev. Biol. 71*, 137–145.

(9) Kyburz, K. A., and Anseth, K. S. (2015) Synthetic Mimics of the Extracellular Matrix: How Simple is Complex Enough? *Ann. Biomed. Eng. 43*, 489–500.

(10) Li, Q., Uygun, B. E., Geerts, S., Ozer, S., Scalf, M., Gilpin, S. E., Ott, H. C., Yarmush, M. L., Smith, L. M., Welham, N. V., and Frey, B. L. (2016) Proteomic analysis of naturally-sourced biological scaffolds. *Biomaterials 75*, 37–46.

(11) Tibbitt, M. W., and Anseth, K. S. (2009) Hydrogels as extracellular matrix mimics for 3D cell culture. *Biotechnol. Bioeng. 103*, 655–663.

(12) Zahir, N., Yeung, T., Ming, W., Janmey, P. A., and Weaver, V. M. (2002) Peering from the outside in: viscoelastic properties of the extracellular matrix dictate spatial organization and apoptosis resistance in mammary epithelial cells, *Proceedings of the Second Joint 24th Annual Conference and the Annual Fall Meeting of the Biomedical Engineering Society [Engineering in Medicine and Biology]*, pp 430–431 vol.1.

(13) Ulrich, T. A., Pardo, E. M. de J., and Kumar, S. (2009) The Mechanical Rigidity of the Extracellular Matrix Regulates the Structure, Motility, and Proliferation of Glioma Cells. *Cancer Res. 69*, 4167–4174.

(14) Kalli, M., and Stylianopoulos, T. (2018) Defining the Role of Solid Stress and Matrix Stiffness in Cancer Cell Proliferation and Metastasis. *Front. Oncol. 8*, Article 55.

(15) Engler, A. J., Sen, S., Sweeney, H. L., and Discher, D. E. (2006) Matrix Elasticity Directs Stem Cell Lineage Specification. *Cell 126*, 677–689.

(16) Huebsch, N., Arany, P. R., Mao, A. S., Shvartsman, D., Ali, O. A., Bencherif, S. A., Rivera-Feliciano, J., and Mooney, D. J. (2010) Harnessing traction-mediated manipulation of the cell/matrix interface to control stem-cell fate. *Nat. Mater. 9*, 518–526.

(17) Lv, H., Li, L., Sun, M., Zhang, Y., Chen, L., Rong, Y., and Li, Y. (2015) Mechanism of regulation of stem cell differentiation by matrix stiffness. *Stem Cell Res. Ther. 6*, 103.

(18) Semler, E. J., Lancin, P. A., Dasgupta, A., and Moghe, P. V. (2005) Engineering hepatocellular morphogenesis and function via ligand-presenting hydrogels with graded mechanical compliance. *Biotechnol. Bioeng. 89*, 296–307.

(19) Pathak, A., and Kumar, S. (2012) Independent regulation of tumor cell migration by matrix stiffness and confinement. *Proc. Natl. Acad. Sci. 109*, 10334–10339.

(20) Chaudhuri, O., Gu, L., Darnell, M., Klumpers, D., Bencherif, S. A., Weaver, J. C., Huebsch, N., and Mooney, D. J. (2015) Substrate stress relaxation regulates cell spreading. *Nat. Commun. 6*, 1–7.

(21) Seidi, A., Ramalingam, M., Elloumi-Hannachi, I., Ostrovidov, S., and Khademhosseini, A. (2011) Gradient biomaterials for soft-to-hard interface tissue engineering. *Acta Biomater. 7*, 1441–1451.

(22) Oudin, M. J., and Weaver, V. M. (2016) Physical and Chemical Gradients in the Tumor Microenvironment Regulate Tumor Cell Invasion, Migration, and Metastasis. *Cold Spring Harb. Symp. Quant. Biol. 81*, 189–205.

(23) Jo, H., Yoon, M., Gajendiran, M., and Kim, K. (2020) Recent Strategies in Fabrication of Gradient Hydrogels for Tissue Engineering Applications. *Macromol. Biosci. 20*, 1900300.

(24) Xia, T., Liu, W., and Yang, L. (2017) A review of gradient stiffness hydrogels used in tissue engineering and regenerative medicine. *J. Biomed. Mater. Res. A 105*, 1799–1812.

(25) Hadden, W. J., Young, J. L., Holle, A. W., McFetridge, M. L., Kim, D. Y., Wijesinghe, P., Taylor-Weiner, H., Wen, J. H., Lee, A. R., Bieback, K., Vo, B.-N., Sampson, D. D., Kennedy, B. F., Spatz, J. P., Engler, A. J., and Choi, Y. S. (2017) Stem cell migration and mechanotransduction on linear stiffness gradient hydrogels. *Proc. Natl. Acad. Sci. 114*, 5647–5652.

(26) Zhang, H., Lin, F., Huang, J., and Xiong, C. (2020) Anisotropic stiffness gradient-regulated mechanical guidance drives directional migration of cancer cells. *Acta Biomater. 106*, 181–192.

(27) Davidson, C. D., Jayco, D. K. P., Matera, D. L., DePalma, S. J., Hiraki, H. L., Wang, W. Y., and Baker, B. M. (2020) Myofibroblast activation in synthetic fibrous matrices composed of dextran vinyl sulfone. *Acta Biomater. 105*, 78–86.

(28) Ulrich, T. A., Jain, A., Tanner, K., MacKay, J. L., and Kumar, S. (2010) Probing cellular mechanobiology in three-dimensional culture with collagen–agarose matrices. *Biomaterials 31*, 1875–1884.

(29) Ulrich, T. A., Lee, T. G., Shon, H. K., Moon, D. W., and Kumar, S. (2011) Microscale mechanisms of agarose-induced disruption of collagen remodeling. *Biomaterials 32*, 5633–5642.

(30) McNamara, L. E., Burchmore, R., Riehle, M. O., Herzyk, P., Biggs, M. J. P., Wilkinson, C. D. W., Curtis, A. S. G., and Dalby, M. J. (2012) The role of microtopography in cellular mechanotransduction. *Biomaterials 33*, 2835–2847.

(31) Zhang, K., Xiao, X., Wang, X., Fan, Y., and Li, X. (2019) Topographical patterning: characteristics of current processing techniques, controllable effects on material properties and co-cultured cell fate, updated applications in tissue engineering, and improvement strategies. *J. Mater. Chem. B 7*, 7090–7109.

(32) Liu, X., Liu, R., Cao, B., Ye, K., Li, S., Gu, Y., Pan, Z., and Ding, J. (2016) Subcellular cell geometry on micropillars regulates stem cell differentiation. *Biomaterials 111*, 27–39.

(33) Hou, Y., Xie, W., Yu, L., Camacho, L. C., Nie, C., Zhang, M., Haag, R., and Wei, Q. (2020) Surface Roughness Gradients Reveal Topography-Specific Mechanosensitive Responses in Human Mesenchymal Stem Cells. *Small 16*, 1905422.

(34) Hu, J., Gondarenko, A. A., Dang, A. P., Bashour, K. T., O'Connor, R. S., Lee, S., Liapis, A., Ghassemi, S., Milone, M. C., Sheetz, M. P., Dustin, M. L., Kam, L. C., and Hone, J. C. (2016) High-Throughput Mechanobiology Screening Platform Using Micro- and Nanotopography. *Nano Lett. 16*, 2198–2204.

(35) Rianna, C., Radmacher, M., and Kumar, S. (2020) Direct Evidence that Tumor Cells Soften when Navigating Confined Spaces. *Mol. Biol. Cell* mbc.E19-10-0588.

(36) Rossano, L., Cimmino, C., Cavalli, S., Ventre, M., and Netti, P. A. (2018) Regulating Fibroblast Shape and Mechanics through Photoresponsive Surfaces with Concentric Circular Topographic Patterns. *Adv. Mater. Interfaces 5*, 1800890.

(37) Engler, A., Bacakova, L., Newman, C., Hategan, A., Griffin, M., and Discher, D. (2004) Substrate Compliance versus Ligand Density in Cell on Gel Responses. *Biophys. J. 86*, 617–628.

(38) Harjanto, D., and Zaman, M. H. (2009) Matrix mechanics and receptor–ligand interactions in cell adhesion. *Org. Biomol. Chem. 8*, 299–304.

(39) E. Brown, T., and S. Anseth, K. (2017) Spatiotemporal hydrogel biomaterials for regenerative medicine. *Chem. Soc. Rev. 46*, 6532–6552.

(40) Rape, A. D., Zibinsky, M., Murthy, N., and Kumar, S. (2015) A synthetic hydrogel for the high-throughput study of cell–ECM interactions. *Nat. Commun. 6*, 8129.

(41) Tong, X., Jiang, J., Zhu, D., and Yang, F. (2016) Hydrogels with Dual Gradients of Mechanical and Biochemical Cues for Deciphering Cell-Niche Interactions. *ACS Biomater. Sci. Eng. 2*, 845–852.

(42) Vega, S. L., Kwon, M. Y., Song, K. H., Wang, C., Mauck, R. L., Han, L., and Burdick, J. A. (2018) Combinatorial hydrogels with biochemical gradients for screening 3D cellular microenvironments. *Nat. Commun. 9*, 614.

(43) Zhou, Q., Ge, L., Guimarães, C. F., Kühn, P. T., Yang, L., and Rijn, P. van. (2018) Development of a Novel Orthogonal Double Gradient for High-Throughput Screening of Mesenchymal Stem Cells–Materials Interaction. *Adv. Mater. Interfaces 5*, 1800504.

(44) Seo, J., Shin, J.-Y., Leijten, J., Jeon, O., Bal Öztürk, A., Rouwkema, J., Li, Y., Shin, S. R., Hajiali, H., Alsberg, E., and Khademhosseini, A. (2018) Interconnectable Dynamic Compression Bioreactors for Combinatorial Screening of Cell Mechanobiology in Three Dimensions. *ACS Appl. Mater. Interfaces 10*, 13293–13303.

(45) Lopes, D., Fernandes, C., Nóbrega, J. M., Patrício, S. G., Oliveira, M. B., and Mano, J. F. (2019) Screening of perfused combinatorial 3D microenvironments for cell culture. *Acta Biomater. 96*, 222–236.

(46) Gallagher, W. M., Lynch, I., Allen, L. T., Miller, I., Penney, S. C., O'Connor, D. P., Pennington, S., Keenan, A. K., and Dawson, K. A. (2006) Molecular basis of cell–biomaterial interaction: Insights gained from transcriptomic and proteomic studies. *Biomaterials 27*, 5871–5882.

(47) Cranford, S. W., Boer, J. de, Blitterswijk, C. van, and Buehler, M. J. (2013) Materiomics: An -omics Approach to Biomaterials Research. *Adv. Mater. 25*, 802–824.

(48) Groen, N., Guvendiren, M., Rabitz, H., Welsh, W. J., Kohn, J., and de Boer, J. (2016) Stepping into the omics era: Opportunities and challenges for biomaterials science and engineering. *Acta Biomater. 34*, 133–142.

(49) Darnell, M., and Mooney, D. J. (2017) Leveraging advances in biology to design biomaterials. *Nat. Mater. 16*, 1178–1185.

(50) Hughes, J. H., Ewy, J. M., Chen, J., Wong, S. Y., Tharp, K. M., Stahl, A., and Kumar, S. (2019) Transcriptomic analysis reveals that BMP4 sensitizes glioblastoma tumor-initiating cells to mechanical cues. *Matrix Biol. 85–86*, 112–127.

(51) Wong, S. Y., Ulrich, T. A., Deleyrolle, L. P., MacKay, J. L., Lin, J.-M. G., Martuscello, R. T., Jundi, M. A., Reynolds, B. A., and Kumar, S. (2015) Constitutive Activation of Myosin-Dependent Contractility Sensitizes Glioma Tumor-Initiating Cells to Mechanical Inputs and Reduces Tissue Invasion. *Cancer Res. 75*, 1113–1122.

(52) Darnell, M., O'Neil, A., Mao, A., Gu, L., Rubin, L. L., and Mooney, D. J. (2018) Material microenvironmental properties couple to induce distinct transcriptional programs in mammalian stem cells. *Proc. Natl. Acad. Sci.* 201802568.

(53) Schwartz, A. D., Barney, L. E., Jansen, L. E., Nguyen, T. V., Hall, C. L., Meyer, A. S., and Peyton, S. R. (2017) A biomaterial screening approach reveals microenvironmental mechanisms of drug resistance. *Integr. Biol. 9*, 912–924.

(54) Frith, J. E., Kusuma, G. D., Carthew, J., Li, F., Cloonan, N., Gomez, G. A., and Cooper-White, J. J. (2018) Mechanically-sensitive miRNAs bias human mesenchymal stem cell fate via mTOR signalling. *Nat. Commun. 9*, 257.

(55) Li, J., Wang, S., Li, Y., Zhang, N., Gribskov, M., Zhang, X., Lin, M., Shao, D., Zhang, C., Dai, L., Qin, C., Duan, X., Li, J., Xu, F., and Yang, H. (2020) miRNA-mediated macrophage behaviors responding to matrix stiffness and ox-LDL. *J. Cell. Physiol. n/a*.

(56) Chen, Y.-F., Li, Y.-S. J., Chou, C.-H., Chiew, M. Y., Huang, H.-D., Ho, J. H.-C., Chien, S., and Lee, O. K. (2020) Control of matrix stiffness promotes endodermal lineage specification by regulating SMAD2/3 via lncRNA LINC00458. *Sci. Adv. 6*, eaay0264.

(57) Yu Christopher K., Xu Tina, Assoian Richard K., and Rader Daniel J. (2018) Mining the Stiffness-Sensitive Transcriptome in Human Vascular Smooth Muscle Cells Identifies Long Noncoding RNA Stiffness Regulators. *Arterioscler. Thromb. Vasc. Biol. 38*, 164–173.

(58) Hynes, R. O., and Naba, A. (2012) Overview of the Matrisome—An Inventory of Extracellular Matrix Constituents and Functions. *Cold Spring Harb. Perspect. Biol. 4*, a004903.

(59) Ferreira, S. A., Motwani, M. S., Faull, P. A., Seymour, A. J., Yu, T. T. L., Enayati, M., Taheem, D. K., Salzlechner, C., Haghighi, T., Kania, E. M., Oommen, O. P., Ahmed, T., Loaiza, S., Parzych, K., Dazzi, F., Varghese, O. P., Festy, F., Grigoriadis, A. E., Auner, H. W., Snijders, A. P., Bozec, L., and Gentleman, E. (2018) Bi-directional cell-pericellular matrix interactions direct stem cell fate. *Nat. Commun. 9*, 1–12.

(60) Devaud, Y. R., Avilla-Royo, E., Trachsel, C., Grossmann, J., Martin, I., Lutolf, M. P., and Ehrbar, M. (2018) Label-Free Quantification Proteomics for the Identification of Mesenchymal Stromal Cell Matrisome Inside 3D Poly(Ethylene Glycol) Hydrogels. *Adv. Healthc. Mater. 7*, 1800534.

(61) Maffioli, E., Schulte, C., Nonnis, S., Grassi Scalvini, F., Piazzoni, C., Lenardi, C., Negri, A., Milani, P., and Tedeschi, G. (2018) Proteomic Dissection of Nanotopography-Sensitive Mechanotransductive Signaling Hubs that Foster Neuronal Differentiation in PC12 Cells. *Front. Cell. Neurosci. 11*, Article 417.

(62) Galli, A., Maffioli, E., Sogne, E., Moretti, S., Di Cairano, E. S., Negri, A., Nonnis, S., Norata, G. D., Bonacina, F., Borghi, F., Podestà, A., Bertuzzi, F., Milani, P., Lenardi, C., Tedeschi, G., and Perego, C. (2018) Cluster-assembled zirconia substrates promote long-term differentiation and functioning of human islets of Langerhans. *Sci. Rep. 8*, 1–17.

(63) Kelkhoff, D., Downing, T., and Li, S. (2016) Mechanotransduction to Epigenetic Remodeling, in *Molecular and Cellular Mechanobiology* (Chien, S., Engler, A. J., and Wang, P. Y., Eds.), pp 163–173. Springer, New York, NY.

(64) Lv, L., Tang, Y., Zhang, P., Liu, Y., Bai, X., and Zhou, Y. (2017) Biomaterial Cues Regulate Epigenetic State and Cell Functions—A Systematic Review. *Tissue Eng. Part B Rev. 24*, 112–132.

(65) Crowder, S. W., Leonardo, V., Whittaker, T., Papathanasiou, P., and Stevens, M. M. (2016) Material Cues as Potent Regulators of Epigenetics and Stem Cell Function. *Cell Stem Cell 18*, 39–52.

(66) Lv, L., Liu, Y., Zhang, P., Zhang, X., Liu, J., Chen, T., Su, P., Li, H., and Zhou, Y. (2015) The nanoscale geometry of TiO2 nanotubes influences the osteogenic differentiation of human adipose-derived stem cells by modulating H3K4 trimethylation. *Biomaterials 39*, 193–205.

(67) Killaars, A. R., Grim, J. C., Walker, C. J., Hushka, E. A., Brown, T. E., and Anseth, K. S. (2019) Extended Exposure to Stiff Microenvironments Leads to Persistent Chromatin Remodeling in Human Mesenchymal Stem Cells. *Adv. Sci. 6*, 1801483.

(68) Prince, E., and Eugenia, K. (2019) Design and applications of man-made biomimetic fibrillar hydrogels. *Nat. Rev. Mater. Lond. 4*, 99–115.

(69) Rosales, A. M., Vega, S. L., DelRio, F. W., Burdick, J. A., and Anseth, K. S. (2017) Hydrogels with Reversible Mechanics to Probe Dynamic Cell Microenvironments. *Angew. Chem. Int. Ed. 56*, 12132–12136.

(70) Decaris, M. L., and Leach, J. K. (2011) Design of Experiments Approach to Engineer Cell-Secreted Matrices for Directing Osteogenic Differentiation. *Ann. Biomed. Eng. 39*, 1174–1185.

Chapter 2

A Combinatorial Hyaluronic Acid (HA)-Based Hydrogel Array Platform For Investigating Cell Mechanobiology

Abstract

Biophysical cues in the extracellular matrix (ECM) regulate stem cell behavior in a complex, non-linear, and interdependent manner. To quantify these important regulatory relationships and gain a comprehensive understanding of mechanotransduction, there is a need for high-throughput matrix platforms that enable parallel culture and analysis of cells in various matrix conditions. Here we describe a multi-well hyaluronic acid (HA) platform in which cells are cultured on combinatorial arrays of hydrogels spanning a range of elasticities and adhesivities. Our approach is based on an orthogonal photopatterning strategy previously developed in our laboratory, with the stiffness gradient implemented by a programmable light illumination system. Our system allows individual treatment and analysis of each matrix environment while eliminating contributions of haptotaxis and durotaxis. In human mesenchymal stem cells (hMSCs), this platform recapitulated expected relationships between matrix stiffness, adhesivity and cell mechanosensing. The platform also supported adipogenesis and osteogenesis of hMSCs, as well as the beige adipocyte development of Shingo adipose tissue (sWAT) preadipocytes. We anticipate that this platform has broad applications in dissecting molecular mechanisms of stem cell mechanosensing.

The studies described in this chapter were conducted in collaboration with Kelly C.Y. Wong, Nicole A. Repina, Kayla J. Wolf, Garrett E. Dempsey and Andreas Stahl, and will be a part of a peer-reviewed publication.

2.1. Introduction

Stem cells play a central role in tissue engineering because of their ability to self-renew and to differentiate into specialized lineages. Stem cells are deeply engaged with the surrounding extracellular matrix (ECM), whose properties guide fundamental cellular behaviors including cell morphology, migration, proliferation and fate commitment.[1–5] One major goal in tissue engineering is to create a favorable niche environment to maintain the renewal potential of stem cells and precisely control their lineage commitment, which requires a systematic understanding of the relationships between ECM biophysical properties and stem cell mechanosensing. To this end, biomaterial scaffolds have been developed to mimic native ECM properties and to serve as tunable platforms to study stem cell-ECM interactions.[6–8] Synthetic hydrogels are a common type of biomaterial scaffolds in tissue engineering because of their structural and physical similarities with native ECM and their versatility with which they can be chemically functionalized.[9–12] Synthetic hydrogel platforms have been developed to investigate cell response to various biophysical cues such as matrix mechanics,[13–15] integrin-adhesive ligands[16–18] and surface topography.[19,20]

ECM regulates stem cell behaviors in a complex, non-linear, and interdependent manner. For example, matrix stiffness has strong coupling effects with adhesive ligand density, stress relaxation properties and surface wettability.[16,21,22] Mesenchymal stem cell (MSC) phenotypes and transcriptomic profiles were reported to be non-linearly regulated by topography and stiffness.[23–25] The complexity of cell-ECM interactions underscores the need to develop high-throughput hydrogel platforms that allow for parallel culture of cells in many matrix conditions at one time. High-throughput hydrogel platforms have two major categories: discrete hydrogel arrays[26–28] and continuous gradient hydrogels.[29–31] While both platforms provide various matrix conditions for parallel culture, these conditions are physically separated on an array, while on a gradient gel cells residing on different conditions can interact with each other and even migrate across conditions.[32] Gradient gels provides infinite resolution of test parameters within the dynamic range, while the resolution of arrays are limited by the number of gels, making gradient gels generally more favorable for screening optimal matrix conditions. On the other hand, array platforms are more suitable than gradient gels when individual assessment of a certain matrix condition is needed. First, arrays effectively prevent crosstalk across matrix conditions, such that the response of one subpopulation does not interfere with those on a different condition. Second, sample isolation for downstream analysis is far more straightforward on the arrays, while gradient gels would need to be carefully dissected and separated prior to sample extraction.

To date, hydrogel array platforms fabricated by automated liquid-handling systems can culture and analyze cells on hundreds or even thousands of ECM conditions in parallel.[33,34] However, the scale of throughput is not the only parameter to consider for an array platform. Compatibility with downstream bioassays becomes a critical issue when extensive analysis of individual matrix condition is needed. Most laboratory equipment and assays have been optimized for standard multi-well culture plates. Therefore, making hydrogel arrays in multi-well plates may largely facilitate sample processing and analysis by standard bioassays. Array platforms in a multi-well setting have been successfully developed, but the fabrication usually requires robotic injection equipment or in-house fabrication of culture chambers.[34–36] Hydrogel arrays made directly in standard well plates include examples reported by Mih

et al., Díaz-Bello et al., and Hribar et al.[37–39] However, most studies were focused on gradients of single ECM property, which leaves a gap for multi-well combinatorial arrays.

In this chapter, we describe a combinatorial, multi-well hydrogel array platform in which cells are cultured on hyaluronic acid (HA) gels with combinations of stiffness and adhesive RGD peptide density. Our approach is based on an orthogonal photopatterning strategy previously developed in our laboratory,[40] with the stiffness gradient patterned by a programmable light illumination system developed by Repina et al.[41] Each well contains one HA hydrogel that represents one unique combination of stiffness and RGD ligand density. We demonstrated the array in a 96-well plate format, but the fabrication technique can be easily adapted to other well plate types. This platform allows individual treatment and analysis of each matrix environment while eliminating contributions of haptotaxis and durotaxis. We conducted a proof-of-principle study on human adipose-derived mesenchymal stem cells (hMSCs) to validate this platform by recapitulating the relationships between matrix stiffness, adhesivity and cell morphology. We also evaluated the adipogenesis and osteogenesis of hMSCs as well as browning of Shingo adipose tissue preadipocytes (sWATs) on the array platform.

2.2. Results and Discussion

2.2.1. HA Hydrogel Array Design and Fabrication

Hyaluronic acid (HA) is a linear polysaccharide prevalently expressed in native ECM. HA has been widely used as the backbone of ECM-mimetic hydrogels in tissue engineering, due to its biocompatibility and flexibility to chemical modifications.[42,43] Methacrylation is a common modification that occurs on the primary hydroxyl groups of HA, which generates α, β-unsaturated carbonyls that can undergo Michael addition-type reactions or be photocrosslinked by radical polymerization. Methacrylated HA hydrogels with tunable mechanical properties have been used by our lab and others to study cell-matrix interplays that are dependent on stiffness, adhesive ligand density, topography or other biophysical cues.[44–47] In this study, we used 60 kDa HA as the hydrogel array backbone. We modified HA with excess methacrylic anhydride and achieved a high methacrylate to HA unit ratio of 70~80% estimated by ^{1}H-NMR (Figure 2.1). This is expected to provide sufficient reaction sites for peptide conjugation and photocrosslinking.

We designed the array in a 96-well plate format to maximize the number of possible conditions on a single plate. To fabricate 2D hydrogel arrays at the bottom of a well plate, one approach is to crosslink the hydrogel precursors directly in the wells.[37–39] Either coverslips or a lid with multiple posts may be applied to the top of gels and form a sandwich assembly to flatten the gels during crosslinking. One caveat of this approach is that the size or shape of the resulting hydrogels may not be easily customized unless another mold is added to the well. Alternatively, Zustiak et al. crosslinked the hydrogels outside the well plates and then transferred and sealed them to the well bottom,[48,49] which allowed them to change the size of the gels. However, for a 96-well plate, it could be very time- and labor-intensive to glue individual gels. A third approach is to fabricate the array on a flat substrate, and then glue the substrate to a bottomless well plate, which is similar to a topography screening device reported by Hu et al.[50] However, this approach was reported to require

around an hour to assemble the substrate and the well plate with oxygen plasma and aminosilane-mediated treatment. We developed a simple solution by utilizing double-sided medical tapes as part of the hydrogel mold and also an adhesive that attaches hydrogel array to the bottomless well plate. To ensure precise alignment of the hydrogel array and the well plate, we used a laser cutter to perforate the double-sided tapes and create "wells". HA hydrogel precursor was pipetted to these "wells", and a lid of PDMS posts was applied to flatten the gel surfaces. Each post have the appropriate spacing to match the holes on the tape (Figure 2.2A). The resulting hydrogels are ~200 μm thick (the same thickness as the double-sided tapes), and 3 mm wide. After removing the PDMS lid, the double-sided tape was further used to glue the array to a bottomless 96 well plate. Although we only focus on 96-well arrays in this Chapter, the fabrication strategy can be easily adapted to any other standardized or customized cell culture devices.

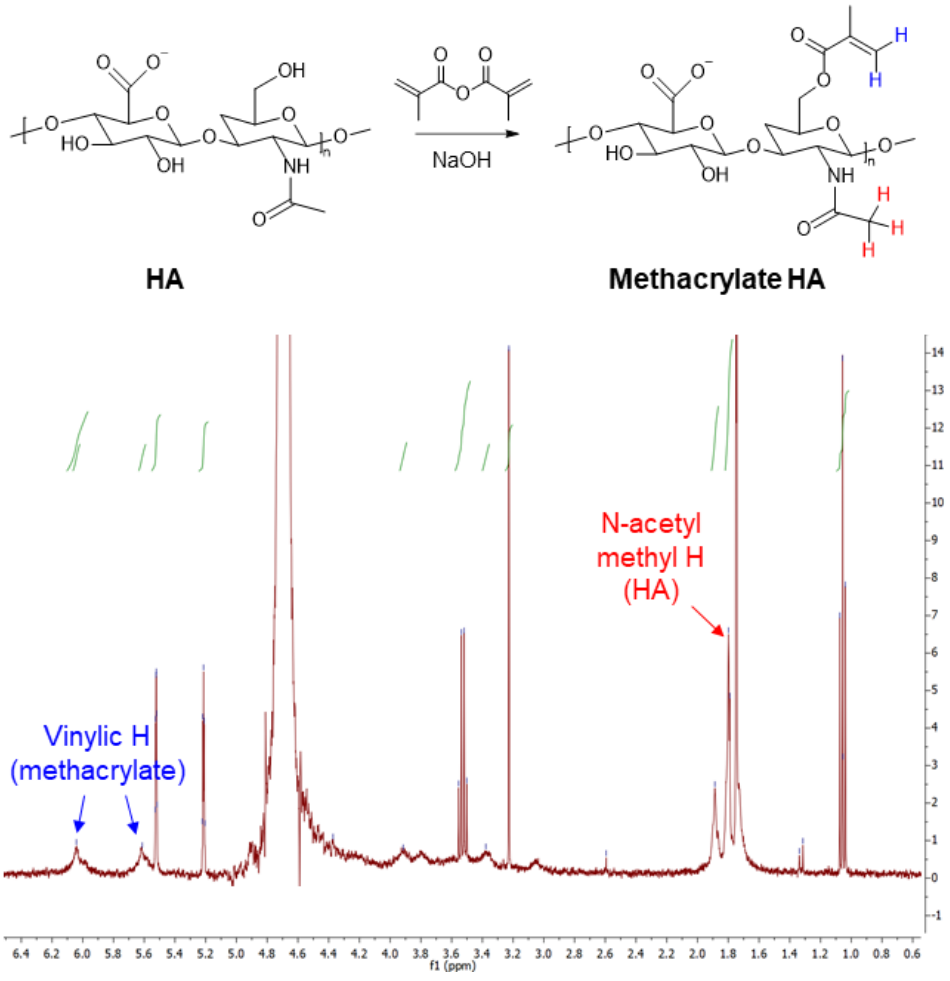

Figure 2.1. The reaction scheme of HA methacrylation (top) and ^{1}H-NMR spectrum of methacrylated HA (bottom). Arrows indicate the peaks for vinylic proton (blue) from the methacrylate groups and N-acetyl methyl protons (red) from the HA backbone.

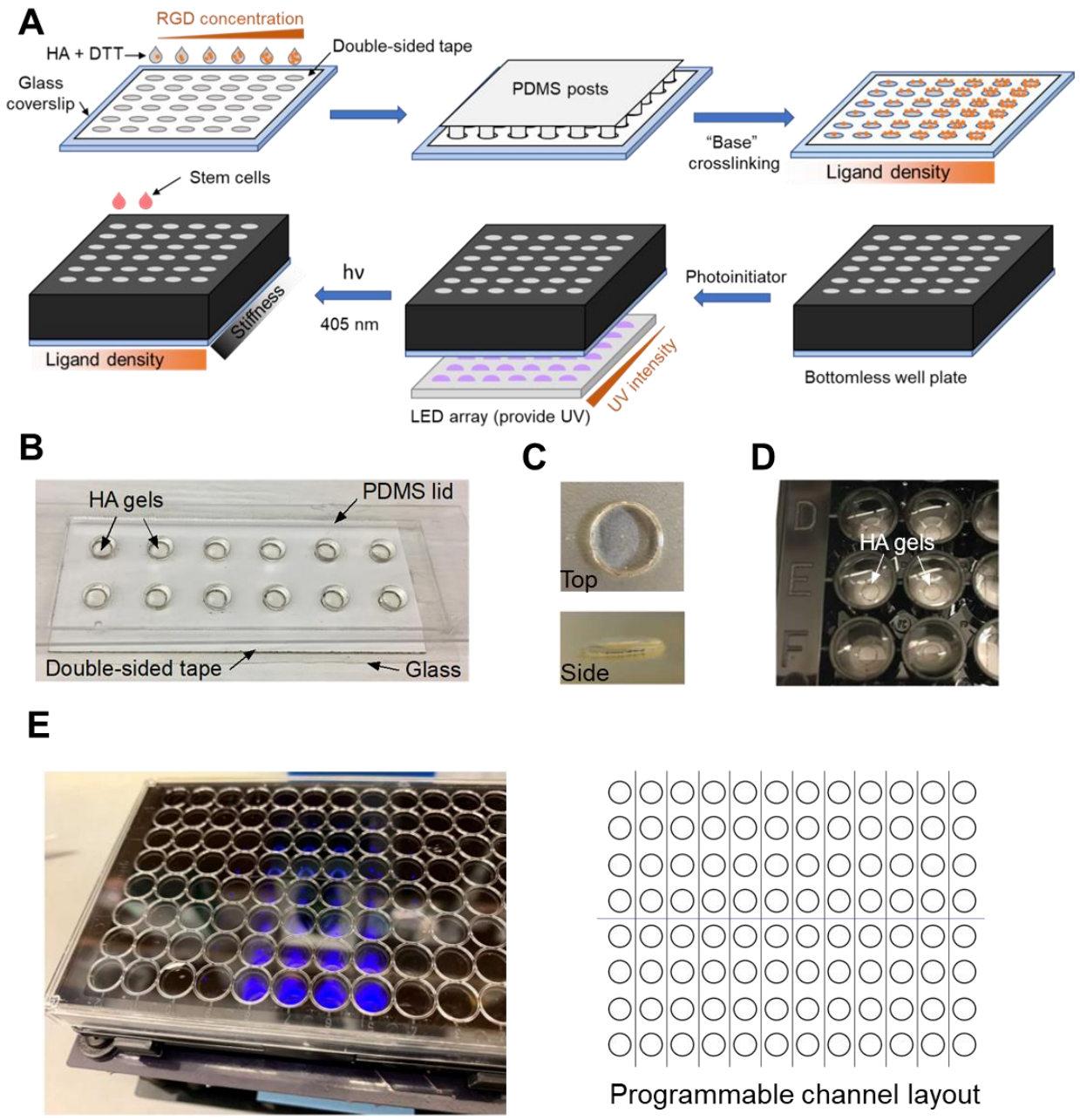

Figure 2.2. Fabrication of the HA hydrogel array platform. (A) Workflow of the array fabrication. RGD density is controlled by mixing methacrylated HA precursor with varying peptide concentrations. Stiffness is determined by the accumulation of two crosslinking steps: first by DTT, and then by radical photocrosslinking. (B) The array in its "sandwich" assembly. (C) Top view (upper) and side view (lower) of one gel in the array. Each gel is ~3 mm wide and ~200 μm thick. (D) Array assembled with a bottomless 96-well plate. (E) The hydrogel array was photopatterned by a light activation at variable amplitudes (LAVA) device. The LAVA device has 12×2 channels whose intensity and illumination time can be controlled independently.

The array platform integrates various elasticities along the X direction and adhesivities along the Y direction. Prior to crosslinking, we conjugated various concentrations of RGD peptide (Ac-GCGYGRGDSPG-NH2) to methacrylated HA precursors through the thiol-ene reaction, thus generating a series of RGD-modified HA (refer to as HA-RGD) to eventually give rise to an RGD density gradient on the hydrogel surface. The HA-RGD then underwent a two-step crosslinking reaction to generate the stiffness gradient. In the first step, HA-RGD was mixed with DTT at a thiol to HA unit ratio (T/H ratio) of 0.15 to create a soft "base" gel. The second crosslinking step involves a tunable illumination process that was achieved on a light activation at variable amplitudes (LAVA) device developed by Repina et al.[41] On the LAVA device, hydrogels in each well was radiated by a programmable 405 nm LED bulb in the presence of LAP photoinitiator, with both the intensity and time of illumination being adjustable (Figure 2.2E). In our study, we maintained a constant UV intensity (15 μW/mm^2) and adjusted the illumination time to fine-tune the crosslinking level.

2.2.2. Array Mechanical Property Characterization

To characterize the stiffness gradient, we used atomic force microscopy to indent the gel in at least five positions and extracted Young's moduli by fitting the resulting force extension curves to a Hertz model as described previously.[51] The hydrogel stiffness is highly correlated with the illumination time, spanning a dynamic range of 12 to 91 kPa with 0 to 90 seconds of illumination (Figure 2.3). An extended illumination time can increase the modulus to above 200 kPa. Unless specified otherwise, the following studies were focused on the 12-91 kPa range because the modulus of most human tissues falls between 500 Pa to 100 kPa.[52,53] Also, as illumination time increased, we observed a broader distribution of modulus across the gel, indicating increasing heterogeneity in crosslinking.

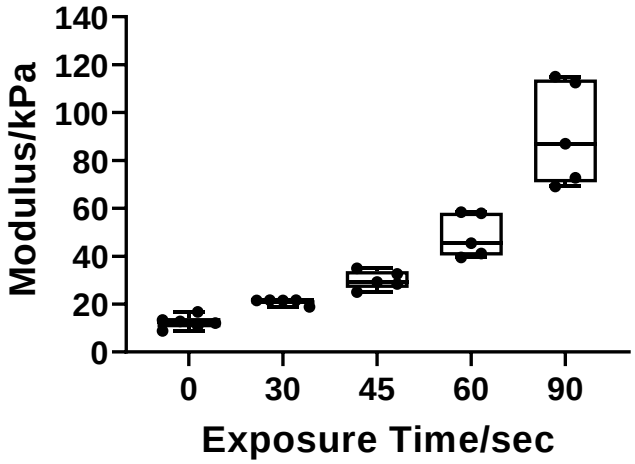

Figure 2.3. Stiffness gradient on the HA hydrogel array after LAP-induced photocrosslinking. Intensity of 405 nm UV radiation was fixed at 15 μW/mm^2. Gels were indented with a pyramid-tipped AFM probe and elastic moduli were calculated from at least 5 different locations on each individual gel, whose average was used as the elastic modulus of the gel. For each condition, at least 5 individual gels were measured. The median values of each condition are: 0 sec – 12 kPa, 30 sec – 21 kPa, 45 sec – 30 kPa, 60 sec – 48 kPa, 90 sec – 91 kPa.

As stated in 2.2.1, the lower end of hydrogel stiffness range depends on the T/H ratio. When the ratio fell below 0.15, we noticed that the hydrogels tended to swell in PBS buffer or cell culture media, leading to a convex gel surface that may complicate imaging analysis. Therefore, we did not set T/H ratio below 0.15. The modulus difference between HA-RGD gels and HA-only gels under the same illumination condition is negligible (data not shown), suggesting that the HA backbone still has sufficient unreacted methacrylate groups for the photocrosslinking after RGD conjugation.

2.2.3. Human Mesenchymal Stem Cell (hMSC) Response to Array Stiffness and Ligand Density

To demonstrate that our hydrogel array platform can recapitulate the effects of ECM stiffness and adhesive ligand density on cell mechanotransduction and morphological response, we cultured adipose-derived hMSCs on the platform, after which yes-associated protein (YAP) localization and cell spreading were evaluated. YAP is a key transcriptional regulator that responds directly to mechanical input and triggers a series of downstream cell response.[54,55] YAP is enriched in the nucleus of hMSCs on stiff matrices but predominantly localizes to the cytoplasm on soft matrices, thus YAP localization can be used as a readout of hMSC mechanosensing on the array platform. YAP nuclear localization was also reported on high ligand density, which promotes focal adhesion formation and increased cytoskeleton tension.[56] hMSC morphologies are also highly sensitive to matrix stiffness and adhesive ligand density on *in vitro* platforms.[17,57,58] We hypothesized that on our platform, increased stiffness and ligand density would enhance YAP nucleus localization and expand cell area.

To evaluate hMSC sensitivity to stiffness and RGD density gradients, we made a 3×5 array with 3 different RGD densities (0.1 mM, 0.25 mM and 0.5 mM in the HA-RGD precursors) and 5 different elasticities. hMSCs were seeded onto the array platform at a density of 5,000-7,500 cells/cm^2 and allowed to attach for 16 – 20 hrs. The time window was chosen to ensure cell attachment and also minimize any interference from cell division. After cell fixation, YAP localization was characterized by immunostaining. Cell shape and area were evaluated by phalloidin staining of F-actin cytoskeleton. To rule out possible contributions of cell-cell interactions and focus exclusively on the impact of cell-ECM interactions, we excluded clustered cells from the analysis. YAP localization was significantly affected by hydrogel stiffness and RGD density (Figure 2.4). Stiff gels and high RGD gels biased YAP localization to the nuclear region, shown as an overlap of YAP and DAPI staining (Figure 2.4A). We quantified YAP nuclear/cytoplasmic ratio for each individual cell by calculating the ratio of the average YAP intensity in the nucleus region and the average intensity in the cytoplasmic region of similar size that is adjacent to the nucleus. Some cells, especially those on low RGD and soft gels, were barely spread with minimum cytoplasmic region, and therefore excluded from the analysis. As stiffness increased, under both low RGD and medium RGD densities, YAP nuc/cyt ratio increased significantly from 12 to 91 kPa (Figure 2.4B). Under high RGD density, while statistical differences between low and high stiffness still persisted, the gaps in their median values were narrowed. When stiffness was below 48 kPa, YAP was more enriched in the nucleus as RGD density increased (Figure 2.4C). On 91 kPa gels, however, YAP localization was not sensitive to the ligand density changes. Our finding adds to recent work by Stanton et al., which reported that YAP localization was insensitive to stiffness at very high or low fibronectin density.[56] They attributed ligand

density-induced YAP translocation to cytoskeletal tension and αVβ3-integrin adhesion, which share similarities with mechanisms for stiffness-induced YAP translocation.

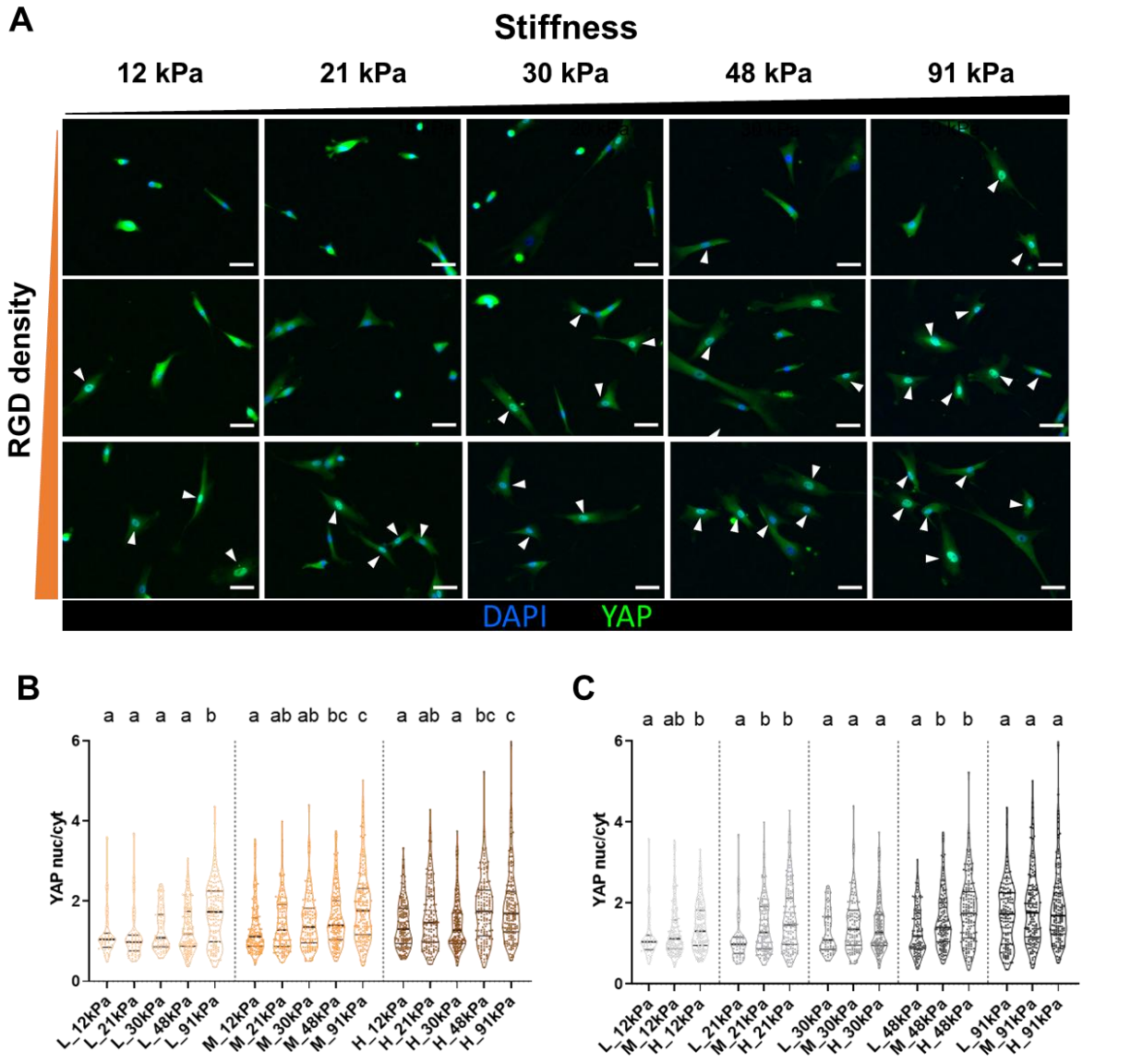

Figure 2.4. YAP localized to hMSC nucleus as matrix stiffness and RGD density increased. (A) High stiffness/high RGD density promotes YAP/TAZ nuclear localization. The nucleus is visualized with DAPI (blue). Arrows highlight cells with YAP nuc/cyt > 1.0. Scale bars: 50 μm. (B) Violin plot of YAP nuc/cyt ratios of individual cells on the array, grouped by RGD density. Data was pooled from experimental triplicates, as no systematic difference was observed among the triplicates. (C) Violin plot of the same dataset as Fig. 2.4B, grouped by stiffness. At least 40 cells were analyzed per gel, except on some low RGD or low stiffness gels where the overall number of hMSCs attached to the gel was under 40. a, b, c statistical families show $p<0.05$ from Kruskal-Wallis test for multiple comparison of non-normally distributed data. L, M, H: low, medium, and high RGD gels, respectively.

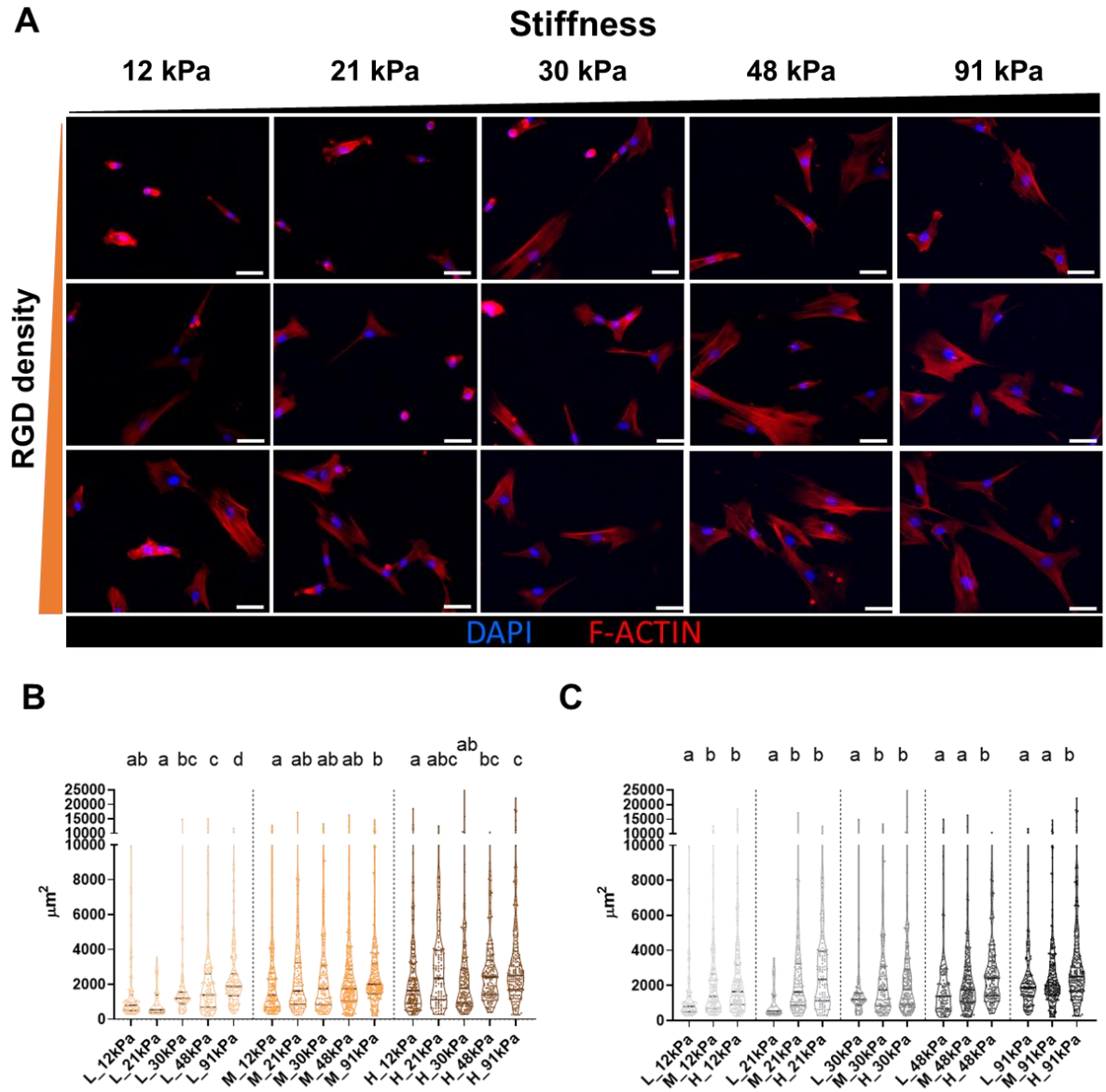

Figure 2.5. hMSC spreading area increased as matrix stiffness and RGD density increased. (A) High stiffness/high RGD density promotes hMSC spreading. The F-actin network is visualized with phalloidin (red) and the nucleus is visualized with DAPI (blue). Scale bars: 50 μm. (B) Violin plot of YAP nuc/cyt ratios of individual cells on the array, grouped by the same RGD density. Data was pooled from experimental triplicates, as we did not observe systematic difference between the triplicates. (C) Violin plot of the same dataset as panel B, grouped by the same stiffness. A, B, C statistical families show $p<0.05$ from Kruskal-Wallis test for multiple comparison of non-normally distributed data. L, M, H: low, medium, and high RGD gels, respectively.

Similar to YAP nuclear localization, hMSC cell spreading was largely promoted as stiffness and RGD density increased, as indicated by F-actin staining that depicted an expanded stress fiber network (Figure 2.5A). Stiffness dependence was seen on all three RGD

densities (Figure 2.5B), and ligand density dependence was observed across all stiffness conditions (Figure 2.5C). As expected, ECM stiffness and ligand density have a synergized outcome in facilitating hMSC spreading. Overall, we validated that the array platform successfully recapitulated the expected YAP localization preference and cell spreading behaviors to stiffness and ligand density.

Interestingly, YAP nuc/cyt ratio and cell area of hMSCs under all conditions did not follow normal distributions. Instead, they both showed a long-tail distribution. Even on hydrogels with the highest stiffness and ligand density, there are still a subpopulation of hMSCs that favors cytoplasmic localization of YAP or is not well spread. Also, a small percentage of cells on soft, low RGD density gels are still capable of spreading or have YAP enriched in the nucleus. Such non-normal distribution may be due to an intrinsic heterogeneity of hMSCs.[59]

2.2.4. Human Mesenchymal Stem Cell Differentiation on the Array

We further tested if the array platform could direct mechanosensitive hMSC lineage commitment. A strong tendency to differentiate into adipocytes on soft matrices has been observed on hydrogels based on hyaluronic acid, polyacrylamide, poly(ethylene glycol) (PEG) and alginate, while stiff hydrogels largely promote hMSC osteogenesis.[13,60–62] Our lab's previous finding on combinatorial gradient HA hydrogels also indicated that soft, low fibronectin density matrices biased hMSC toward adipogenesis, while stiff, high fibronectin density matrices biased toward osteogenesis.[40] We therefore hypothesized that a similar trend would be observed on our array platform. We first evaluated whether the array is permissive for hMSC adipogenesis and osteogenesis in the presence of corresponding induction media. We seeded hMSCs on the array, allowed them to grow for 1-2 days in expansion medium, and then exposed the cells to a 1:1 mixture of adipogenic and osteogenic differentiation media. After 7 days of differentiation, we analyzed adipogenesis and osteogenesis by BODIPY staining (for lipid droplets) and alkaline phosphatase activity.

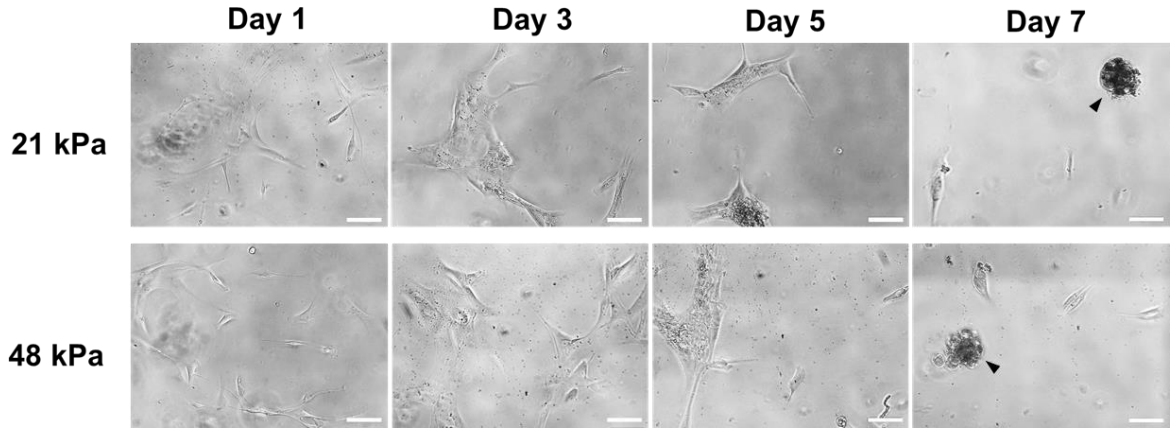

Figure 2.6. Phase contrast images of hMSCs migration on low RGD gels to form cell clusters (arrows) after cell differentiation induced with 1:1 adipogenic: osteogenic media. Scale bars: 100 μm. The image for day 7, 21 kPa was from a different field compared to day 1,3 and 5 because cells migrated out from the original field.

On hydrogels with low RGD density (0.1 mM), despite the initial attachment and spreading, hMSCs started to migrate and aggregate to form cell clusters (Figure 2.6). On day 7, most cells seeded on gels of low or moderate stiffness migrated to these clusters, suggesting that the majority of cells are no longer in direct contact with the matrix. Instead, they were sensing mostly the cells around them. We did not observe cell migration during differentiation on gels with high RGD density. On medium RGD gels, the migration behavior was somewhere in between. Oil O Red staining of the cell clusters confirmed the presence of lipid droplets. However, 5-bromo-4-chloro-3-indolyl phosphate (NBT/BCIP) staining of alkaline phosphatase activity was difficult to visualize under bright field images due to the dark color of cell clusters (data not shown).

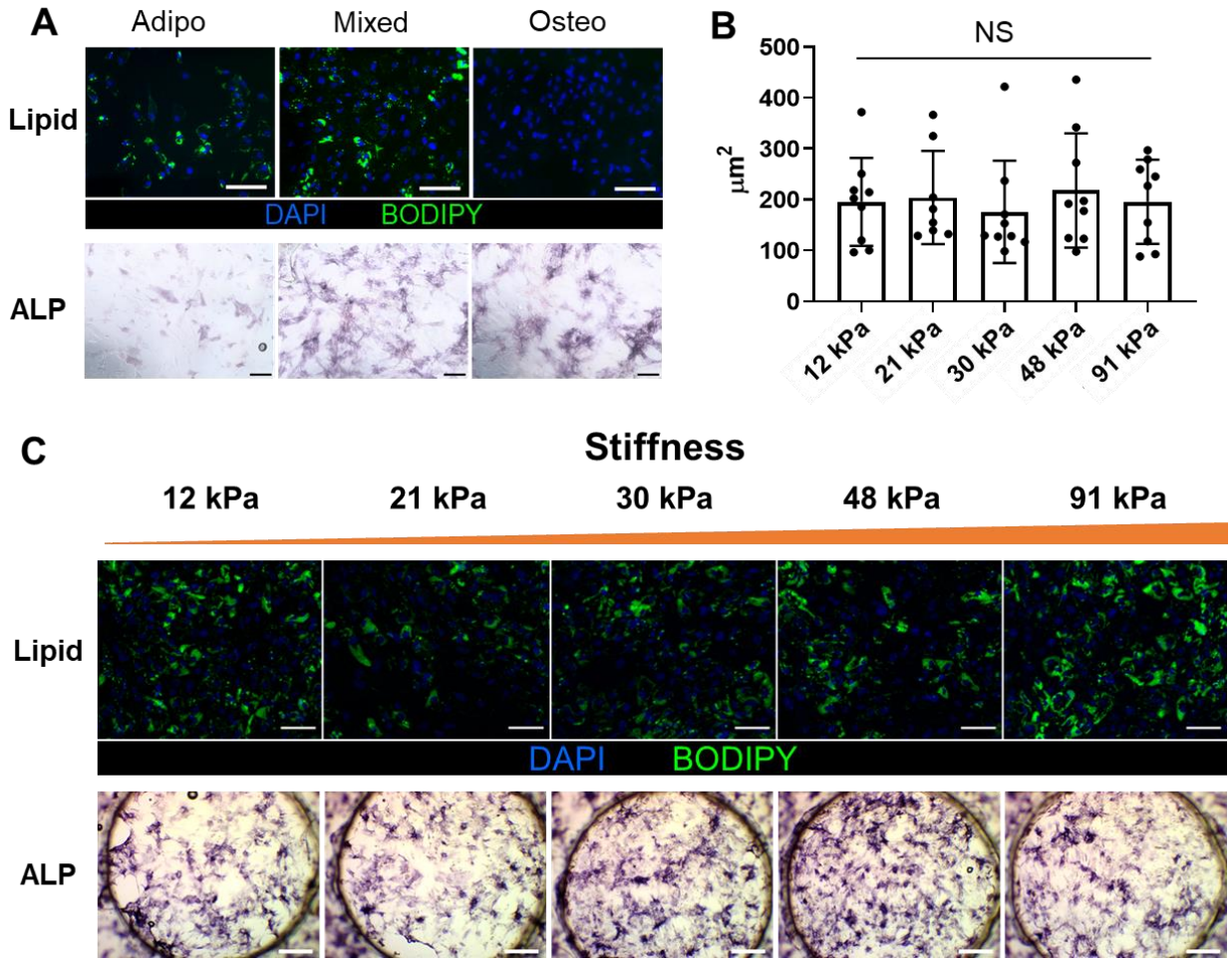

Figure 2.7. Characterization of hMSC adipogenesis and osteogenesis on the HA array platform. (A) When treated with osteogenic medium only, hMSCs did not develop any lipid droplets on day 7. When treated with adipogenic medium only, hMSCs exhibited little alkaline phosphatase activity, indicating very low level of osteogenesis. Scale bars: 200 μm. (B) When treated with 1:1 adipogenic:osteogenic mixed media, hMSCs were capable of differentiating into adipocytes and osteocytes from 12 to 91 kPa gels. A comparison of representative images from experimental replicates did not show stiffness-dependence of staining intensity. Scale bars: 100 μm (top row); 500 μm (bottom row). (C) Average lipid droplet area per cell has no statistically significant stiffness-dependence (ordinary one-way ANOVA). Data points represent analysis of individual

hydrogels from three independent differentiation experiments. Each experiment has 2 or 3 gels of the same stiffness.

To better examine the effect of cell-ECM interactions on hMSC lineage commitment, we focused on the high RGD density conditions. A control experiment using adipogenic-only or osteogenic-only induction medium validated that without soluble factors in the medium, the hydrogels alone could not induce adipogenesis or osteogenesis (Figure 2.7A). The mixed media condition can induce both lineages simultaneously. We then compared adipogenic and osteogenic efficiency across a stiffness range of 12 to 91 kPa. Surprisingly, we did not see strong stiffness-dependency of either lineage. Clear phenotypic changes of adipogenesis (lipid droplet formation) and osteogenesis stiffness (ALP activity) were found on all stiffness conditions (Figure 2.7B). We also observed large variations of the adipogenic level across experimental replicates despite that the gel conditions remained consistent (Figure 2.7C). Such batch-to-batch variation again pointed to the heterogeneity of hMSCs in their differentiation potency. We have also measured the expression levels of adipogenesis marker FABP4 and osteogenesis marker ALP across the stiffness range, yet we did not see any stiffness dependence of expression levels (data not shown).

Previous studies on the stiffness dependence of MSCs fate commitment spanned across a wide stiffness range on 2D biomaterials. The optimal modulus for adipogenesis reported ranges from several hundred pascals to 5 kPa, while stiffness above 30 kPa dramatically decreases adipogenic efficiency.[29,40,62] On the other hand, osteogenic efficiency increases along with stiffness above 21 kPa[29,52,63], but a more quantitative pattern is likely to highly depend on the hydrogel composition, adhesive ligand coating, and stem cell sources. It is also worth mentioning that the reported "optimal" stiffness for directing hMSCs to a certain lineage may also depend on the method used to characterize matrix mechanics (e.g. rheology versus AFM).

In our studies, several factors may contribute to the fact that no stiffness-dependence was observed. First, it is possible that the induction medium was so potent that it overrode any impact of matrix stiffness. In particular, the adipogenic level on 91 kPa gels was comparable to that on 12 kPa gels, whereas past studies have shown a rapid decline of adipogenesis for stiffness values exceeding 10 kPa[40,62]. Tuning down the potency of differentiation medium by optimizing concentrations of induction factors may sensitize stiffness-dependent responses. Second, the dynamic range of hydrogel stiffnesses may be insufficient to capture strong biasing of lineage commitment. The soft hydrogels of 12 kPa may still be too stiff to see a significant decline of osteogenesis or a surge of adipogenesis. Third, a small difference in cell density may also play a role in adipogenic efficiency. Despite an identical seeding density, hMSCs expanded slightly faster on stiff gels, which led to a ~20% higher cell count on day 7 of differentiation. We noticed that adipogenic efficiency significantly increased with cell density. This is consistent with previous studies which attributed such increase to cell shape changes at high density.[64,65] In this way, cell density may affect adipogenesis towards an opposite direction as stiffness goes up, thus attenuating any outcomes of stiffness sensing.

2.2.5. Shingo Adipose Tissue Preadipocyte (sWAT) Browning on the Array

Brown and beige adipose tissues are responsible for a thermogenesis process that is critical to maintain metabolic homeostasis. Induced by environmental stimuli such as cold, exercise or tissue injury, beige adipocytes mays arise from either mesenchymal stem cells *de novo* or trans-differentiation of white adipocytes, knowing as adipose tissue browning.[66] Residing in the white adipose tissues, beige adipocytes share the thermogenic capability of brown adipocytes and express uncoupling protein 1 (UCP1) for uncoupling oxidative phosphorylation.[67,68] The morphology of beige is distinctive to white adipocytes, but similar to vascular smooth muscle cells.[66,69] It is unclear what implications the cytoskeleton rearrangement of beige adipocytes may have on their thermogenic capacity. Vaicik et al. encapsulated adipose-derived MSCs in 3D PEG hydrogels of varying stiffness and found that UCP1 expression decreased from 5 to 30 kPa, suggesting that matrix mechanics may play a role in beige adipocyte thermogenesis.[70] Furthermore, Tharp et al. showed that mature white and brown adipocytes generate different degrees of cellular contractility, which is associated with the expression of distinct myosin isoforms.[71] Enhanced actomyosin tension was correlated to acute activation of uncoupled respiration and thermogenic gene expression. This finding suggested a broader possibility that adipose tissue browning may be sensitive to ECM mechanical properties that are known to regulate cellular contractility in differentiation. Interestingly, white adipogenesis of MSCs are typically a consequence of reduced cytoskeleton tension,[64,72,73] which raises the question of whether developmental signals have reactivated contractile gene expression at some point during beige differentiation. Our HA array platform may help answer this question by mediating cellular tension through altering matrix mechanics.

To this end, we studied beige differentiation of Shingo Adipose Tissue preadipocytes (sWATs) on the array platform. sWAT is an immortal cell line derived from inguinal white adipose tissue in mice models developed by Kajimura et al.[74] sWAT was used as a model system because of its potency to differentiate into either white or beige adipocytes given the appropriate induction medium. We tested whether sWATs could differentiate to beige adipocytes on the array platform. sWATs were plated on the array of high RGD gels and allowed to reach 95% confluency in expansion medium as cell-cell contact is a prerequisite for high beige adipogenic efficiency. After that, cells were treated with beige induction medium for two days, and then treated with beige maintenance medium for 3 days. Beige differentiation efficiency was evaluated by the expression levels of UCP1 and FABP4 using quantitative real-time PCR (qRT-PCR).

sWATs attached and spread normally on high RGD gels regardless of the stiffness before induction. However, after cells were exposed to the beige induction media, they started to exhibit strong cell-cell retraction forces and migrated to form cell clusters, similar to the behavior we observed from hMSCs differentiating on low RGD gels. When gel stiffness reached 200 kPa, cell aggregation was significantly suppressed (Figure 2.8A). Interestingly, when sWATs were induced with white adipogenic medium, i.e. in the absence of triiodothyronine, rosiglitazone, and indomethacin, sWATs exhibited little contraction on tissue culture plastic compared to those exposed to beige induction medium (data not shown). To our best knowledge, there have not been systematic studies to explain whether cell contraction forces are intensified in the browning process. Our observation on the array

suggests a possibility that sWATs may be under high cellular tension at the early stage of beige adipogenesis.

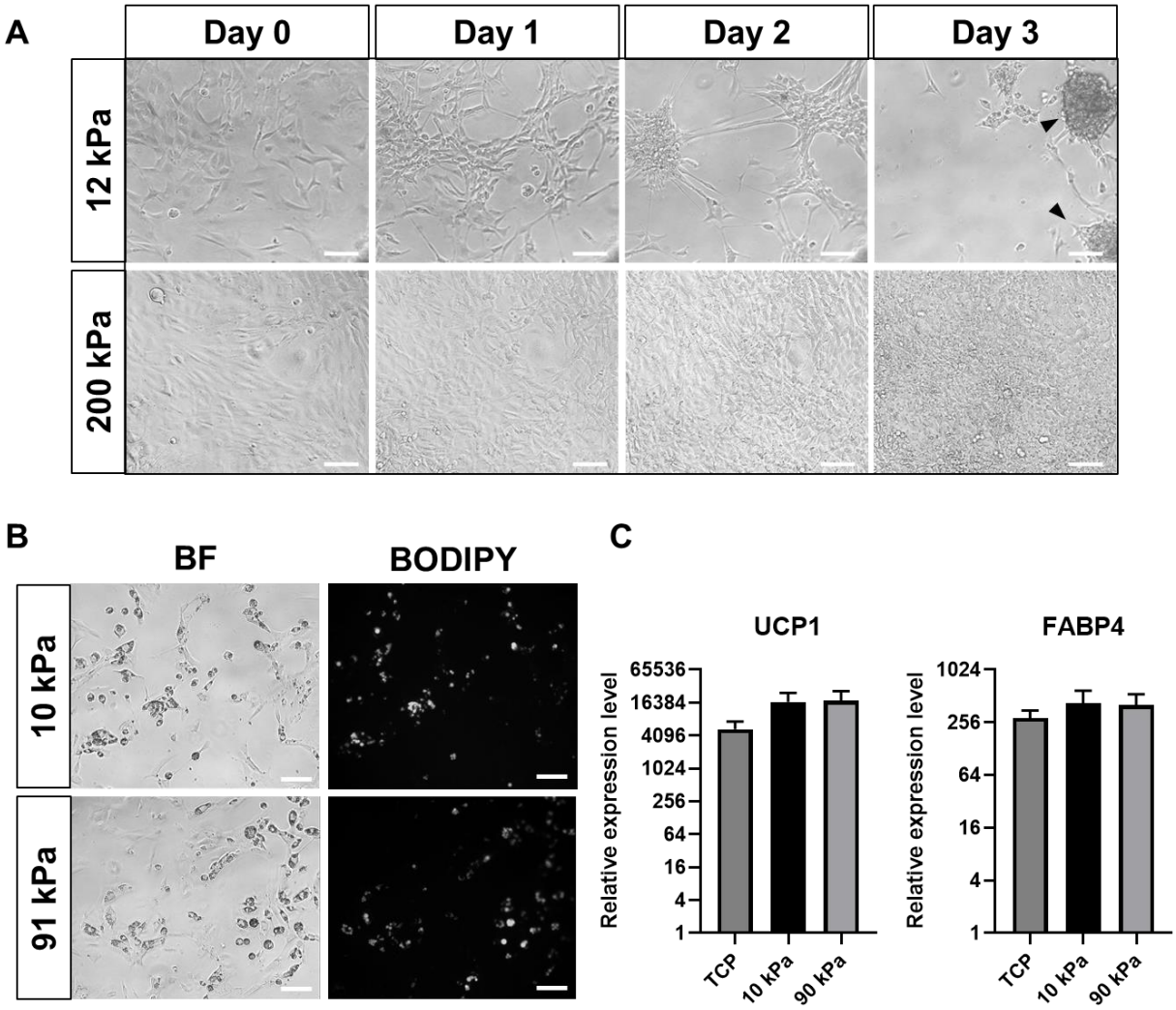

Figure 2.8. sWAT beige differentiation on HA array platform. (A) sWATs experienced significant cell-cell contraction after induced beige differentiation. On 12 kPa gels, the majority of cells had migrated to form cell clusters on day 3 of differentiation (arrows), which prevent them from interacting with the matrix. Scale bars: 100 μm (B) sWATs differentiated on tissue culture plastic for two days and reseeded onto the array platform at 10% of the original density did not aggregate, possibly due to the reduced cell density. Scale bars: 100 μm. (C) UCP1 and FABP4 expression of sWATs on day 5 after differentiation. On the gel array, both markers have comparable expression level as on tissue culture plastic. The expression levels are normalized against sWAT cells cultured in expansion media for 5 days. Inorganic pyrophosphatase (PPA1) gene was used as an internal control. N = 3 for 12 kPa and 91 kPa hydrogels. N = 2 for plastic.

To avoid formation of cell aggregates, where cell-cell interactions might dominate mechanosensing and minimize the effect of cell-matrix interactions, we reduced the cell density by "diluting" sWATs on day 2 of differentiation. Specifically, two days after beige

differentiation was induced in sWATs cultured on tissue culture plastic, cells were trypsinized and reseeded onto the array platform at 1/10 of original density, then were treated with beige maintenance medium for 3 more days. Phase contrast and BODIPY fluorescence images of sWATs on day 5 of differentiation showed that they were fully capable of forming lipid droplets (Figure 2.8B). We extracted mRNAs from these sWATs and evaluated the expression levels of UCP1 and FABP4 (Figure 2.8C). Compared to uninduced cells, both UCP1 and FABP4 were significantly upregulated, indicating robust browning.

In the case where sWATs are reseeded two days into their beige adipogenesis, the cells could not incorporate mechanical cues from the hydrogels in their early stage of differentiation because they were cultured on plastic to prevent forming cell aggregates. Our lab has reported that neural stem cells were most sensitive to matrix stiffness within 12-36 hours of differentiation.[75] We do not know yet if similar mechanosensing windows apply to sWATs, which will need further investigations. Future studies will focus on a systematic comparison of sWAT thermogenic capacity across different stiffnesses. We expect to observe a correlation between matrix stiffness and thermogenic capacity and on the array platform, which may provide clues for understanding the impact of matrix mechanosensing in beige adipogenesis.

2.3. Conclusions

We have developed a combinatorial HA-based hydrogel array in a standard 96-well plate setting, with orthogonal gradients of matrix elasticity and adhesive ligand density. Adipose-derived hMSCs responded strongly to both matrix stiffness and RGD peptide density, as high stiffness, high RGD conditions significantly promoted YAP nuclear localization and cell spreading. On the array, hMSCs are fully capable of adipogenesis and osteogenesis within the stiffness range of 12-91 kPa in the presence of RGD. sWATs expressed UCP1 and developed into beige adipocytes on the array platform. Future studies will focus on investigating the interplay between matrix mechanics and signaling factors for white versus beige adipogenesis in preadipocyte development. Our platform represents a simple strategy to fabricate combinatorial hydrogel arrays in standard multi-well culture plates, which may be adapted to broader applications for dissecting molecular mechanisms of stem cell mechanosensing.

2.4. Materials And Methods

2.4.1. Synthesis and Characterization of Methacrylated Hyaluronic Acid (HA-Me)

Hyaluronic acid powder (MW 66–90 kDa; Lifecore Technologies) was dissolved at a concentration of 1 wt% in deionized water. The solution was placed in an ice bath and a ten-fold molar excess of methacrylic anhydride (Sigma-Aldrich; relative to the HA disaccharide repeat unit) was added dropwise to the solution. The pH was controlled within 8-9 by adding 10 N NaOH in the next 6 hours. By the end of the day, pH was adjusted to 10 and the reaction was maintained at 4°C overnight. On the next day, two-fold molar excess of methacrylic anhydride was added dropwise to the solution. The reaction was then maintained at 4C for

4 more hours, with pH adjusted to 8-9 by adding 10 N NaOH. After that, the pH was adjusted to 10 and the reaction was maintained at 4°C overnight.

At the conclusion of the reaction, methacrylated HA was precipitated from the aqueous solution by adding excess cold ethanol (Proof 200 ethanol, anhydrous, Koptec). The mixture was then centrifuged at 4,000×g for 15 min and the supernatant was discarded. HA-methacrylate was then dissolved in minimal amount of deionized water, froze at -80°C, and lyophilized for 3 days. Methacrylated HA has a white, flaky appearance after lyophilization. For long-term storage, -20°C is needed.

NMR spectra of methacrylated HA was obtained by dissolving it at 3 mg/mL in deuterium oxide (D_2O, Sigma Aldrich). NMR spectra were collected at 400MHz using a Bruker Avance AVB-400 instrument. The degree of methacrylation was then calculated as the ratio of the vinylic protons from the methacrylate group to the N-acetyl methyl protons from the HA backbone, normalized to the number of protons per group.

2.4.2. Fabrication of HA Array

2.4.2.1. General Materials

RGD adhesive peptide (Ac-GCGYGRGDSPG-NH2) was synthesized and received from AnaSpec Inc, then reconstituted in 1X PBS. Dithiothreitol (DTT) was purchased from Thermo Fisher. PBS (10X) was purchased from Fisher Scientific and diluted to 1X following manufacturer's protocol. Poly-D-lysine (MW>300,000) was purchased from Sigma-Aldrich and dissolved in PBS to 1 mg/mL. PDMS was purchased from Dow Corning (SYLGARD™ 184 silicone elastomer kit). Double-sided medical tape was purchased from Adhesives Research (ARcare® 90106). Laser cutting was performed on a Full Spectrum H-series 20×12 Desktop CO_2 Laser Engraver (Full Spectrum Laser).

2.4.2.2 Mold for HA array

A piece of double-sided tape was laser cut to generate an array of 3 mm-wide circular holes, with the distance between circles being 9.02 mm (which equals to the well-to-well distance of a standard 96-well plate). A lid with an array of PDMS posts was casted by using acrylic molds. Specifically, a 1/16 inch-thick acrylic sheet was perforated by the laser cutter to generate an array of 3.3 mm-wide circular holes, with the distance between circles equals to that of the double-sided tape (Sheet A). A spacer acrylic sheet (Sheet B) with a rectangular cutout was placed on top of Sheet A, with another rectangular acrylic sheet (Sheet C) at the bottom of Sheet A (Figure 2.9). PDMS was poured into the mold, then a glass slide was placed on top and the sandwich assembly was fixed with binder clips. PDMS was cured at 80°C for at least two hours before removing from the casting mold.

One side of tape cover was removed so that the tape can be adhered to a clean glass coverslip (Fisherbrand, No. 1.5). 1 mg/mL Poly-D-lysine (PDL) solution was applied to coat the glass for at least 1 min to render the surface positively charged, so that the HA hydrogels could attach. The PDMS lid was plasma treated immediately before uses.

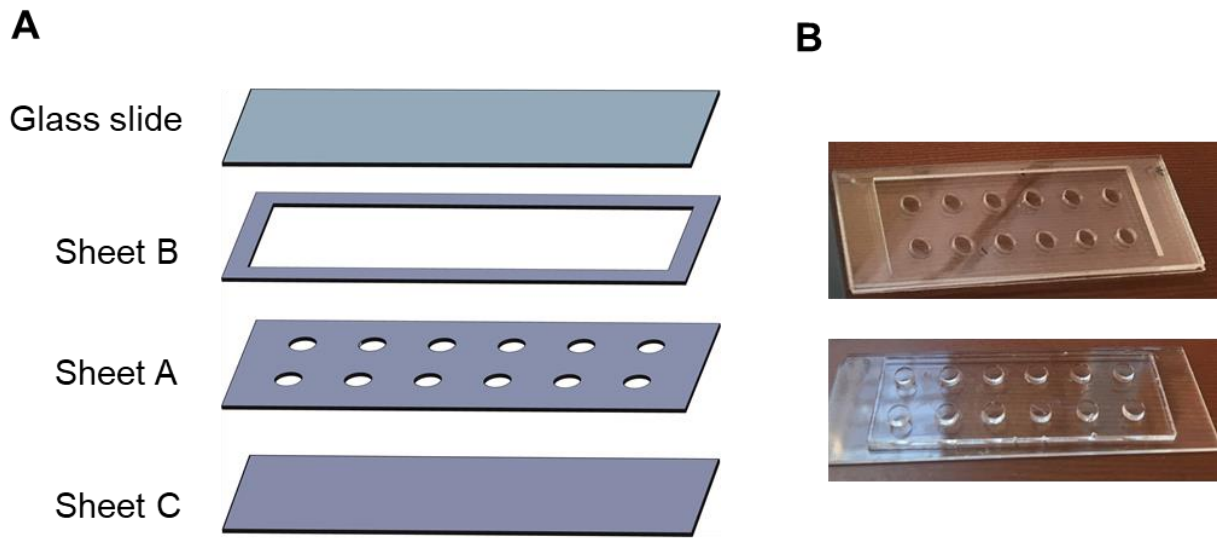

Figure 2.9. An acrylic mold for casting the multi-post PDMS lid. (A) Illustration of the acrylic mold stacking. (B) Photos of the acrylic mold (top, without the glass slide) and the resulting PDMS lid (bottom).

2.4.2.3. HA array crosslink

HA-RGD solution, depending on the final RGD concentration in the gel precursor, was made by mixing appropriate volume of 10% wt HA-me, 4 mg/mL RGD and PBS, then vortexing at room temperature for 1 hr. HA-RGD solution was mixed with 5% wt DTT to achieve a 0.15 thiol:HA repeat unit ratio, then was immediately pipetted to the PDL-treated glass area. The PDMS lid was then placed on top of the coverslip to form a sandwich assembly. The assembly was allowed to sit at room temperature in a moisturized chamber overnight for hydrogel crosslinking. On the next day, the assembly was soaked in 1X PBS to detach the PDMS lid from the gel array. Cover of the double-sided tape was removed, and the exposed adhesive surface further glued the gel array onto a bottomless 96-well black-wall culture plate (Greiner Bio-One International GmbH). For cell differentiation assays or other long-term cell culture (>1 day) experiments, sterile PBS was used at all times, plastic culture supplies were UV-disinfected and the fabrication process occurred in a biosafety hood to minimize bacteria contamination.

2.4.3. Stiffness Gradient Patterned by a Programmable Light Illumination System

Specialized illumination devices for light activation at variable amplitudes (LAVA) were used for gel photostimulation.[41] The LAVA devices were designed for 96-well plate illumination as described in[41]. In brief, the illumination intensity of a surface-mount 405 nm LED (SMT405R, Marubeni) placed at the center of each well was controlled with pulse-width modulation. User-defined intensities for each well were programmed through a graphical user interface to allow 405 nm illumination in the [0 – 33.5] $\mu W/mm^2$ intensity range. The LAVA device allowed independent control of 24 channels, so that clusters of four neighboring wells were controlled simultaneously in the 96-well format (Figure 2.2E).

Lithium phenyl-2,4,6-trimethylbenzoylphosphinate (LAP) was dissolved in PBS to make 0.5 wt % solution. 100 μL of freshly-made LAP solution was added to each well and the gels were soaked with LAP on a shaker for 1 hr at room temperature. The array was then placed on the LAVA device, exposed to 405 nm UV light (intensity measured at the center of hydrogel = 15 μW/mm^2) for various amount of time programmed by a software described in[41]. Then, the LAP solution was immediately removed and the array was washed with 1X PBS for 20 min on a shaker to remove excess LAP.

2.4.4. Atomic Force Microscope Characterization of Hydrogel Array

The hydrogel array for AFM measurement was attached to a removable plastic chamber to hold LAP solution when photocrosslinked on the LAVA device as described in 2.4.3, then the chamber was removed to enable direct contact between the AFM tip and the hydrogels. AFM was performed with a Veeco Catalyst Bioscope (Bruker Corporation, Camarillo, California, USA). The gels were indented with a pyramid-tipped probe (DNP-10; Bruker AFM Probes) with cantilever spring constants of 0.12–0.24 N/m, as measured by thermal calibration. Typically, at least 5 force curves per hydrogel were collected at different positions that are at least 100 μm apart from each other. Elastic moduli of the gels were calculated from force curves using a modified Hertz model as described.[51]

2.4.5. Cell Culture

Human primary adipose-derived mesenchymal stem cells (hMSC) were purchased from ATCC (PCS-500-001), maintained and grown in accordance with the manufacturer's recommendations. Cells were cultured and grown in mesenchymal growth medium supplemented with corresponding growth supplements (ATCC) and used at passage number < 8. sWAT cells were achieved from Professor Shingo Kajimura's laboratory at University of California, San Francisco.[74] Only passage numbers between 11 and 19 were used in the experiments. Cells were cultured and grown in expansion medium [DMEM, high glucose medium (Life Technologies) supplemented with 10% fetal bovine serum (Corning) and 1% penicillin/streptomycin (Thermo Fisher Scientific)]. Medium change was performed every two days during cell expansion.

2.4.6. hMSC Spreading Assay and Immunostaining

hMSCs were seeded on the hydrogels at a density of 5,000 - 7,500 cells/cm^2 and allowed to attach and grow for 16 to 20 hrs. Cells were then fixed with 4% paraformaldehyde (Sigma-Aldrich) in 1X PBS for 15 min at room temperature, permeabilized with 0.5% Triton X-100 (EMD Millipore, 9410) in PBS, and blocked using 5% goat serum (Thermo Fisher Scientific) in PBS. YAP was visualized using YAP (D8H1X) XP® rabbit mAb (Cell Signaling Technology). Actin filaments were visualized using AlexaFluor-546 labeled phalloidin (Thermo Fisher Scientific). Cell nuclei were visualized using 4′,6-diamidino-2-phenylindole dihydrochloride (DAPI, Sigma-Aldrich). Fluorescence imaging was performed on a Nikon Eclipse Ti epifluorescence microscope equipped with ×10 and ×20 lens. YAP nucleus/cytoplasm ratio was measured as the average intensity of YAP signal inside the nucleus divided by the average intensity of an area adjacent to the nucleus region, of similar size as the nucleus. Morphometric analysis of projected cell area was performed by thresholding the phalloidin fluorescence images to define the cell boundaries and applying automated particle shape analysis in ImageJ.

2.4.7. hMSC Differentiation and Staining

hASCs were seeded on the HA hydrogel array at a density of 20,000 cells/cm^2 and allowed to grow in expansion medium for 1 day. Cells were then treated with a mixed differentiation media, consisting of a 1:1 mixture of osteogenic and adipogenic differentiation media (StemPro kits, Thermo Fisher Scientific). Cells were maintained for 7 days in these conditions with media change every 3-4 days.

For adipogenic staining, cells were fixed with 4% paraformaldehyde for 10 min at room temperature, then washed extensively with PBS. Adipogenic differentiation was assessed by lipid droplet staining of BODIPY™ 493/503 (4,4-Difluoro-1,3,5,7,8-Pentamethyl-4-Bora-3a,4a-Diaza-s-Indacene, Invitrogen), at a 2 μM working concentration. The cells were then washed extensively with PBS prior to imaging on a Nikon Eclipse Ti epifluorescence microscope.

For osteogenic staining, fixed cells were permeabilized with 0.5% Triton X-100, then washed extensively with PBS. Osteogenic differentiation was assessed by alkaline phosphatase activity via the SigmaFast BCIP/NBT assay (Sigma-Aldrich). A working solution of BCIP/NBT was prepared as per manufacturer's instructions, added to the cells, incubated for 10 min at room temperature, and then washed in PBS extensively. Alkaline phosphatase staining was identified as a dark purple color and imaged on an Olympus IX50 inverted fluorescence phase contrast microscope, with the images captured by a Canon EOS Rebel T3 digital SLR camera.

2.4.8. sWAT Beige Differentiation and Staining

sWAT cells were seeded on the array platform at a density of 15,000 cells/cm^2 and allowed to grow in expansion medium for 1-2 day or until past 90% confluency. Cells were then treated with beige induction medium [expansion medium with 5 μM dexamethasone (TCI America, CAS 50-02-2), 500 μM 3-isobutyl-1-methylxanthine (Sigma-Aldrich, CAS 28822-58-4), 5 μg/mL HUMULIN N (isophane insulin human suspension, Eli Lilly), 1 nM L-3,3',5-triiodothyronine, sodium salt (T3, Sigma-Aldrich, CAS 55-06-1), 500 nM rosiglitazone (Rosi, Sigma-Aldrich, CAS 122320-73-4) and 125 μM indomethacin (Sigma-Aldrich, CAS 53-86-1)] for 2 days, and treated with beige maintenance medium (expansion medium with 5 μg/mL HUMULIN N, 1 nM T3, 500 nM Rosi] for 3 days. In the case that cell density was reduced to 1/10 of the original, cells were first seeded on a 24-well standard tissue culture plate on the first two days of differentiation, then trypsinized, pelleted, suspended in beige maintenance medium and reseeded to the array platform, treated with beige maintenance medium for 3 days.

Prior to staining, cells were fixed with 4% paraformaldehyde for 10 min at room temperature, permeabilized with 0.5% Triton X-100, then stained with BODIPY™ 493/503 as described in 2.4.7. to visualize lipid droplets. Cell nuclei were visualized using DAPI.

2.4.9. Real-time Polymerase Chain Reaction (RT-PCR)

Prior to cell seeding, a ring-shaped removable cover was laser cut and adhered to the bare tape region in each well of the gel array. Cells were then seeded onto the array and allowed to differentiate as described in 2.4.7. or 2.4.8. At the conclusion of the differentiation assay, this removable cover was peeled off, removing cells attached to the cover and only leaving cells attached to the hydrogel. After that, cells were lysed and RNA was extracted following the manufacturer's protocol of ReliaPrep™ RNA Miniprep systems (Promega Corporation). cDNA was synthesized using qScript™ cDNA SuperMix (Quantabio), following the manufacturers' protocols. Real-time PCR reactions were prepared with a SYBR Green qPCR Master Mix (Bimake) and the PCR cycle was performed on a BioRad CFX Connect Real-Time System™.

Primer sequences used in RT-PCR of hMSC: ALP (ACC ACC ACG AGA GTG AAC CA; CGT TGT CTG AGT ACC AGT CCC, Elimbio), FABP4 (ACG AGA GGA TGA TAA ACT GGT GG; GCG AAC TTC AGT CCA GGT CAA C, Genewiz), GAPDH (GTC AAG GCT GAG AAC GGG AA; AAA TGA GCC CCA GCC TTC TC, Elimbio)

Primer sequences used in RT-PCR of sWAT: UCP1 (CAC ACC TCC AGT CAT TAA GCC; CAA ATC AGC TTT GCC TCA CTC, Elimbio), FABP4 (CCT TTC ATA ACA CAT TCC ACC AC A; AAA TCA CCG CAG ACG ACA G, Integrated DNA Technologies), PPA1 (TTC AAC TTC CCA AAG ACC AC; CAA ACA CAA ACG GTT CCC AG, Integrated DNA Technologies)

2.5 References

(1) Discher, D. E., Mooney, D. J., and Zandstra, P. W. (2009) Growth Factors, Matrices, and Forces Combine and Control Stem Cells. *Science 324*, 1673–1677.

(2) Gattazzo, F., Urciuolo, A., and Bonaldo, P. (2014) Extracellular matrix: A dynamic microenvironment for stem cell niche. *Biochim. Biophys. Acta BBA - Gen. Subj. 1840*, 2506–2519.

(3) Smith, L. R., Cho, S., and Discher, D. E. (2017) Stem Cell Differentiation is Regulated by Extracellular Matrix Mechanics. *Physiology 33*, 16–25.

(4) Vining, K. H., and Mooney, D. J. (2017) Mechanical forces direct stem cell behaviour in development and regeneration. *Nat. Rev. Mol. Cell Biol. 18*, 728–742.

(5) Smith, Q., and Gerecht, S. (2018) Extracellular Matrix Regulation of Stem Cell Fate. *Curr. Stem Cell Rep. 4*, 13–21.

(6) Anderson, H. J., Sahoo, J. K., Ulijn, R. V., and Dalby, M. J. (2016) Mesenchymal Stem Cell Fate: Applying Biomaterials for Control of Stem Cell Behavior. *Front. Bioeng. Biotechnol. 4*, Article 38.

(7) Bao, M., Xie, J., and Huck, W. T. S. (2018) Recent Advances in Engineering the Stem Cell Microniche in 3D. *Adv. Sci. 5*, 1800448.

(8) Madl, C. M., and Heilshorn, S. C. (2018) Engineering Hydrogel Microenvironments to Recapitulate the Stem Cell Niche. *Annu. Rev. Biomed. Eng. 20*, 21–47.

(9) Geckil, H., Xu, F., Zhang, X., Moon, S., and Demirci, U. (2010) Engineering hydrogels as extracellular matrix mimics. *Nanomed. 5*, 469–484.

(10) Zhu, J., and Marchant, R. E. (2011) Design properties of hydrogel tissue-engineering scaffolds. *Expert Rev. Med. Devices 8*, 607–626.

(11) Kyburz, K. A., and Anseth, K. S. (2015) Synthetic Mimics of the Extracellular Matrix: How Simple is Complex Enough? *Ann. Biomed. Eng. 43*, 489–500.

(12) Xing, H., Lee, H., Luo, L., and Kyriakides, T. R. (2019) Extracellular matrix-derived biomaterials in engineering cell function. *Biotechnol. Adv.* 107421.

(13) Huebsch, N., Arany, P. R., Mao, A. S., Shvartsman, D., Ali, O. A., Bencherif, S. A., Rivera-Feliciano, J., and Mooney, D. J. (2010) Harnessing traction-mediated manipulation of the cell/matrix interface to control stem-cell fate. *Nat. Mater. 9*, 518–526.

(14) Chaudhuri, O., Gu, L., Klumpers, D., Darnell, M., Bencherif, S. A., Weaver, J. C., Huebsch, N., Lee, H., Lippens, E., Duda, G. N., and Mooney, D. J. (2016) Hydrogels with tunable stress relaxation regulate stem cell fate and activity. *Nat. Mater. 15*, 326–334.

(15) Xia, T., Liu, W., and Yang, L. (2017) A review of gradient stiffness hydrogels used in tissue engineering and regenerative medicine. *J. Biomed. Mater. Res. A 105*, 1799–1812.

(16) Engler, A., Bacakova, L., Newman, C., Hategan, A., Griffin, M., and Discher, D. (2004) Substrate Compliance versus Ligand Density in Cell on Gel Responses. *Biophys. J. 86*, 617–628.

(17) Rowlands, A. S., George, P. A., and Cooper-White, J. J. (2008) Directing osteogenic and myogenic differentiation of MSCs: interplay of stiffness and adhesive ligand presentation. *Am. J. Physiol.-Cell Physiol. 295*, C1037–C1044.

(18) Kilian Kristopher A., and Mrksich Milan. (2012) Directing Stem Cell Fate by Controlling the Affinity and Density of Ligand–Receptor Interactions at the Biomaterials Interface. *Angew. Chem. Int. Ed. 51*, 4891–4895.

(19) Wilson, M. J., Jiang, Y., Yañez-Soto, B., Liliensiek, S., Murphy, W. L., and Nealey, P. F. (2012) Arrays of topographically and peptide-functionalized hydrogels for analysis of biomimetic extracellular matrix properties. *J. Vac. Sci. Technol. B 30*, 06F903.

(20) Guo, Z., Hu, K., Sun, J., Zhang, T., Zhang, Q., Song, L., Zhang, X., and Gu, N. (2014) Fabrication of Hydrogel with Cell Adhesive Micropatterns for Mimicking the Oriented Tumor-Associated Extracellular Matrix. *ACS Appl. Mater. Interfaces 6*, 10963–10968.

(21) Gong, Z., Szczesny, S. E., Caliari, S. R., Charrier, E. E., Chaudhuri, O., Cao, X., Lin, Y., Mauck, R. L., Janmey, P. A., Burdick, J. A., and Shenoy, V. B. (2018) Matching material and cellular timescales maximizes cell spreading on viscoelastic substrates. *Proc. Natl. Acad. Sci.* 201716620.

(22) Zhou, Q., Ge, L., Guimarães, C. F., Kühn, P. T., Yang, L., and Rijn, P. van. (2018) Development of a Novel Orthogonal Double Gradient for High-Throughput Screening of Mesenchymal Stem Cells–Materials Interaction. *Adv. Mater. Interfaces 5*, 1800504.

(23) Hou, Y., Yu, L., Xie, W., Camacho, L. C., Zhang, M., Chu, Z., Wei, Q., and Haag, R. (2020) Surface Roughness and Substrate Stiffness Synergize To Drive Cellular Mechanoresponse. *Nano Lett. 20*, 748–757.

(24) Darnell, M., Gu, L., and Mooney, D. (2018) RNA-seq reveals diverse effects of substrate stiffness on mesenchymal stem cells. *Biomaterials 181*, 182–188.

(25) Liu, X., Liu, R., Gu, Y., and Ding, J. (2017) Nonmonotonic Self-Deformation of Cell Nuclei on Topological Surfaces with Micropillar Array. *ACS Appl. Mater. Interfaces 9*, 18521–18530.

(26) D. Hansen, T., T. Koepsel, J., Nhi Le, N., H. Nguyen, E., Zorn, S., Parlato, M., G. Loveland, S., P. Schwartz, M., and L. Murphy, W. (2014) Biomaterial arrays with defined adhesion ligand densities and matrix stiffness identify distinct phenotypes for tumorigenic and non-tumorigenic human mesenchymal cell types. *Biomater. Sci. 2*, 745–756.

(27) Guermani, E., Shaki, H., Mohanty, S., Mehrali, M., Arpanaei, A., Gaharwar, A. K., and Dolatshahi-Pirouz, A. (2016) Engineering complex tissue-like microgel arrays for evaluating stem cell differentiation. *Sci. Rep. 6*, 30445.

(28) Richardson, T. C., Mathew, S., Candiello, J. E., Goh, S. K., Kumta, P. N., and Banerjee, I. (2018) Development of an Alginate Array Platform to Decouple the Effect of Multiparametric Perturbations on Human Pluripotent Stem Cells During Pancreatic Differentiation. *Biotechnol. J. 13*, 1700099.

(29) Hadden, W. J., Young, J. L., Holle, A. W., McFetridge, M. L., Kim, D. Y., Wijesinghe, P., Taylor-Weiner, H., Wen, J. H., Lee, A. R., Bieback, K., Vo, B.-N., Sampson, D. D., Kennedy, B. F., Spatz, J. P., Engler, A. J., and Choi, Y. S. (2017) Stem cell migration and mechanotransduction on linear stiffness gradient hydrogels. *Proc. Natl. Acad. Sci. 114*, 5647–5652.

(30) Vega, S. L., Kwon, M. Y., Song, K. H., Wang, C., Mauck, R. L., Han, L., and Burdick, J. A. (2018) Combinatorial hydrogels with biochemical gradients for screening 3D cellular microenvironments. *Nat. Commun. 9*, 614.

(31) Tong, X., Jiang, J., Zhu, D., and Yang, F. (2016) Hydrogels with Dual Gradients of Mechanical and Biochemical Cues for Deciphering Cell-Niche Interactions. *ACS Biomater. Sci. Eng. 2*, 845–852.

(32) Vincent, L. G., Choi, Y. S., Alonso-Latorre, B., Álamo, J. C. del, and Engler, A. J. (2013) Mesenchymal stem cell durotaxis depends on substrate stiffness gradient strength. *Biotechnol. J. 8*, 472–484.

(33) Ranga, A., Gobaa, S., Okawa, Y., Mosiewicz, K., Negro, A., and Lutolf, M. P. (2014) 3D niche microarrays for systems-level analyses of cell fate. *Nat. Commun. 5*, 1–10.

(34) Dolatshahi-Pirouz, A., Nikkhah, M., Gaharwar, A. K., Hashmi, B., Guermani, E., Aliabadi, H., Camci-Unal, G., Ferrante, T., Foss, M., Ingber, D. E., and Khademhosseini, A. (2014) A combinatorial cell-laden gel microarray for inducing osteogenic differentiation of human mesenchymal stem cells. *Sci. Rep. 4*, 1–9.

(35) Simon, C. G., Yang, Y., Thomas, V., Dorsey, S. M., and Morgan, A. W. (2009) Cell interactions with biomaterials gradients and arrays. *Comb. Chem. High Throughput Screen. 12*, 544–553.

(36) Caliari, S. R., Gonnerman, E. A., Grier, W. K., Weisgerber, D. W., Banks, J. M., Alsop, A. J., Lee, J.-S., Bailey, R. C., and Harley, B. A. C. (2015) Collagen Scaffold Arrays for Combinatorial Screening of Biophysical and Biochemical Regulators of Cell Behavior. *Adv. Healthc. Mater. 4*, 58–64.

(37) Mih, J. D., Sharif, A. S., Liu, F., Marinkovic, A., Symer, M. M., and Tschumperlin, D. J. (2011) A Multiwell Platform for Studying Stiffness-Dependent Cell Biology. *PLoS ONE 6*, e19929.

(38) Díaz-Bello, B., Monroy-Romero, A. X., Pérez-Calixto, D., Zamarrón-Hernández, D., Serna-Marquez, N., Vázquez-Victorio, G., and Hautefeuille, M. (2019) Method for the Direct Fabrication of Polyacrylamide Hydrogels with Controlled Stiffness in Polystyrene Multiwell Plates for Mechanobiology Assays. *ACS Biomater. Sci. Eng. 5*, 4219–4227.

(39) Hribar, K. C., and Buckley, P. (2018, January 11) Apparatus for patterning hydrogels into multi-well plates.

(40) Rape, A. D., Zibinsky, M., Murthy, N., and Kumar, S. (2015) A synthetic hydrogel for the high-throughput study of cell–ECM interactions. *Nat. Commun. 6*, 8129.

(41) Repina, N. A., McClave, T., Bao, X., Kane, R. S., and Schaffer, D. V. (2019) Engineered illumination devices for optogenetic control of cellular signaling dynamics. *bioRxiv* https://doi.org/10.1101/675892.

(42) Highley, C. B., Prestwich, G. D., and Burdick, J. A. (2016) Recent advances in hyaluronic acid hydrogels for biomedical applications. *Curr. Opin. Biotechnol. 40*, 35–40.

(43) Wolf, K. J., and Kumar, S. (2019) Hyaluronic Acid: Incorporating the Bio into the Material. *ACS Biomater. Sci. Eng. 5*, 3753–3765.

(44) Ananthanarayanan, B., Kim, Y., and Kumar, S. (2011) Elucidating the mechanobiology of malignant brain tumors using a brain matrix-mimetic hyaluronic acid hydrogel platform. *Biomaterials 32*, 7913–7923.

(45) Kim, Y., and Kumar, S. (2014) CD44-Mediated Adhesion to Hyaluronic Acid Contributes to Mechanosensing and Invasive Motility. *Mol. Cancer Res. 12*, 1416–1429.

(46) Kim, I. L., Khetan, S., Baker, B. M., Chen, C. S., and Burdick, J. A. (2013) Fibrous hyaluronic acid hydrogels that direct MSC chondrogenesis through mechanical and adhesive cues. *Biomaterials 34*, 5571–5580.

(47) Cosgrove, B. D., Mui, K. L., Driscoll, T. P., Caliari, S. R., Mehta, K. D., Assoian, R. K., Burdick, J. A., and Mauck, R. L. (2016) N-cadherin adhesive interactions modulate matrix mechanosensing and fate commitment of mesenchymal stem cells. *Nat. Mater. 15*, 1297–1306.

(48) Zustiak, S., Nossal, R., and Sackett, D. L. (2014) Multiwell stiffness assay for the study of cell responsiveness to cytotoxic drugs. *Biotechnol. Bioeng. 111*, 396–403.

(49) Syed, S., Karadaghy, A., and Zustiak, S. (2015) Simple Polyacrylamide-based Multiwell Stiffness Assay for the Study of Stiffness-dependent Cell Responses. *JoVE J. Vis. Exp.* e52643.

(50) Hu, J., Gondarenko, A. A., Dang, A. P., Bashour, K. T., O'Connor, R. S., Lee, S., Liapis, A., Ghassemi, S., Milone, M. C., Sheetz, M. P., Dustin, M. L., Kam, L. C., and Hone, J. C. (2016) High-Throughput Mechanobiology Screening Platform Using Micro- and Nanotopography. *Nano Lett. 16*, 2198–2204.

(51) MacKay, J. L., and Kumar, S. (2012) Measuring the Elastic Properties of Living Cells with Atomic Force Microscopy Indentation, in *Cell Imaging Techniques* (Taatjes, D. J., and Roth, J., Eds.), pp 313–329. Humana Press, Totowa, NJ.

(52) Engler, A. J., Sen, S., Sweeney, H. L., and Discher, D. E. (2006) Matrix Elasticity Directs Stem Cell Lineage Specification. *Cell 126*, 677–689.

(53) Nemir, S., and West, J. L. (2010) Synthetic Materials in the Study of Cell Response to Substrate Rigidity. *Ann. Biomed. Eng. 38*, 2–20.

(54) Dupont, S., Morsut, L., Aragona, M., Enzo, E., Giulitti, S., Cordenonsi, M., Zanconato, F., Le Digabel, J., Forcato, M., Bicciato, S., Elvassore, N., and Piccolo, S. (2011) Role of YAP/TAZ in mechanotransduction. *Nature 474*, 179–183.

(55) Das, A., Fischer, R. S., Pan, D., and Waterman, C. M. (2016) YAP Nuclear Localization in the Absence of Cell-Cell Contact Is Mediated by a Filamentous Actin-dependent, Myosin II- and Phospho-YAP-independent Pathway during Extracellular Matrix Mechanosensing. *J. Biol. Chem. 291*, 6096–6110.

(56) Stanton, A. E., Tong, X., Lee, S., and Yang, F. (2019) Biochemical Ligand Density Regulates Yes-Associated Protein Translocation in Stem Cells through Cytoskeletal Tension and Integrins. *ACS Appl. Mater. Interfaces 11*, 8849–8857.

(57) Park, J. S., Chu, J. S., Tsou, A. D., Diop, R., Tang, Z., Wang, A., and Li, S. (2011) The effect of matrix stiffness on the differentiation of mesenchymal stem cells in response to TGF-β. *Biomaterials 32*, 3921–3930.

(58) Lee, J. P., Kassianidou, E., MacDonald, J. I., Francis, M. B., and Kumar, S. (2016) N-terminal specific conjugation of extracellular matrix proteins to 2-pyridinecarboxaldehyde functionalized polyacrylamide hydrogels. *Biomaterials 102*, 268–276.

(59) Wilson, A., Hodgson-Garms, M., Frith, J. E., and Genever, P. (2019) Multiplicity of Mesenchymal Stromal Cells: Finding the Right Route to Therapy. *Front. Immunol. 10*, Article 1112.

(60) Zhao, W., Li, X., Liu, X., Zhang, N., and Wen, X. (2014) Effects of substrate stiffness on adipogenic and osteogenic differentiation of human mesenchymal stem cells. *Mater. Sci. Eng. C 40*, 316–323.

(61) Ye, K., Wang, X., Cao, L., Li, S., Li, Z., Yu, L., and Ding, J. (2015) Matrix Stiffness and Nanoscale Spatial Organization of Cell-Adhesive Ligands Direct Stem Cell Fate. *Nano Lett. 15*, 4720–4729.

(62) Lee, J., Abdeen, A. A., Tang, X., Saif, T. A., and Kilian, K. A. (2016) Matrix directed adipogenesis and neurogenesis of mesenchymal stem cells derived from adipose tissue and bone marrow. *Acta Biomater. 42*, 46–55.

(63) Hsieh, W.-T., Liu, Y.-S., Lee, Y., Rimando, M. G., Lin, K., and Lee, O. K. (2016) Matrix dimensionality and stiffness cooperatively regulate osteogenesis of mesenchymal stromal cells. *Acta Biomater. 32*, 210–222.

(64) McBeath, R., Pirone, D. M., Nelson, C. M., Bhadriraju, K., and Chen, C. S. (2004) Cell Shape, Cytoskeletal Tension, and RhoA Regulate Stem Cell Lineage Commitment. *Dev. Cell 6*, 483–495.

(65) Wiesner, M., Berberich, O., Hoefner, C., Blunk, T., and Bauer-Kreisel, P. (2018) Gap junctional intercellular communication in adipose-derived stromal/stem cells is cell density-dependent and positively impacts adipogenic differentiation. *J. Cell. Physiol. 233*, 3315–3329.

(66) Wang, W., and Seale, P. (2016) Control of brown and beige fat development. *Nat. Rev. Mol. Cell Biol. 17*, 691–702.

(67) Bartelt, A., and Heeren, J. (2014) Adipose tissue browning and metabolic health. *Nat. Rev. Endocrinol. 10*, 24–36.

(68) Ikeda, K., Maretich, P., and Kajimura, S. (2018) The Common and Distinct Features of Brown and Beige Adipocytes. *Trends Endocrinol. Metab. 29*, 191–200.

(69) Long, J. Z., Svensson, K. J., Tsai, L., Zeng, X., Roh, H. C., Kong, X., Rao, R. R., Lou, J., Lokurkar, I., Baur, W., Castellot, J. J., Rosen, E. D., and Spiegelman, B. M. (2014) A smooth muscle-like origin for beige adipocytes. *Cell Metab. 19*, 810–820.

(70) Vaicik, M. K., Morse, M., Blagajcevic, A., Rios, J., Larson, J. C., Yang, F., Cohen, R. N., Papavasiliou, G., and Brey, E. M. (2015) Hydrogel-based engineering of beige adipose tissue. *J. Mater. Chem. B 3*, 7903–7911.

(71) Tharp, K. M., Kang, M. S., Timblin, G. A., Dempersmier, J., Dempsey, G. E., Zushin, P.-J. H., Benavides, J., Choi, C., Li, C. X., Jha, A. K., Kajimura, S., Healy, K. E., Sul, H. S., Saijo, K., Kumar, S., and Stahl, A. (2018) Actomyosin-Mediated Tension Orchestrates Uncoupled Respiration in Adipose Tissues. *Cell Metab. 27*, 602-615.e4.

(72) Kilian, K. A., Bugarija, B., Lahn, B. T., and Mrksich, M. (2010) Geometric cues for directing the differentiation of mesenchymal stem cells. *Proc. Natl. Acad. Sci. 107*, 4872–4877.

(73) Lv, H., Li, L., Sun, M., Zhang, Y., Chen, L., Rong, Y., and Li, Y. (2015) Mechanism of regulation of stem cell differentiation by matrix stiffness. *Stem Cell Res. Ther. 6*, 103.

(74) Galmozzi, A., Sonne, S. B., Keylin, S., Hasegawa, Y., Shinoda, K., Luijten, I. H. N., Chang, J. W., Sharp, L. Z., Cravatt, B. F., Saez, E., and Kajimura, S. (2014) ThermoMouse: an in vivo model to identify modulators of UCP1 expression in brown adipose tissue. *Cell Rep. 9*, 1584–1593.

(75) Rammensee, S., Kang, M. S., Georgiou, K., Kumar, S., and Schaffer, D. V. (2017) Dynamics of Mechanosensitive Neural Stem Cell Differentiation. *STEM CELLS 35*, 497–506.

Chapter 3

Structural Regulation of a Neurofilament-inspired Intrinsically Disordered Protein Brush by Multisite Phosphorylation

Abstract

Intrinsically disordered proteins (IDPs) play central roles in numerous cellular processes. While IDP structure and function are often regulated by multisite phosphorylation, the biophysical mechanisms linking these post-translational modifications to IDP structure remain elusive. For example, the intrinsically disordered C-terminal sidearm domain of the neurofilament heavy subunit (NFH-SA) forms a dense brush along axonal NF backbones and is subject to extensive serine phosphorylation. Yet, biophysical insight into the relationship between phosphorylation and structure has been limited by the lack of paradigms in which NF brush conformational responses can be measured in the setting of controlled phosphorylation. Here, we approach this question by immobilizing a recombinant NFH-SA (rNFH-SA) as IDP brushes onto glass, and controllably phosphorylating the sequence in situ with mitogen-activated protein kinase 1 (ERK2) pre-activated by mitogen-activated protein kinase kinase (MKK). We then monitor brush height changes using atomic force microscopy, which shows that phosphorylation induces significant brush swelling to an extent that strongly depends upon pH and ionic strength, consistent with a mechanism in which phosphorylation regulates brush structure through local electrostatic interactions. Further consistent with this mechanism, the phosphorylated rNFH-SA brush may be dramatically condensed with micromolar concentrations of divalent cations. Phosphorylation-induced height changes are qualitatively reversible via alkaline phosphatase-mediated dephosphorylation. Our study demonstrates that multisite phosphorylation controls NFH-SA structure through modulation of chain electrostatics and points to a general strategy for engineering IDP-based interfaces that can be reversibly and dynamically modulated by enzymes.

The studies described in this chapter were conducted in collaboration with Jessica Pui Yan Lee and is part of a peer-reviewed publication. (Lei, R., Lee, J. P., Francis, M. B., and Kumar, S. Structural Regulation of a Neurofilament-Inspired Intrinsically Disordered Protein Brush by Multisite Phosphorylation. *Biochemistry*. 57: 4019-4028) This chapter was reproduced with permission from all co-authors.

3.1 Introduction

Intrinsically disordered proteins (IDPs) are prevalent in biological systems and regulate several critical cellular processes including cell differentiation, transcription, cell cycle regulation, signaling and neurogenesis.[1,2] Because IDPs often lack a compact hydrophobic core, they can be highly accessible to post-translational modifications (PTMs),[3] which have been reported to regulate a number of function-driving properties, including structure,[4] protein-binding function,[5] phase transitions,[6] and degradation.[7] Phosphorylation represents the most common type of PTM in IDPs,[1,8] with serine, threonine, and tyrosine phosphorylation all observed to alter IDP structure and protein-protein interactions. Notably, IDPs frequently contain regions that are subject to multisite phosphorylation.[8,9] Regulation of IDP structure by multisite phosphorylation has been explored in a variety of systems,[10–13] revealing a highly complex and context-dependent relationship in which phosphorylation may modulate conformation in either a continuous or discrete, switch-like manner.[4,5]

Importantly, the vast majority of these efforts have characterized IDPs in dilute solution. In many biological contexts, however, IDPs are presented on scaffold-like surfaces, raising the possibility that IDP conformation and phospho-sensitivity may be a function of both inter- and intra-IDP interactions. Such IDP arrays, which have been likened to synthetic "polymer brush" coatings, play important roles in controlling transit through nuclear pores, as well as in the structure and mechanics of cytoskeletal networks.[14–16] Neurofilaments (NFs), the key intermediate filament in large myelinated axons, offer a particularly insightful example. NFs run in parallel, cable-like arrays along the length of the axon and play a central role in modulating axon radial growth and caliber.[17] The C-terminal sidearm domains of neurofilament subunits are IDPs that protrude from the rod-like filament backbone and mediate NF-NF spacing by producing a zone of steric exclusion around the NF core.[18,19] In mammals, the NF heavy subunit (NF-H) sidearm domain typically contains 40-60 phosphorylation sites, mostly in the context of lysine-serine-proline (KSP) repeats. NF phosphorylation has been functionally linked to NF assembly, transport, and spacing within the axon,[20,21] and alterations in NF phosphorylation have been associated with a number of neurodegenerative diseases.[22,23] KSP phosphorylation converts the NF-H sequence from a nearly perfect and well-mixed polyampholyte to a polyanion under physiological pH, raising the possibility that phosphorylation may modulate NF conformation through local electrostatic effects. This idea is supported by both computational[24–26] and experimental studies.[19,27,28] Despite the broad consensus around the importance of electrostatic effects in controlling NF sidearm conformation, key mechanistic details remain controversial.[29] For example, it is not clear whether phosphate-phosphate repulsions are sufficient to overcome potential attractive interactions between oppositely charged residues (e.g. lysine and glutamate) on adjacent sidearms.[30] It is also unclear whether the tendency of phosphates to swell the sidearm might be offset by the abundant prolines, which have recently been proposed to structurally "buffer" phosphate-driven conformational changes in IDPs.[13]

Part of this controversy may originate from the fact that many mechanistic hypotheses relating NF phosphorylation to structure have been indirectly inferred from studies with assemblies of purified and fully assembled NFs, including reconstituted NF hydrogels.[19,31–33] While phosphorylation-induced network expansion and collapse have been observed in

these systems, the response to changes in electrostatic milieu (pH, ionic strength) can be subtle, and the interpretation of the results is confounded to some degree by effects of electrostatics on NF assembly and entanglement, both of which influence gel structure. As a result, there is a need for paradigms in which NF sidearms (and IDPs in general) can be reconstituted in assemblies that feature intra- and intermolecular interactions, enable phosphorylation, and can be conformationally probed. By analogy, such reconstitution approaches have produced great insight into sequence-structure relationships for synthetic polymers, where expansion and collapse of polymer brushes have been used to decipher molecular regulatory principles.[34,35]

To address this need, we developed an experimental IDP brush system in which a recombinant NF-H sidearm domain (rNFH-SA) was surface-immobilized in an oriented fashion and probed with atomic force microscopy (AFM).[36] For the native (i.e. non-phosphorylated) sequence, we observed strongly pH- and ionic strength-dependent conformational transitions, with brush thickness largely correlated with formal charges along the chain. These brushes could be enzymatically modified, with brush height reduced to predictable levels with site-directed proteolysis. To gain further insight into potential effects of phosphorylation, we later created and characterized 32-residue peptide versions of these molecules (containing 4 KSP repeats) in which we mimicked electrostatic effects of phosphorylation through mutagenesis (KSP to KDP).[37] KDP peptides swelled to a greater degree than KSP peptides, consistent with a model in which phosphate-phosphate repulsion drives conformational properties. However, aspartate replacement may not fully capture electrostatic effects of phosphorylation,[38] and it is challenging to infer conformational properties of the entire NF sequence from such short peptides.

To enable the systematic study of IDP multisite phosphorylation on conformational properties, we now present a system in which full-length NF-H sidearm brush may be enzymatically phosphorylated and dephosphorylated in solution and in surface-immobilized brushes. We find that KSP phosphorylation produces a dramatic swelling of the grafted brush and produces pH- and ionic strength-dependent properties characteristic of a strong polyanion. Moreover, phosphorylated brushes may be condensed with micromolar concentrations of divalent cations. By enzymatically phosphorylating the native IDP and probing its conformational changes in a well-defined protein brush system, this work offers a new method to study the effects of multisite phosphorylation events on IDP structure and function. It also provides insight into biophysical mechanisms of NF assembly.

3.2 Results and Discussion

3.2.1 Recombinant NFH-SA Expression and Purification

In a previous study, we used an engineered recombinant NFH-SA construct containing residues 426-1066 from the rat NF-H sidearm domain with a tetra-cysteine tag on the N-terminus.[36] For the current study, to facilitate protein purification and mass spectrometry, we used a very similar construct in which we reduced the number of cysteines from four to one and moved this cysteine to the C-terminus. The full protein sequence is shown in Figure 3.1. This modified construct, hereafter simply referred to as rNFH-SA, contains 50 KSP repeats and a large and nearly equal number of positively charged (Glu and Asp) and

negatively charged residues (Lys and Arg), rendering the unmodified sequence polyampholytic (net neutral) at physiological pH. At the C-terminus, the construct also features a 6xHis tag enable protein purification by immobilized metal affinity chromatography, and aromatic residues (YW) to facilitate concentration measurements by absorbency.

We expressed rNFH-SA in *Escherichia coli* and purified the protein with a Ni-NTA resin. (Figure 3.2A). Due to the high charge numbers, rNFH-SA may have a lower affinity for sodium dodecyl sulfate (SDS) in electrophoresis and thus exhibit a higher apparent molecular weight on SDS-PAGE, which is ~120 kDa compared to the actual molecular weight of 70 kDa. Deconvoluted ESI-TOF MS spectra validated the identity of rNFH-SA (Figure 3.2B).

SEFTSMSTHIKVKSEEKIKVVEKSEKETVIVEEQTEEIQVTEEVTEEEDKEAQGEEEEEAEEGGEEAATTSPP
AEEAASPEKETKSPVKEEAKSPAEAKSPAEAKSPAEAKSPAEVKSPAVAKSPAEVKSPAEVKSPAEAKSP
AEAKSPAEVKSPATVKSPGEAKSPAEAKSPAEVKSPVEAKSPAEAKSPASVKSPGEAKSPAEAKSPAEVK
SPATVKSPVEAKSPAEVKSPVTVKSPAEAKSPVEVKSPASVKSPSEAKSPAGAKSPAEAKSPVVAKSPAE
AKSPAEAKPPAEAKSPAEAKSPAEAKSPAEAKSPAEAKSPVEVKSPEKAKSPVKEGAKSLAEAKSPEKAK
SPVKEEIKPPAEVKSPEKAKSPMKEEAKSPEKAKTLDVKSPEAKTPAKEEAKRPADIRSPEQVKSPAKEEA
KSPEKEETRTEKVAPKKEEVKSPVEEVKAKEPPKKVEEEKTPATPKTEVKESKKDEAPKEAQKPKAEEKE
PLTEKPKDSPGEAKKEEAKEKKAAAPEEETPAKLGVKEEAKPKEKAEDAKAKEPSKPSEKEKPKKEEVPAA
PEKKDTKEEKTTESKKPEEKPKMEAKAKEEDKGLPQEPSKPKTEKAEKSSSTDQKDSQPSEKAPEDKLYW
CLVPRGSWSHPQFEKASHHHHHH

Figure 3.1. Full amino acid sequence of rNFH-SA. The 50 KSP repeats (red), the cysteine for surface immobilization (blue), and phosphorylatable residues other than Ser in KSP repeats (green) are highlighted.

3.2.2 rNFH-SA Phosphorylation *in vitro* by Recombinant ERK2 and MKK

To investigate how phosphorylation might affect rNFH-SA structure, we first sought to develop an enzymatic strategy in which we could specifically phosphorylate KSP serines with kinases and then reverse this modification with a phosphatase. The mitogen-activated protein kinase (MAPK) pathway is the major mechanism for the phosphorylation of KSP repeats *in vivo*,[41,43] involving upstream activation of mitogen-activated protein kinase 1 (also known as the extracellular signal-regulated kinase 2, ERK2) by mitogen-activated protein kinase kinase (MAP2K1, or MKK). ERK2/MKK-based phosphorylation has previously been used to phosphorylate purified recombinant NF-H *in vitro* to map phosphorylation sites.[41] Inspired by this strategy, we chose an ERK2/MKK-based system to phosphorylate our rNFH-SA construct. We expressed ERK2 and MKK in *Escherichia coli* and purified both the IDP and the kinases by affinity chromatography (Figure 3.3).

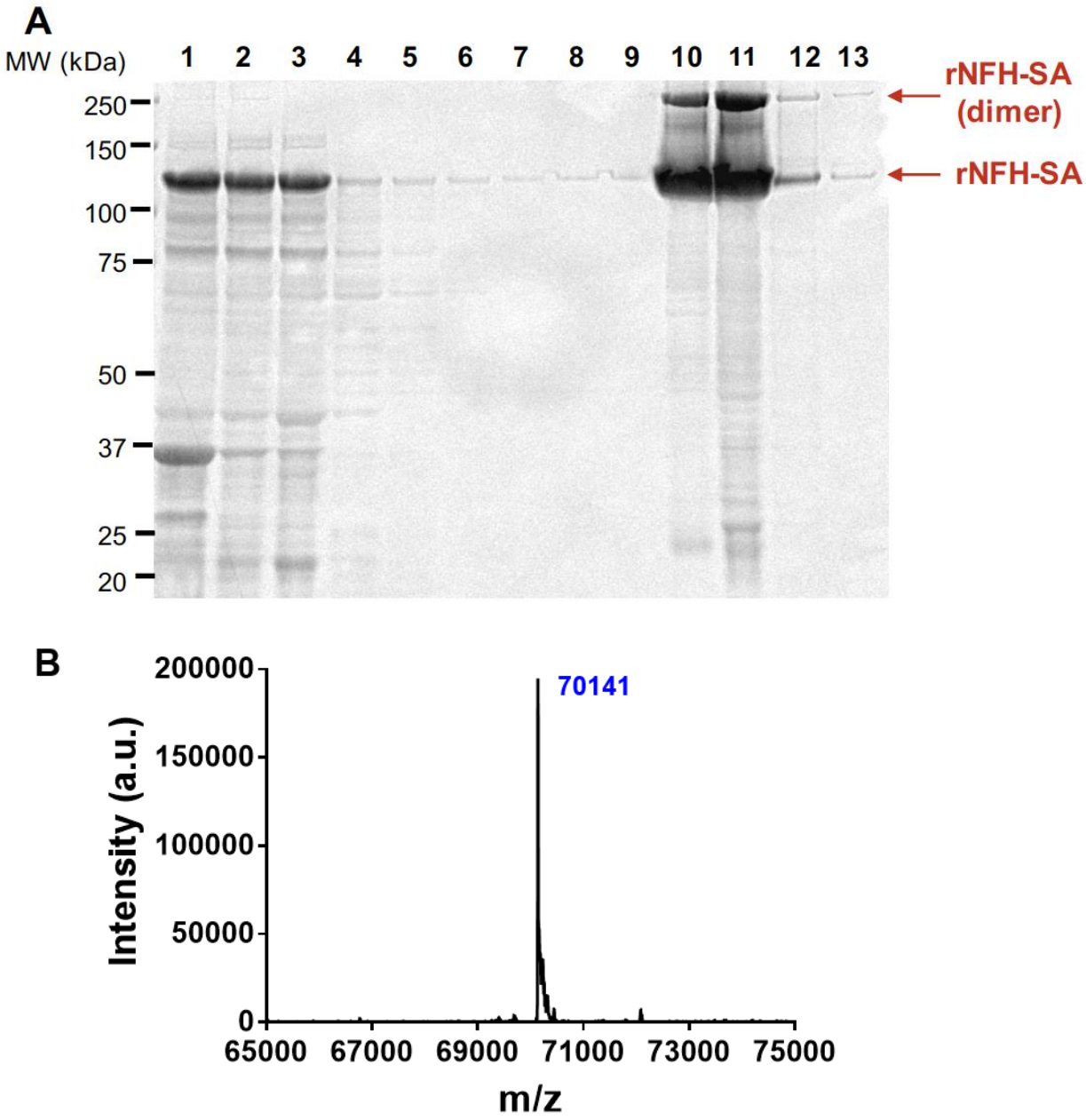

Figure 3.2. Purification of rNFH-SA. (A) Coomassie stained SDS-PAGE illustrating purification of rNFH-SA on HisTrap HP affinity column. Lane 1, crude cellular lysate; lane 2, material collected following application of this lysate to the column; lane 3–8, material collected following column washes with buffer containing 34 mM imidazole; lane 9–13, material eluted following application of buffer containing 250 mM imidazole. (B) Deconvoluted ESI-TOF MS spectra of rNFH-SA. Expected mass of rNFH-SA is 70141 Da.

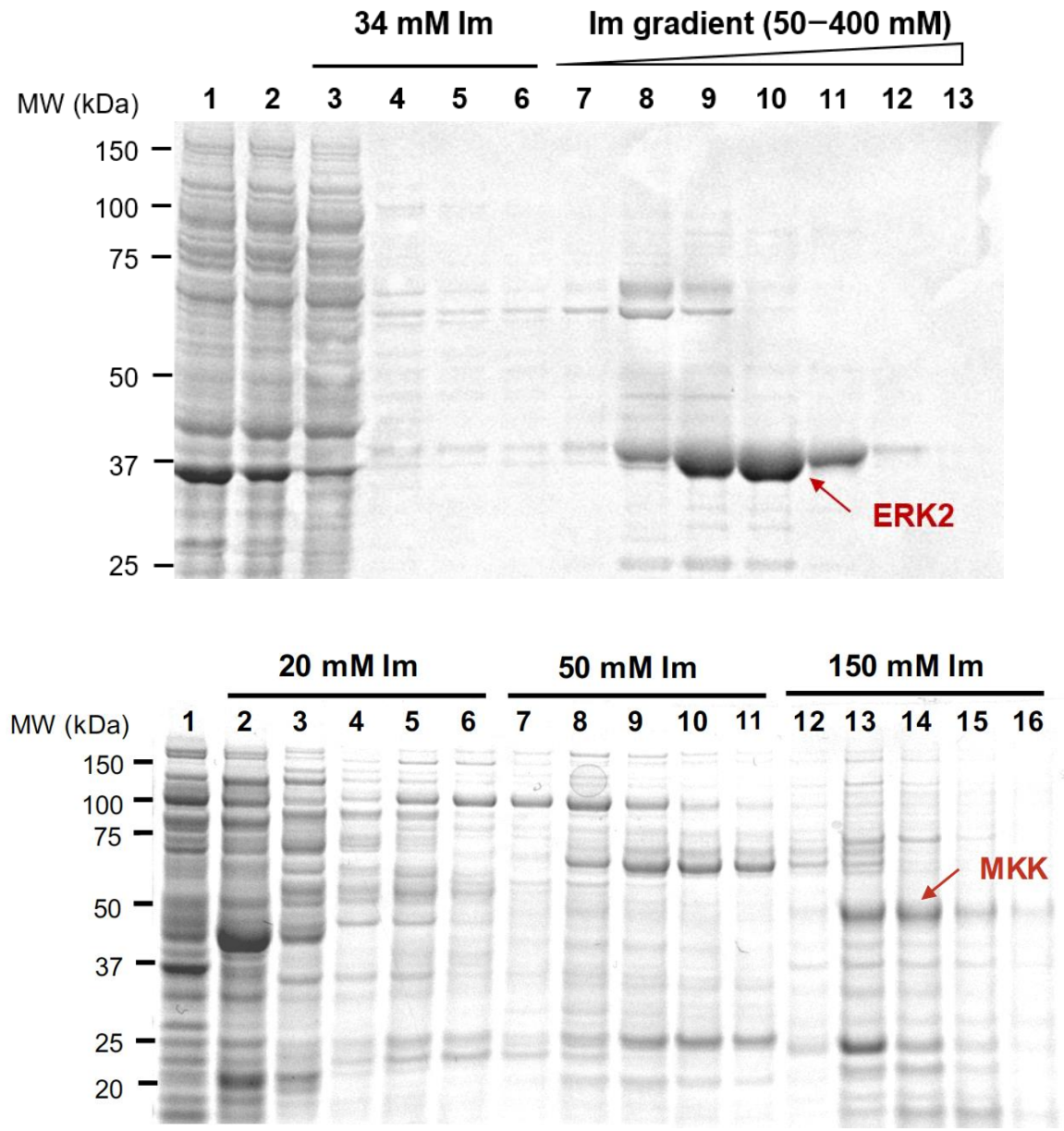

Figure 3.3. Coomassie stained SDS-PAGE illustrating purification of ERK2 (top) and MKK (bottom). Top panel: Lane 1, crude cellular lysate; lane 2, material collected following application of this lysate to the column; lane 3–6, material collected following a series of column washes with buffer containing 34 mM imidazole; lane 7–13, material eluted following application of elution buffer containing a linear gradient of imidazole, increasing from 50 to 400 mM. Bottom panel: Lane 1, material collected following application of this lysate to the column; lane 2–11, material collected following a series of column washes with buffer containing 20 mM or 50 mM imidazole; lane 12–16, material eluted following application of elution buffer containing 150 mM imidazole.

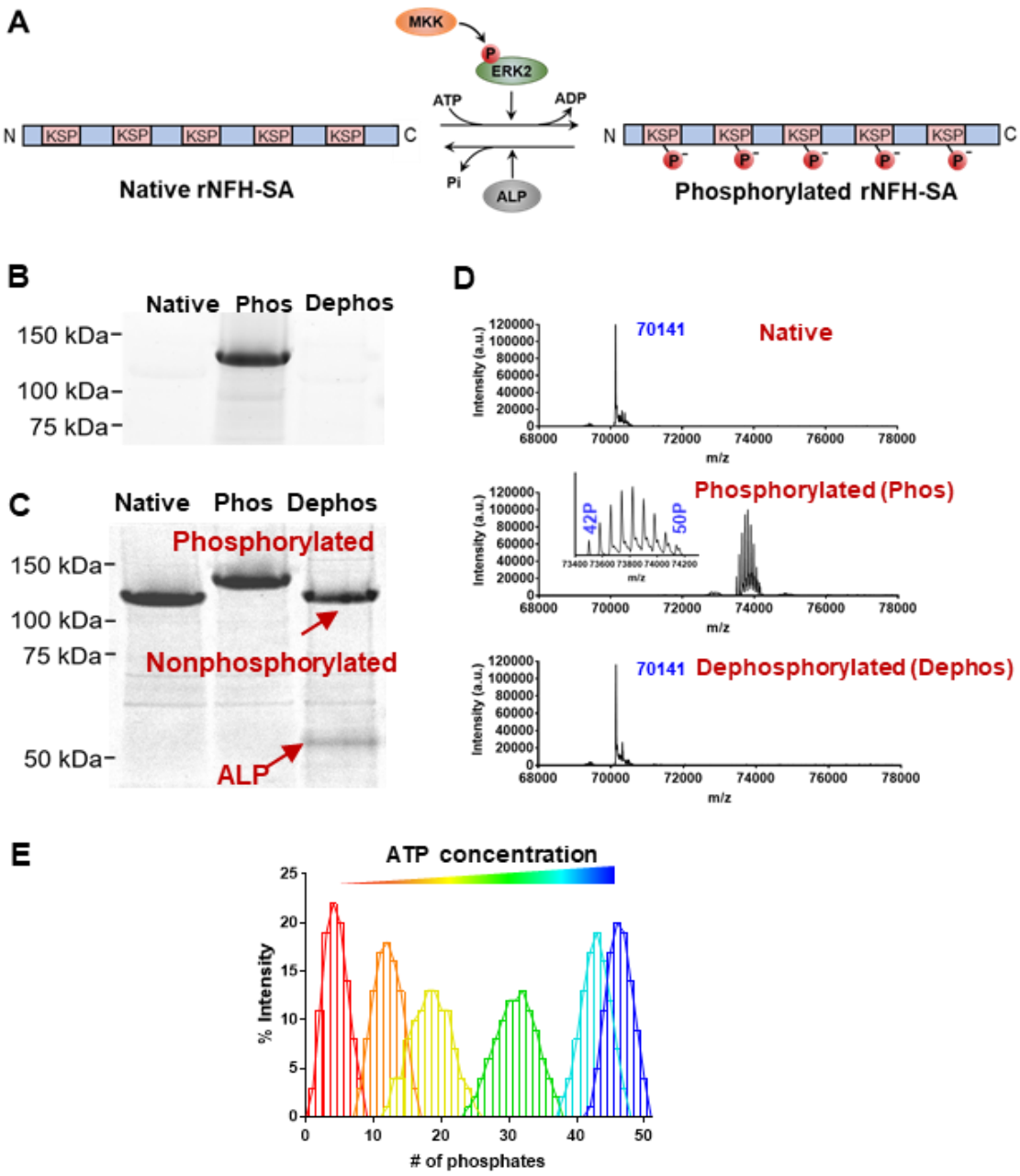

Figure 3.4. Enzymatic phosphorylation of rNFH-SA. (A) Overview of reactions. rNFH-SA was enzymatically phosphorylated using a two-kinase process involving treatment with ERK2 pre-activated with MKK. Dephosphorylation was carried out using alkaline phosphatase (ALP). (B) Phosphoprotein-specific gel electrophoretic analysis of phosphorylation/dephosphorylation. The unmodified protein (Native) does not show phosphorylation, whereas kinase treatment (Phos) produces a band at ~130 kD, a molecular weight significantly higher than native rNFH-SA with the degree consistence with previous studies.[41] (C) LC/MS analysis. Native rNFH-SA (top) produces a peak at the expected molecular weight of 70141 Da. Kinase treatment (middle) produces a population of peaks spanning a range of 73501 to 74139 Da, corresponding to the addition of 42-50 phosphates/chain. Treatment with phosphatase (bottom) led to recovery of the native spectrum. (D) Effect of ATP concentration on extent of phosphorylation. Each color histogram represents the LC/MS-determined distribution of phosphospecies over an ATP

concentration range of 0.125–4.0 mM. While all ATP concentration produce a heterogeneous distribution of phosphospecies, increasing ATP concentration pushes the distribution to higher average levels of phosphorylation.

To validate that ERK2 and MKK may be used to phosphorylate rNFH-SA in solution, we first used MKK to phosphorylate ERK2 in the presence of MgATP, then incubated the reaction mixture with rNFH-SA in phosphorylation buffer overnight (Figure 3.4A). The protein mixture was then analyzed by SDS-PAGE (Figure 3.4B, C) and mass spectrometry (Figure 3.4D). Phospho-specific fluorescence staining of SDS-PAGE gels showed a strongly positive signal for the kinase-treated reaction mixture (Figure 3.4B, 'Phos'), while native rNFH-SA had negligible signal (Figure 3.4B, 'Native'). Kinase treatment of rNFH-SA produced an increase in molecular weight on Coomassie-stained gels (Figure 3.4D), consistent with successful phosphorylation.

LC-MS analysis of the intact protein further confirmed a molecular weight shift of rNFH-SA after kinase treatment and revealed a nearly normal distribution of phosphorylation stoichiometry. The number of phosphorylated sites was proportional to the molar ratio of ATP to rNFH-SA used in the kinase reaction within a certain range, with a ratio of ~ 1400:1 producing an average of ~46 phosphates/chain and in some cases a maximum of 50 phosphates/chain (Figure 3.4E). Increasing ATP concentration beyond this point had a marginal impact on the overall extent of phosphorylation (data not shown). Phosphorylation of Ser residues on KSP repeats was further confirmed by MS analysis of the tryptic digested peptide fragments of phosphorylated rNFH-SA (See 3.6 Supporting Information). We found unique phosphorylated peptides corresponding to each KSP repeat, confirming accessibility of all such repeats to enzymatic phosphorylation. Interestingly, while the majority of phosphorylation occurred on KSP repeats, MS analysis of these peptides also revealed phosphorylation on a few serines or threonine residues other than Ser in KSP repeats (Figure 3.2, highlighted in green), some of which undergo phosphorylation *in vivo* as well.[44]

To examine if rNFH-SA phosphorylation can be reversed by phosphatase treatment, we further incubated the reaction mixture after phosphorylation with calf intestine alkaline phosphatase (ALP). The resulting mixture was again analyzed by SDS-PAGE and MS. Phosphospecific SDS-PAGE showed elimination of the phosphoprotein signal (Figure 3.5B, 'Dephos') and both Coomassie staining and MS showed reversion of the molecular weight to the native value (Figure 3.4C, D). Thus, enzymatic phosphorylation of rNFH-SA is fully reversible in solution.

3.2.3. Phosphorylation Induces Swelling of rNFH-SA Brushes in a pH-dependent Manner

We next probed whether phosphorylation influences the conformational properties of grafted layers of rNFH-SA. We immobilized rNFH-SA on maleimide-functionalized silica coverslip surfaces as described previously[36] and phosphorylated the brush *in situ* using more concentrated ERK2 and MKK (13X concentration compared to in-solution phosphorylation assay) to facilitate enzyme penetration to the interior of the brush. We used a "sandwich" assembly for rNFH-SA immobilization as well as phosphorylation to ensure an identical

grafting density within the same batch of samples. rNFH-SA surfaces treated with kinase mixture lacking ATP were used as a negative control.

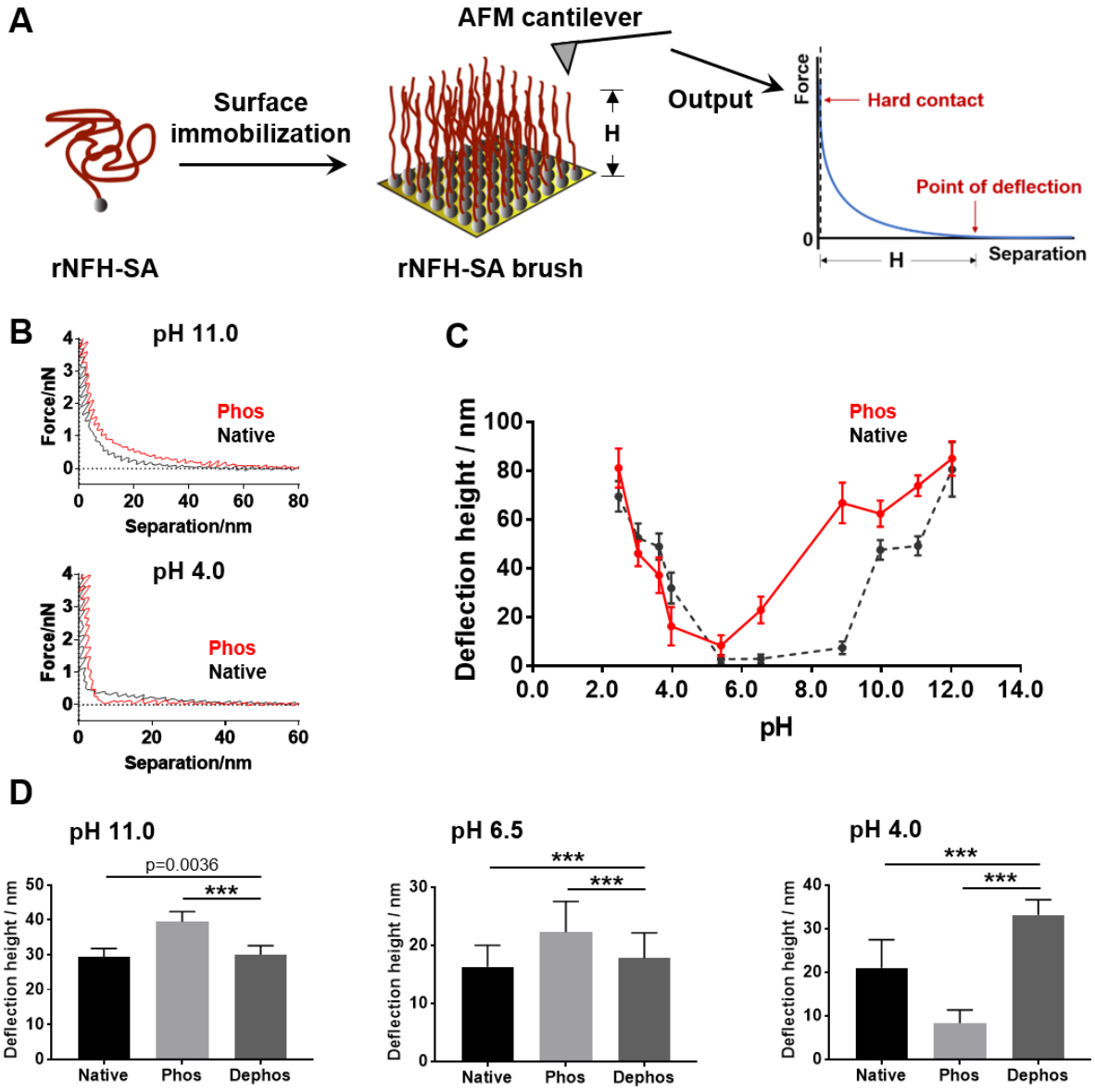

Figure 3.5. Coordinated regulation of rNFH-SA brush height by phosphorylation and pH. (A) Schematic of rNFH-SA brush assembly and AFM brush height measurement. Brush height was extracted from the tip-sample separation difference between the first point of tip deflection and the hard contact point. (B) Representative AFM force-separation curves for native and phosphorylated brushes at pH 4.0 and 11.0. (C) pH-dependence of phosphorylation-induced swelling of rNFH-SA brushes. In the pH range of 6–12, phosphorylated brushes were more swollen than native brushes, while at pH 3.5 and 4.0 phosphorylated brushes were more condensed. (D) Reversibility of conformational effects by alkaline phosphatase (ALP) treatment. ***p<0.005, Student's t-test with Welch's correction. Error bars represent standard error of the mean.

We then applied AFM to measure forces exerted by the IDP brush layer (Figure 3.5A). Force curves were acquired within a 100 μm x 100 μm area with separation distances between force measurements chosen to be much larger than the expected inter-chain spacing distance (estimated to be 7.75 nm based on our previous work).[36] Raw force curves were converted to force-distance curves as previously described, and the brush height was defined as the difference between the scanner position at which that the cantilever starts to deflect and the position at which hard contact is achieved. We initially focused on two pH values: pH 11.0, at which the chain is expected to be strongly anionic due to deprotonation of lysines, glutamates, and phosphates; and pH 4.0, at which the chain is expected to be weakly polycationic due to protonation of both lysine and glutamate as well as incomplete protonation of phosphates.

Notably, the effect of phosphorylation on brush thickness depended strongly on pH, with phosphorylation inducing swelling at pH 11 and partial collapse at pH 4 (Figure 3.5B). To explore this pH regulation further, we compared brush heights for phosphorylated and native brushes over a pH range of 2.5 to 12, covering nominal pKa of glutamate (4.1), lysine (10.7) and phosphoserine (pKa_2, 5.6). We discovered a similar biphasic trend for both phosphorylated and native IDP brushes (Figure 3.5C), in which the brush height rises at both ends of the pH curve and reaches a minimum near neutral pH. However, the phosphorylated rNFH-SA brush was significantly more swollen than the native brush from pH 6.5 to pH 12 (Figure 3.5C), fell to a minimum at pH 4–5, and tracked the native rNFH-SA curve at pH < 3. This phosphorylation-induced difference in pH-dependence is consistent with the idea that phosphorylation converts rNFH-SA from a polyampholyte to a polyelectrolyte, and correspondingly shifts the isoelectric point of the chain.

We next tested whether enzymatically induced rNFH-SA conformational changes could be reversed by enzymatic dephosphorylation. We performed *in situ* dephosphorylation of the IDP brush using an increased ALP concentration and a prolonged reaction time compared to in-solution dephosphorylation. We then chose 3 pH values (4.0, 6.5 and 11.0) under which the phosphorylated rNFH-SA brush exhibited distinct heights. As expected, after dephosphorylation, the brush height changes driven by phosphorylation were largely reversed (Figure 3.5D), consistent with removal of significant numbers of phosphates and strong reversibility of conformational effects.

3.2.4. Phosphorylation-Induced Conformational Changes of rNFH-SA Brushes in Response to Ionic Strength and Divalent Cations

Ionic strength controls the range and strength of electrostatic interactions and has previously been shown to regulate conformational properties of native NFs.[26,31,45] Our previous study with native rNFH-SA also revealed that brush height is sensitive to ionic strength. Specifically, with the increase of ionic strength, the brush first entered a narrow 'osmotic brush regime' in which brush height briefly increased with ionic strength, and then transitioned to a 'salted brush regime' in which height fell with subsequent increases in ionic strength. To further explore the ionic strength-sensitivity of phosphorylated brushes, we conducted AFM measurements on both native and phosphorylated brushes at pH 11.0 over a range of NaCl concentrations. We chose pH 11 to render the brush highly anionic, thereby maximizing electrostatic repulsion between the phosphates. Moreover, at pH 11 the native brush is highly swollen, making it easier to detect subtle changes in brush thickness by AFM.

We observed a monotonic height decrease of both native and phosphorylated brushes over a range of 2–100 mM NaCl (Figure 3.6). With 100 mM NaCl, both brush types condensed to <20% of their original heights under no-salt condition, approaching the sensitivity limit of our measurement (<10 nm).

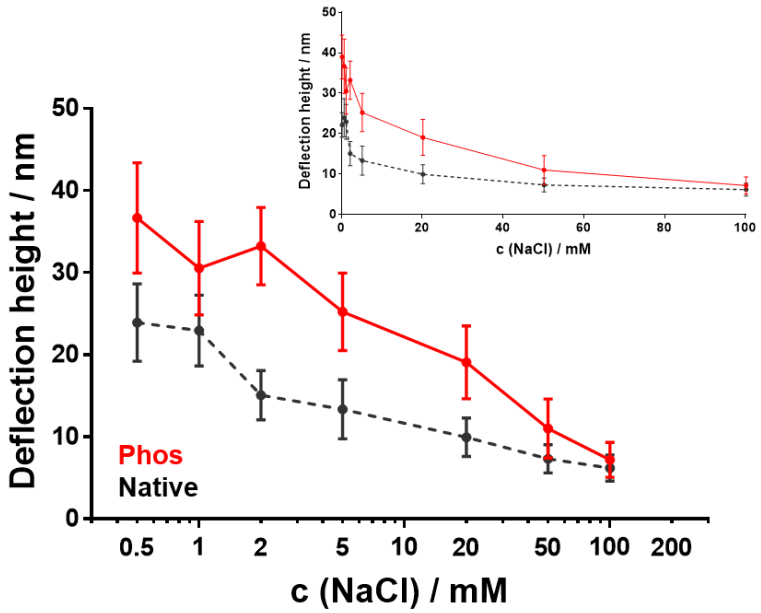

Figure 3.6. Sensitivity of rNFH-SA brushes to ionic strength before and after phosphorylation. Both native and phosphorylated brushes condensed with increasing NaCl concentration in the range of 2–100 mM at pH 11.0. The inset depicts the same data plotted on a linear scale.

The results are in accordance with the 'salted brush' regime in polyelectrolyte theory, in which the negative charges on the protein chains are effectively screened by Na^+ and Cl^-. This similarity in ionic strength sensitivity before and after phosphorylation indicated that both forms of brushes behave like highly-charged polymers that can be analyzed using classical polyelectrolyte theory, qualitatively congruent with the mean-field theory of weak polyelectrolyte brushes.[46]

As a final test of the importance of phosphorylation to controlling conformation, we treated the rNFH-SA brush with divalent cations, which are classically observed to condense polyanionic brushes.[19,47] Divalent cations play an especially important role in NF biology, in that intracellular Ca^{2+} has been reported to control NF axonal transport through strongly phosphorylation-dependent cross-bridging interactions.[20,48] Based on these findings, we hypothesized that divalent cations such as Ca^{2+} and Mg^{2+} might induce a concerted brush condensation, but only when the brush is polyanionic. Phosphorylation would be expected to support a particularly dramatic effect given the ability of multivalent ions to condense phosphate-based polymers (e.g. DNA).[49] We therefore treated native and phosphorylated rNFH-SA brushes at pH 11.0 over a range of $CaCl_2$ and $MgCl_2$ concentrations and measured brush heights by AFM. The average heights of phosphorylated and native brushes in pH 11.0

with no additional salt were used as references ('original height') to quantify following height changes.

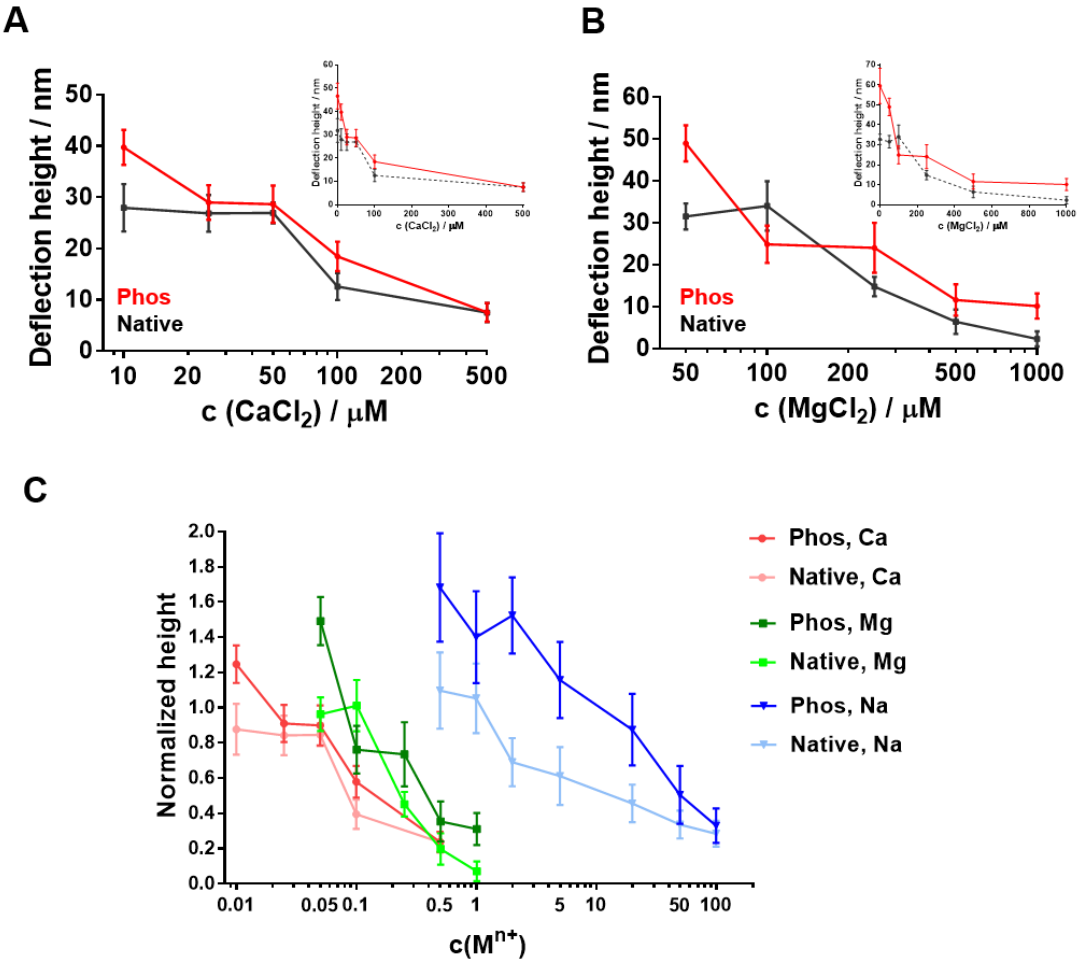

Figure 3.7. Phosphorylation sensitizes rNFH-SA brushes to divalent cations. At pH 11.0, the phosphorylated rNFH-SA brush began to condense at lower Ca^{2+} (A) and Mg^{2+} concentration (B) than the native brush (25 µM vs. 100 µM for Ca^{2+}, 100 µM vs. 250 µM for Mg^{2+}). The insets depict the same data plotted on linear scales at pH 11.0. (C) Summary of all cation responses. Both phosphorylated and native brushes collapsed abruptly in micromolar concentrations of Ca^{2+} or Mg^{2+}, while Na^{+} of the same ionic strength induced only marginal brush condensation. Brush heights are normalized against the average native brush height at pH 11.0, salt-free, from the same experiment, assuming a consistent grafting density. Data for Na^{+} reproduced from Fig. 3.6.

Treatment with 25 µM $CaCl_2$ reduced the height of the phosphorylated brush by 40% relative to its calcium-free state but no effect on the height of the native brush. The thickness of the native brush eventually fell for $CaCl_2$ concentrations greater than 50 µM Ca^{2+}, and then collapsed from ~85% to ~40% of the original height from 50 to 100 µM (Figure 3.7A). A similar trend was observed in the case of $MgCl_2$, in which the phosphorylated brush

collapsed by 60% under 100 μM Mg^{2+} and the native brush collapsed to the same extent at 250 μM Mg^{2+} (Figure 3.7B). There was some quantitative variation in this result from sample to sample, which may be a function of imperfect control of grafting density (see Discussion). Nonetheless, the phosphorylation-dependence of brush condensation remained qualitatively consistent in independent replicates. This condensation is much more significant than that would be predicted by purely electrostatic screening effects. For example, both phosphorylated and native IDP brushes exhibited an 80% reduction from the original height under 500 μM of Ca^{2+} or Mg^{2+}, which corresponds to an ionic strength that is approximately equivalent to that of 1.5 mM NaCl by the Debye-Huckel relationship. However, as our studies with NaCl reveal, the heights of both phosphorylated and native brushes fall only modestly (~30%) with 2 mM NaCl. Therefore, this condensation is attributable to crosslinking of phosphates by the multivalent counterions and is consistent with previous reports on polyanion condensation.[47,50] These results underscore the importance of phosphorylation in regulating IDP conformation.

3.2.5. A Model for Multisite Phosphorylation-Induced rNFH-SA Brush Conformational Changes

The conformational change of phosphorylated rNFH-SA in response to the electrostatic environment is consistent with observed responses for synthetic polymer brush systems and follows classic polyelectrolyte/polyampholyte theory. The biphasic pH-dependence of brush height for both phosphorylated and native brushes reflects the transition between polyampholyte and polyelectrolyte regimes as dictated by the protein's net charge. Additionally, multisite phosphorylation may shift the isoelectric point (pI) of rNFH-SA to more acidic values, as would be expected given the relative values of the theoretically predicted pI for rNFH-SA (5.9) and the pK_{a2} of O-phosphoserine (5.6). This is consistent with our pH-dependence measurements (Figure 3.5C), as the phosphorylated brush reaches maximal condensation at pH 4.0-5.0, whereas the native brush does so at pH 5.0-8.0. Interestingly, brush swelling at basic pH was not observed in our past study on NFH-SA derived phosphomimetic peptide brushes, in which both the native peptide and aspartate-substituted peptide both showed very similar brush height at pH 10.[37] This underscores the idea that phosphomimetic mutations may not fully capture the electrostatic effects of phosphorylation and that observations with short peptides may not be strictly predictive of full-length IDPs.[38]

Phosphorylated brush conformational sensitivity to ionic strength and divalent cations under basic conditions also aligns with past studies on synthetic polyelectrolytes.[35,47] In the presence of divalent cations, rNFH-SA brushes condense at a much lower ionic strength than is observed for monovalent Na^{+}, indicating that the divalents are binding and coordinating the phosphates rather than simply screening them. The enhanced sensitivity to divalent counterions upon brush phosphorylation implies a cross-bridging effect, consistent with the hypothesis that Ca^{2+} can promote inter-filament association among phosphorylated NFs.[26,52] This similarity to phosphorylated NF sidearms *in vivo* shows the ability of our reconstituted brush system to recapitulate NF sidearm interactions. The structure and physical chemistry of phosphate-bearing polyanion synthetic polymers have not been extensively studied, and our brush paradigm may be useful for gaining new insights into such systems.

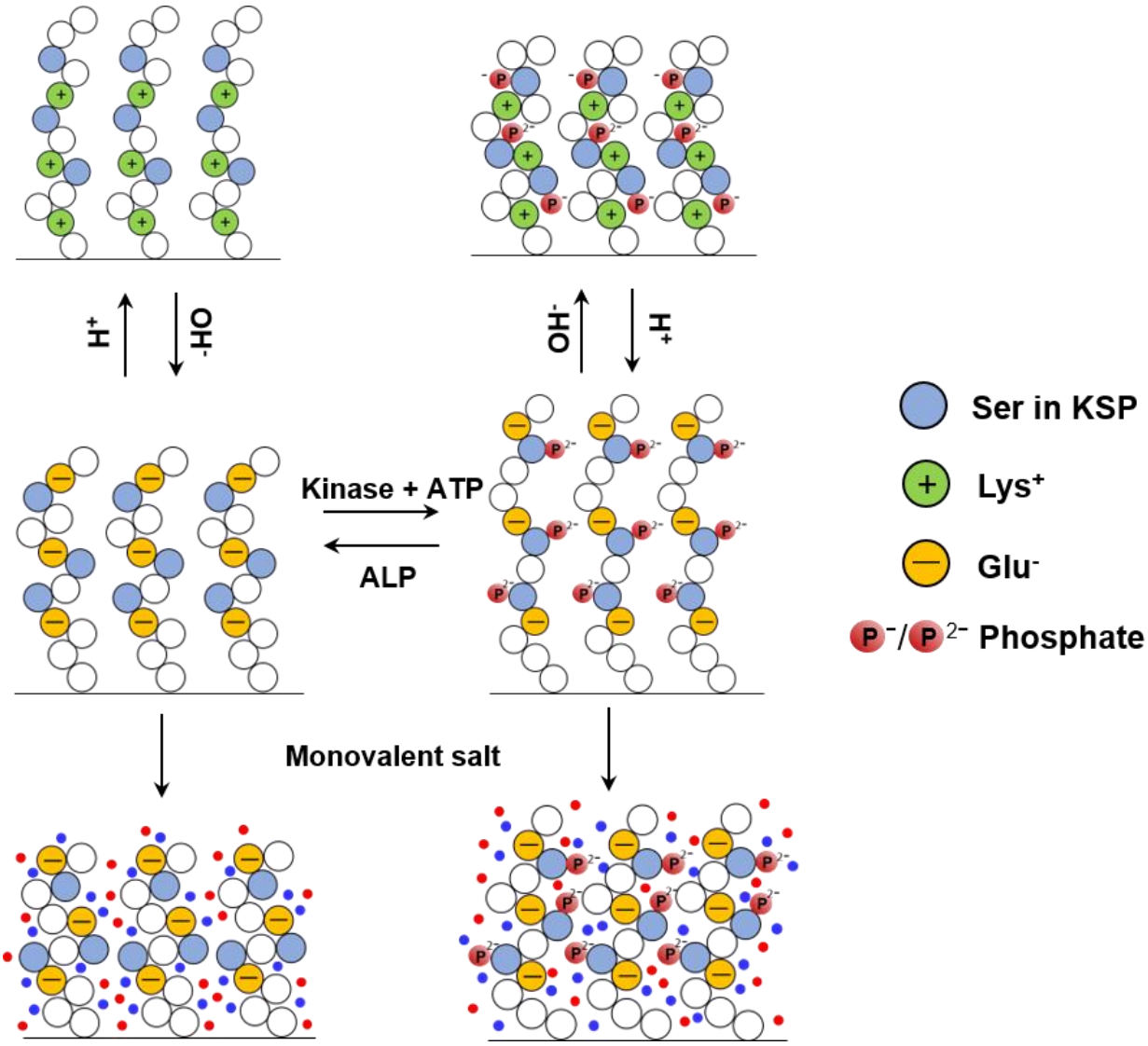

Figure 3.8. A model illustrating multisite phosphorylation-induced rNFH-SA brush conformational change and its pH- (top) and ionic strength- (bottom) dependence. At basic pH, where phosphate groups are fully deprotonated, phosphorylation of rNFH-SA can induce a significant brush swelling effect and increase brush height, while in weakly acidic solution (e.g. pH 4.0), the addition of phosphate groups introduces attraction between phosphates and protonated lysines, reducing brush height. In the presence of monovalent salt, both native and phosphorylated rNFH-SA brushes condense due to charge screening ("salted brush regime"). Blue and red dots represent monovalent cations and anions, respectively.

It is important to note that the structure and responsiveness of any polymer brush will depend strongly on grafting density, with higher grafting densities amplifying both inter- and intra-chain interactions[34]. Whereas grafting densities can be precisely controlled with synthetic polymers by nucleating polymerization from at defined densities on a surface (so-called "grafting from" approaches), the use of IDPs necessitated immobilization of already-

synthesized chains ("grafting to"). This in turn made it challenging to tightly prescribe grafting density from one sample to another, as reflected in the fact that we observed two-fold brush height variations across different samples. For this reason, we swept through the full range of each solution condition (e.g. pH) with a single sample and then normalized across samples. To minimize grafting density differences in native- vs. phosphorylated-comparisons, we used a "sandwich" assembly to equally expose two entire surfaces to the same reaction mixture. Conducting the phosphorylation and dephosphorylation reaction *in situ* also guaranteed consistent grafting densities before and after the reaction. However, the number and position of phosphorylated sites may well be different than those measured in solution, making it challenging to map phosphorylation state to brush conformational properties. One way to overcome this limitation in the future would be to use easily reversible grafting chemistries (e.g. disulfides) or introduce an enzymatic cleavage site close to the grafting point so that proteins can be harvested from the surface for further characterization.

The structural consequences of multisite phosphorylation on IDPs has remained largely unpredictable and can vary drastically among different proteins, which may be a function of the diversity of interactions between phosphorylated residues and neighboring residues. Recently, elegant work from Martin et al.[13] applied NMR spectroscopy to determine that the conformation of the IDP Ash1 is globally insensitive to phosphorylation due to compensatory responses from adjacent proline residues. The dramatic expansion of rNFH-SA brushes upon phosphorylation suggests that electrostatic repulsion overwhelms proline buffering, which may be a consequence of presenting the sequence as a surface-immobilized brush, where inter-IDP interactions contribute strongly to conformational properties. It would be very interesting in the future to develop systems in which brush and solution properties may be compared head-to-head in a more systematic fashion.

3.3 Conclusions

In this chapter, we reported a novel approach to study the effects of multi-phosphorylation on NF-H sidearm conformation by enzymatic phosphorylation and dephosphorylation of surface-immobilized recombinant NF-H sidearm (rNFH-SA) brush. rNFH-SA could be phosphorylated by recombinant ERK2 and MKK and then reversibly dephosphorylated by ALP *in vitro* on serine residues of multiple KSP repeats. Brush height changes characterized by AFM revealed significant brush swelling after phosphorylation, which is highly dependent on environmental stimuli including pH, ionic strength and divalent cation concentration. This swelling effect can be attributed to repulsive forces introduced by phosphate groups, which is in agreement with previous computational modeling[25,26] and experimental results,[19,33,51] describing extension of NF sidearms after phosphorylation.

Our study lends both general insight into how multisite phosphorylation modulates the electrostatic properties of IDPs and more specific insight into mechanisms of NF assembly *in vivo.* We anticipate that our enzymatic modification strategies could be applied to other IDP systems in addition to explore the generality of our findings.

3.4. Materials and Methods

3.4.1. Expression and Purification of rNFH-SA

The IDP expression vector was constructed by modifying the multiple cloning site of pEcoli-Cterm 6×HN vector (Clontech, Cat. No. 631417) to introduce EcoRI and HindIII restriction enzyme recognition sequences, a cysteine near the C-terminus, aromatic residues, thrombin cleavage site and a 6×Histidine tag. The resulting construct was digested with EcoRI-HF and HindIII-HF and subsequently purified. Rat neurofilament heavy protein gene cloned in pClneo with a HindIII restriction enzyme site was excised by ApoI and HindIII-HF digestion. The purified gene insert was then ligated to the doubly digested modified expression vector. Site-directed mutagenesis (QuikChange method adapted from Agilent Technology) was further performed on the resulting modified expression gene to facilitate ribosome binding and to correct reading frame. For simplicity and consistency with our earlier publication,[36] we term the resulting protein rNFH-SA. However, it should be noted that the construct used in the current study has only one C-terminal cysteine, rather than the four N-terminal cysteines our earlier rNFH-SA. The modified rNFH-SA gene was transformed into 5-α *Escherichia coli* (*E. coli*) cells. Plasmids isolated from the resulting transformants were sequenced and the encoded amino acid sequence is shown in Figure S1. rNFH-SA was expressed in *E. coli* Rosetta strain (Novagen) as previously described.[36]

The cell pellet was resuspended in lysis buffer [20 mM Tris-HCl (pH 8.0), 300 mM NaCl, 0.07% (v/v) β-mercaptoethanol, 1.5 mM PMSF, and 10 mM imidazole] and lysed by sonic disruption at 4°C. Insoluble cellular matter was removed by centrifugation and the supernatant was applied to a HisTrap HP Ni^{2+}-NTA affinity column (GE Healthcare) equilibrated with 10 column volumes of 20 mM Tris-HCl (pH 8.0), 300 mM NaCl, and 10 mM imidazole. The column was then washed with 10 column volumes of wash buffer [20 mM Tris (pH 8.0), 300 mM NaCl, 34 mM imidazole] and rNFH-SA was eluted with 5 column volumes of elution buffer [20 mM Tris (pH 8.0), 300 mM NaCl, 250 mM imidazole]. The identity of the eluted protein was verified by SDS-PAGE and LC-MS (ESI-TOF) (6224 TOF and 1200 series HPLC, Agilent Technologies).

3.4.2 Expression and Purification of ERK2 and MKK

6×His-tagged wild type rat ERK2 expression plasmid was a generous gift from Dr. Melanie Cobb (UT Southwestern).[39] The plasmid was transformed into the BL21(DE3) competent *E. coli* strain (New England Biolabs), and protein was expressed as previously described.[39] Cells were harvested after 4 h of induction by centrifugation, and then the cell pellet was resuspended in ERK2 lysis buffer [20 mM Tris-HCl (pH 8.0), 300 mM NaCl, 1.5 mM PMSF, and 10 mM imidazole] and lysed by sonic disruption at 4°C. The clear supernatant obtained from centrifugation was applied to a gravity-flow Ni^{2+}-NTA column equilibrated with 10 column volumes of 20 mM Tris (pH 8.0), 300 mM NaCl, 10 mM imidazole, washed with 10 column volumes of ERK2 wash buffer [20 mM Tris (pH 8.0), 300 mM NaCl, 34 mM imidazole], and ERK2 was eluted using a total of 10 column volumes of elution buffer [20 mM Tris (pH 8.0), 300 mM NaCl, imidazole concentration increasing from 50 to 400 mM].

6×His-tagged human MKK expression plasmid was a generous gift from the laboratory of Dr. Natalie Ahn (U. Colorado). This variant contains phosphorylation site substitutions

S218E and S222D and the deletion of residues 44–51 (DN4).[40] Expression and purification method was modified from Veeranna et al.[39] Specifically, the MKK plasmid was transformed to BL21(DE3) pLysS *E. coli* strain (Promega). Cultures were grown at 30°C to an optical density at 600 nm of 0.6. IPTG was added to a final concentration of 0.1 mM to induce expression and cells were harvested 12-16 h after induction. To purify MKK, cells were lysed in MKK lysis buffer [50mM potassium phosphate (pH 8.0), 10% (v/v) glycerol, 0.25% (v/v) Tween-20, 300 mM NaCl] with 1 mM DTT, 1.5 mM PMSF and 2 mM benzamidine. The cell lysate was sonicated and centrifuged to remove insoluble cell debris before loading to the HisTrap HP column equilibrated with 10 column volumes of MKK lysis buffer with 10 mM imidazole. The column was then washed with 10 column volumes of MKK lysis buffer with 20 mM imidazole and 5 column volumes with 50 mM imidazole. MKK was eluted in lysis buffer with 150 mM imidazole.

3.4.3. In vitro Phosphorylation Assay and Mass Spectrometry Characterization

Phosphorylation protocol was adapted from that of Veeranna et al.[41] First, 1.5 µg of ERK2 was incubated with 0.25 µg of MKK in 20 mM Tris (pH 7.4) and 50 µM MgATP for 2 h at 30 °C. The reaction mix was then incubated with 10 µg rNFH-SA for 14 – 16 h at room temperature in 25 mM Tris (pH 7.4), 2.5 mM $MgCl_2$, 0.05 µM okadaic acid, 0.5 mM EDTA, 0.5 mM EGTA, and 0.5 mM DTT. A final concentration of 0.125~4 mM MgATP was added to achieve different phosphorylation ratio, in a total reaction volume of 50 µL. To dephosphorylate rNFH-SA, a final concentration of 0.5 U/µL of calf intestine alkaline phosphatase (ALP, New England Biolabs) was used to incubate with an aliquot of the reaction mixture at 37 for 2 h. Phosphorylated and dephosphorylated samples were analyzed by SDS-PAGE stained with either ProQ Diamond phosphorylation gel stain (Thermo Fisher Scientific) for phosphoprotein-specific staining, or Coomassie Brilliant Blue R-250 (BioRad Laboratories), following the manufacturer's protocol. MS data of phosphorylated rNFH-SA was collected in the same way as native rNFH-SA.

Upon separation by SDS-PAGE and staining with Coomassie Blue, protein bands were excised from the gels and subject directly to tryptic digest. Tryptic digest was performed according to standard procedures[42] with modifications. Briefly, the gel pieces were dehydrated with acetonitrile (ACN, Fisher Scientific) and then rehydrated with 12.5 ng/µl Pierce™ Trypsin Protease (Thermo Fisher Scientific) in 25 mM NH_4HCO_3 buffer and incubated 2 h at 37°C. Peptides were extracted with 50% ACN, 45% H_2O and 5% formic acid, and concentrated in a vacuum centrifuge. The samples were further analyzed by liquid chromatography-tandem mass spectrometry (LC-MS/MS) using a Dionex UltiMate 3000 RSLCnano LC system that was connected in line with an LTQ-Orbitrap-XL mass spectrometer equipped with an electrospray ionization (ESI) source (Thermo Fisher Scientific; QB3/Chemistry Mass Spectrometry Facility, UC Berkeley). Data analysis to identify tryptic peptides and phosphorylation sites was performed using Proteome Discoverer software (version 1.3, Thermo).

3.4.4. *In situ* Phosphorylation and Dephosphorylation of rNFH-SA Immobilized Brushes

Functionalization of borosilicate glass coverslips (Fisherbrand™ Cover Glasses, Fisher Scientific) and rNFH-SA immobilization were performed as previously described.[36] For *in*

situ phosphorylation, ERK2 and MKK were applied at ~13X concentrations relative to values used for phosphorylation in solution. Specifically, for a 20 µL reaction, 8.4 µg ERK2 and 1.4 µg MKK were incubated for 2 h at 30 °C in 25 mM Tris (pH 7.4), 2.5 mM $MgCl_2$, 0.05 µM okadaic acid, 0.5 mM EDTA, 0.5 mM EGTA, 0.5 mM DTT and 2 mM MgATP. The reaction mixture was then placed between two rNFH-SA immobilized surfaces. An equal volume of reaction mixture without MgATP was used as a negative control. The samples were allowed to react 16-20 h at room temperature and then rinsed with deionized H_2O containing 1 mM EDTA and 1 mM EGTA, and then deionized H_2O adjusted to pH 11. To dephosphorylate the samples, 5 U/µL calf intestine alkaline phosphatase was incubated between two surfaces at 37°C or room temperature for 16 h, and then rinsed with deionized H_2O containing 1 mM EDTA and 1 mM EGTA, and then deionized H_2O adjusted to pH 11.

3.4.5. AFM Characterization of Brush Conformations

AFM was performed with a Veeco Catalyst Bioscope (Bruker Corporation, Camarillo, California, USA) using MLCT-BIO A cantilevers, with spring constants determined by thermal tuning. The experimental setup was based on our earlier publication[36] and used an open cell arrangement with a wetted tip brought into contact with samples fully submerged in solution. Typically, at least 200 force curves per coverslip were collected over 100 µm with 2,048 data points per curve, at a rate of 2.0 Hz. Relative triggers of up to 4 nN were used to minimize tip-surface damage. When exchanging solutions of different conditions, both the sample and tip were rinsed with several milliliters of the new solution prior to a measurement. The brush height was extracted as previously described based on the difference between the piezo positions at initial deflection and hard contact.[36] All results were qualitatively reproduced across at least 3 experimental replicates (i.e., independent surfaces).

3.5. References

(1) Dunker, A. K., Bondos, S. E., Huang, F., and Oldfield, C. J. (2015) Intrinsically disordered proteins and multicellular organisms, *Semin. Cell Dev. Biol. 37*, 44–55.

(2) Levine, Z. A., Larini, L., LaPointe, N. E., Feinstein, S. C., and Shea, J.-E. (2015) Regulation and aggregation of intrinsically disordered peptides, *Proc. Natl. Acad. Sci. U.S.A. 112*, 2758–2763.

(3) Theillet, F.-X., Binolfi, A., Frembgen-Kesner, T., Hingorani, K., Sarkar, M., Kyne, C., Li, C., Crowley, P. B., Gierasch, L., Pielak, G. J., Elcock, A. H., Gershenson, A., and Selenko, P. (2014) Physicochemical Properties of Cells and Their Effects on Intrinsically Disordered Proteins (IDPs), *Chem. Rev. 114*, 6661–6714.

(4) Bah, A., Vernon, R. M., Siddiqui, Z., Krzeminski, M., Muhandiram, R., Zhao, C., Sonenberg, N., Kay, L. E., and Forman-Kay, J. D. (2015) Folding of an intrinsically disordered protein by phosphorylation as a regulatory switch, *Nature 519*, 106–109.

(5) Mukhopadhyay, H., de Wet, B., Clemens, L., Maini, P. K., Allard, J., van der Merwe, P. A., and Dushek, O. (2016) Multisite Phosphorylation Modulates the T Cell Receptor ζ-Chain Potency but not the Switchlike Response, *Biophys. J. 110*, 1896–1906.

(6) Brangwynne, C. P., Eckmann, C. R., Courson, D. S., Rybarska, A., Hoege, C., Gharakhani, J., Jülicher, F., and Hyman, A. A. (2009) Germline P Granules Are Liquid Droplets That Localize by Controlled Dissolution/Condensation, *Science 324*, 1729–1732.

(7) Rosenbaum, J. C., Fredrickson, E. K., Oeser, M. L., Garrett-Engele, C. M., Locke, M. N., Richardson, L. A., Nelson, Z. W., Hetrick, E. D., Milac, T. I., Gottschling, D. E., and Gardner, R. G. (2011) Disorder targets misorder in nuclear quality control degradation: a disordered ubiquitin ligase directly recognizes its misfolded substrates, *Mol. Cell 41*, 93–106.

(8) Bah, A., and Forman-Kay, J. D. (2016) Modulation of Intrinsically Disordered Protein Function by Post-translational Modifications, *J. Biol. Chem. 291*, 6696–6705.

(9) Wu, R., Haas, W., Dephoure, N., Huttlin, E. L., Zhai, B., Sowa, M. E., and Gygi, S. P. (2011) A large-scale method to measure absolute protein phosphorylation stoichiometries, *Nat. Methods 8*, 677-683.

(10) Amata, I., Maffei, M., Igea, A., Gay, M., Vilaseca, M., Nebreda, A. R., and Pons, M. (2013) Multi-phosphorylation of the Intrinsically Disordered Unique Domain of c-Src Studied by In-Cell and Real-Time NMR Spectroscopy, *ChemBioChem 14*, 1820–1827.

(11) Kulkarni, P., Jolly, M. K., Jia, D., Mooney, S. M., Bhargava, A., Kagohara, L. T., Chen, Y., Hao, P., He, Y., Veltri, R. W., Grishaev, A., Weninger, K., Levine, H., and Orban, J. (2017) Phosphorylation-induced conformational dynamics in an intrinsically disordered protein and potential role in phenotypic heterogeneity, *Proc. Natl. Acad. Sci. U.S.A. 114*, E2644-E2653.

(12) Liu, B., Chia, D., Csizmok, V., Farber, P., Forman-Kay, J. D., and Gradinaru, C. C. (2014) The Effect of Intrachain Electrostatic Repulsion on Conformational Disorder and Dynamics of the Sic1 Protein, *J. Phys. Chem. B 118*, 4088–4097.

(13) Martin, E. W., Holehouse, A. S., Grace, C. R., Hughes, A., Pappu, R. V., and Mittag, T. (2016) Sequence Determinants of the Conformational Properties of an Intrinsically Disordered Protein Prior to and upon Multisite Phosphorylation, *J. Am. Chem. Soc. 138*, 15323–15335.

(14) Rout, M. P., Aitchison, J. D., Suprapto, A., Hjertaas, K., Zhao, Y., and Chait, B. T. (2000) The Yeast Nuclear Pore Complex: Composition, Architecture, and Transport Mechanism, *J. Cell Biol. 148*, 635–652.

(15) Schoch, R. L., Kapinos, L. E., and Lim, R. Y. H. (2012) Nuclear transport receptor binding avidity triggers a self-healing collapse transition in FG-nucleoporin molecular brushes, *Proc. Natl. Acad. Sci. U.S.A. 109*, 16911–16916.

(16) Janmey, P. A., Leterrier, J.-F., and Herrmann, H. (2003) Assembly and structure of neurofilaments, *Curr. Opin. Colloid Interface Sci. 8*, 40–47.

(17) Yuan, A., Rao, M. V., Veeranna, and Nixon, R. A. (2012) Neurofilaments at a glance, *J. Cell Sci. 125*, 3257–3263.

(18) Brown, H. G., and Hoh, J. H. (1997) Entropic Exclusion by Neurofilament Sidearms: A Mechanism for Maintaining Interfilament Spacing, *Biochemistry 36*, 15035–15040.

(19) Kumar, S., and Hoh, J. H. (2004) Modulation of repulsive forces between neurofilaments by sidearm phosphorylation, *Biochem. Biophys. Res. Commun. 324*, 489–496.

(20) Shea, T. B., and Chan, W. K.-H. (2008) Regulation of neurofilament dynamics by phosphorylation, *Eur. J. Neurosci. 27*, 1893–1901.

(21) Laser-Azogui, A., Kornreich, M., Malka-Gibor, E., and Beck, R. (2015) Neurofilament assembly and function during neuronal development, *Curr. Opin. Cell Biol. 32*, 92–101.

(22) Ackerley, S., Grierson, A. J., Banner, S., Perkinton, M. S., Brownlees, J., Byers, H. L., Ward, M., Thornhill, P., Hussain, K., Waby, J. S., Anderton, B. H., Cooper, J. D., Dingwall, C., Leigh, P. N., Shaw, C. E., and Miller, C. C. J. (2004) p38α stress-activated protein kinase phosphorylates neurofilaments and is associated with neurofilament pathology in amyotrophic lateral sclerosis, *Mol. Cell. Neurosci. 26*, 354–364.

(23) Hu, Y.-Y., He, S.-S., Wang, X.-C., Duan, Q.-H., Khatoon, S., Iqbal, K., Grundke-Iqbal, I., and Wang, J.-Z. (2002) Elevated levels of phosphorylated neurofilament proteins in cerebrospinal fluid of Alzheimer disease patients, *Neurosci. Lett. 320*, 156–160.

(24) Zhulina, E. B., and Leermakers, F. A. M. (2007) Effect of the Ionic Strength and pH on the Equilibrium Structure of a Neurofilament Brush, *Biophys. J. 93*, 1452–1463.

(25) Stevenson, W., Chang, R., and Gebremichael, Y. (2011) Phosphorylation-Mediated Conformational Changes in the Mouse Neurofilament Architecture: Insight from a Neurofilament Brush Model, *J. Mol. Biol. 405*, 1101–1118.

(26) Lee, J., Kim, S., Chang, R., Jayanthi, L., and Gebremichael, Y. (2013) Effects of molecular model, ionic strength, divalent ions, and hydrophobic interaction on human neurofilament conformation, *J. Chem. Phys. 138*, 015103.

(27) Aranda-Espinoza, H., Carl, P., Leterrier, J.-F., Janmey, P., and Discher, D. E. (2002) Domain unfolding in neurofilament sidearms: effects of phosphorylation and ATP, *FEBS Lett. 531*, 397–401.

(28) Lee, S., Sunil, N., and Shea, T. B. (2011) C-terminal neurofilament phosphorylation fosters neurofilament–neurofilament associations that compete with axonal transport, *Cytoskeleton 68*, 8–17.

(29) Shea, T. B., and Lee, S. (2011) Neurofilament phosphorylation regulates axonal transport by an indirect mechanism: A merging of opposing hypotheses, *Cytoskeleton 68*, 589–595.

(30) Stevens, M. J., and Hoh, J. H. (2011) Interactions between Planar Grafted Neurofilament Side-Arms, *J. Phys. Chem. B 115*, 7541–7549.

(31) Rammensee, S., Janmey, P. A., and Bausch, A. R. (2007) Mechanical and structural properties of in vitro neurofilament hydrogels, *Eur. Biophys. J. 36*, 661–668.

(32) Safinya, C. R., Deek, J., Beck, R., Jones, J. B., and Li, Y. (2015) Assembly of Biological Nanostructures: Isotropic and Liquid Crystalline Phases of Neurofilament Hydrogels, *Annu. Rev. Condens. Matter Phys. 6*, 113–136.

(33) Malka-Gibor, E., Kornreich, M., Laser-Azogui, A., Doron, O., Zingerman-Koladko, I., Medalia, O., and Beck, R. (2016) Phosphorylation-induced mechanical regulation of intrinsically disordered neurofilament protein assemblies, *Biophys. J. 112*, 892-900.

(34) Lego, B., Skene, W. G., and Giasson, S. (2010) Swelling Study of Responsive Polyelectrolyte Brushes Grafted from Mica Substrates: Effect of pH, Salt, and Grafting Density, *Macromolecules 43*, 4384–4393.

(35) Dehghani, E. S., Ramakrishna, S. N., Spencer, N. D., and Benetti, E. M. (2017) Controlled Crosslinking Is a Tool To Precisely Modulate the Nanomechanical and Nanotribological Properties of Polymer Brushes, *Macromolecules 50*, 2932–2941.

(36) Srinivasan, N., Bhagawati, M., Ananthanarayanan, B., and Kumar, S. (2014) Stimuli-sensitive intrinsically disordered protein brushes, *Nat. Commun. 5*, 5145.

(37) Bhagawati, M., Rubashkin, M. G., Lee, J. P., Ananthanarayanan, B., Weaver, V. M., and Kumar, S. (2016) Site-Specific Modulation of Charge Controls the Structure and Stimulus Responsiveness of Intrinsically Disordered Peptide Brushes, *Langmuir 32*, 5990–5996.

(38) Ng, Y.-W., Raghunathan, D., Chan, P. M., Baskaran, Y., Smith, D. J., Lee, C.-H., Verma, C., and Manser, E. (2010) Why an A-Loop Phospho-Mimetic Fails to Activate PAK1: Understanding an Inaccessible Kinase State by Molecular Dynamics Simulations, *Structure 18*, 879–890.

(39) Robbins, D. J., Zhen, E., Owaki, H., Vanderbilt, C. A., Ebert, D., Geppert, T. D., and Cobb, M. H. (1993) Regulation and properties of extracellular signal-regulated protein kinases 1 and 2 in vitro, *J. Biol. Chem. 268*, 5097–5106.

(40) Mansour, S. J., Candia, J. M., Matsuura, J. E., Manning, M. C., and Ahn, N. G. (1996) Interdependent Domains Controlling the Enzymatic Activity of Mitogen-Activated Protein Kinase Kinase 1, *Biochemistry 35*, 15529–15536.

(41) Veeranna, Niranjana D. Amin, Natalie G. Ahn, Jaffe, H., Winters, C. A., Grant, P., and Pant, H. C. (1998) Mitogen-Activated Protein Kinases (Erk1,2) Phosphorylate Lys-Ser-Pro (KSP) Repeats in Neurofilament Proteins NF-H and NF-M, *J. Neurosci. 18*, 4008–4021.

(42) Shevchenko, A., Tomas, H., Havlis, J., Olsen, J. V., and Mann, M. (2006) In-gel digestion for mass spectrometric characterization of proteins and proteomes, *Nat. Protoc. 1*, 2856–2860.

(43) Lee, S., Pant, H. C., and Shea, T. B. (2014) Divergent and convergent roles for kinases and phosphatases in neurofilament dynamics, *J. Cell Sci. 127*, 4064–4077.

(44) Lundby, A., Secher, A., Lage, K., Nordsborg, N. B., Dmytriyev, A., Lundby, C., and Olsen, J. V. (2012) Quantitative maps of protein phosphorylation sites across 14 different rat organs and tissues, *Nat. Commun. 3*, 876.

(45) Beck, R., Deek, J., Choi, M. C., Ikawa, T., Watanabe, O., Frey, E., Pincus, P., and Safinya, C. R. (2010) Unconventional Salt Trend from Soft to Stiff in Single Neurofilament Biopolymer, *Langmuir 26*, 18595–18599.

(46) Pincus, P. (1991) Colloid stabilization with grafted polyelectrolytes, *Macromolecules 24*, 2912–2919.

(47) Yu, J., Mao, J., Yuan, G., Satija, S., Jiang, Z., Chen, W., and Tirrell, M. (2016) Structure of Polyelectrolyte Brushes in the Presence of Multivalent Counterions, *Macromolecules 49*, 5609–5617.

(48) Kushkuley, J., Chan, W. K. H., Lee, S., Eyer, J., Leterrier, J.-F., Letournel, F., and Shea, T. B. (2009) Neurofilament cross-bridging competes with kinesin-dependent association of neurofilaments with microtubules, *J. Cell Sci. 122*, 3579–3586.

(49) Graham, F. L., and van der Eb, A. J. (1973) A new technique for the assay of infectivity of human adenovirus 5 DNA, *Virology 52*, 456–467.

(50) Brettmann, B., Pincus, P., and Tirrell, M. (2017) Lateral Structure Formation in Polyelectrolyte Brushes Induced by Multivalent Ions, *Macromolecules 50*, 1225–1235.

(51) Kumar, S., Yin, X., Trapp, B. D., Hoh, J. H., and Paulaitis, M. E. (2002) Relating Interactions between Neurofilaments to the Structure of Axonal Neurofilament Distributions through Polymer Brush Models, *Biophys. J. 82*, 2360–2372.

(52) Gou, J. P., Gotow, T., Janmey, P. A., and Leterrier, J. F. (1998) Regulation of neurofilament interactionsin vitro by natural and synthetic polypeptides sharing Lys-Ser-Pro sequences with the heavy neurofilament subunit NF-H: Neurofilament crossbridging by antiparallel sidearm overlapping, *Med. Biol. Eng. Comput. 36*, 371–387.

3.6. Supporting Information

Table 3.1. Tryptic-digested peptide fragments detected from MS analysis (with 1 mM ATP)

Note: S – serine, s – phosphoserine, T – threonine, t – phosphothreonine, m – methionine sulfoxide

Sequence	Sequence
AAAPEEETPAK	SPAEAKsPVEVK
AEEKEPLTEKPK	sPAEAKsPVEVKsPASVK
AEEKEPLTEKPKDSPGEAK	SPAEAKsPVEVKsPASVK
AEEKEPLTEKPKDSPGEAKK	SPAEAKsPVEVKSPASVK
AEEKEPLTEKPKDsPGEAKKEEAK	SPAEAKsPVEVKsPASVKsPSEAK
AEEKEPLTEKPKDSPGEAKKEEAK	SPAEAKsPVEVKsPASVKsPsEAKSPAGAK
AEEKEPLTEKPKDSPGEAKKEEAKEK	SPAEAKsPVEVKsPEK
AKEEDKGLPQEPSKPK	SPAEAKsPVEVKSPEK
AKEPPKKVEEEK	SPAEAKsPVEVKsPEKAK
AKEPPKKVEEEKTPAtPK	SPAEAKsPVEVKsPEKAKsPVKEGAK
AKEPPKKVEEEKTPAtPKTEVK	SPAEAKsPVVAK
AKEPSKPSEK	SPAEAKsPVVAKsPAEAK
AKEPSKPSEKEKPK	SPAEAKsPVVAKsPAEAKsPAEAKPPAEAK
AKsPmKEEAK	SPAEVKsPAEAK
AKSPmKEEAK	SPAEVKsPAEAKsPAEAK
AKsPmKEEAKSPEK	SPAEVKsPAEAKsPAEAKsPAEVKsPATVK
AKSPmKEEAKSPEK	SPAEVKsPAEVK
AKSPmKEEAKsPEKAK	sPAEVKsPAEVKsPAEAK
AKsPVKEEIKPPAEVK	SPAEVKsPAEVKsPAEAK
AKSPVKEEIKPPAEVK	SPAEVKsPAEVKSPAEAK
AKSPVKEEIKPPAEVKsPEK	sPAEVKsPATVK
AKSPVKEEIKPPAEVKSPEK	SPAEVKsPATVK

AKSPVKEEIKPPAEVKsPEKAK	SPAEVKsPATVKsPGEAK
AKsPVKEGAK	SPAEVKsPATVKsPVEAK
DSPGEAKKEEAK	sPAEVKSPATVKsPVEAKsPAEVKsPVTVK
DSQPSEK	SPAEVKsPAVAK
DTKEEK	SPAEVKsPAVAKsPAEVK
EEAKSPEKEETRTEK	SPAEVKsPAVAKsPAEVKsPAEVK
EEDKGLPQEPSKPK	SPAEVKsPAVAKsPAEVKSPAEVK
EEIKPPAEVK	SPAEVKsPAVAKsPAEVKsPAEVKSPAEAK
EKAEDAK	SPAEVKsPVEAK
EKPKKEEVPAAPEK	SPAEVKsPVEAKsPAEAK
EKPKKEEVPAAPEKK	SPAEVKSPVEAKsPAEAK
ESKKDEAPK	SPAEVKsPVEAKsPAEAKsPASVK
ESKKDEAPKEAQKPK	SPAEVKsPVEAKsPAEAKsPASVKsPGEAK
GSWSHPQFEK	sPAEVKsPVTVK
IKVVEK	SPAEVKsPVTVK
KAAAPEEETPAK	SPAGAKsPAEAK
KAAAPEEEtPAKLGVKEEAKPK	SPAGAKsPAEAKsPVVAK
KDEAPKEAQKPK	SPAGAKsPAEAKsPVVAKsPAEAK
KEEVKsPVEEVK	SPAKEEAK
KEEVKSPVEEVK	SPAKEEAKsPEKEETR
KEEVKsPVEEVKAK	SPAKEEAKSPEKEETR
KEEVPAAPEK	SPAKEEAKsPEKEETRTEK
KEEVPAAPEKK	SPAKEEAKSPEKEETRTEK
KEEVPAAPEKKDTKEEK	SPAVAKsPAEVKsPAEVKsPAEAK
KPEEKPK	SPEAKtPAKEEAK
KVEEEK	SPEKEETR
KVEEEKTPAtPK	SPEKEETRTEK
KVEEEKTPATPK	SPEQVKsPAKEEAK
KVEEEKtPAtPKTEVK	SPEQVKSPAKEEAK
KVEEEKtPATPKTEVK	SPEQVKsPAKEEAKsPEKEETR
LGVKEEAKPK	SPEQVKsPAKEEAKSPEKEETR
RPADIR	SPEQVKsPAKEEAKsPEKEETRTEK
RPADIRsPEQVK	SPGEAKsPAEAK
RPADIRsPEQVKsPAKEEAK	SPGEAKsPAEAKsPAEVKsPATVK
RPADIRsPEQVKSPAKEEAK	SPGEAKsPAEAKsPAEVKsPVEAK
RPADIRsPEQVKsPAKEEAKSPEKEETR	SPmKEEAK
SEEKIK	SPmKEEAKSPEK
SEFtSmSTHIK	SPmKEEAKsPEKAK
SEFTSmSTHIK	SPSEAKsPAGAK
SLAEAKsPEK	SPVEAKsPAEAK
SLAEAKsPEKAK	SPVEAKsPAEAKsPASVK
SPAEAKPPAEAK	SPVEAKsPAEAKsPAsVKSPGEAK
SPAEAKPPAEAKsPAEAK	SPVEAKsPAEVKsPVTVK
SPAEAKPPAEAKsPAEAKsPAEAK	SPVEAKsPAEVKsPVTVKsPAEAK
SPAEAKPPAEAKsPAEAKSPAEAK	SPVEEVK
SPAEAKsPAEAK	sPVEEVKAK
sPAEAKsPAEAKPPAEAK	SPVEEVKAK

SPAEAKsPAEAKPPAEAK	SPVEEVKAKEPPK
SPAEAKsPAEAKPPAEAKsPAEAK	SPVEVKsPASVK
SPAEAKsPAEAKPPAEAKsPAEAKsPAEAK	SPVEVKsPASVKsPSEAK
SPAEAKsPAEAKPPAEAKsPAEAKSPAEAK	SPVEVKsPASVKsPSEAKsPAGAK
SPAEAKsPAEAKsPAEAK	SPVEVKsPEKAK
SPAEAKsPAEAKSPAEAK	sPVKEEAK
SPAEAKsPAEAKsPAEAKsPAEAKsPVEVKSPEK	SPVKEEAK
SPAEAKsPAEAKsPAEAKsPAEVKsPAVAK	sPVKEEAKsPAEAK
SPAEAKsPAEAKsPAEAKsPVEVK	SPVKEEAKsPAEAK
SPAEAKsPAEAKSPAEAKsPVEVK	sPVKEEAKsPAEAKsPAEAK
SPAEAKsPAEAKsPAEAKsPVEVKSPEK	SPVKEEAKsPAEAKsPAEAK
SPAEAKsPAEAKsPAEVK	SPVKEEAKsPAEAKSPAEAK
SPAEAKsPAEAKsPAEVKsPATVK	SPVKEEAKsPAEAKsPAEAKsPAEAK
SPAEAKsPAEAKsPAEVKsPATVKsPGEAK	SPVKEEIKPPAEVK
SPAEAKsPAEAKsPAEVKsPAVAK	SPVKEEIKPPAEVKsPEK
SPAEAKsPAEAKsPVEVK	SPVKEEIKPPAEVKSPEK
SPAEAKsPAEAKSPVEVK	SPVKEEIKPPAEVKsPEKAK
SPAEAKsPAEAKsPVEVKSPEK	SPVKEEIKPPAEVKsPEKAKsPmKEEAK
SPAEAKsPAEAKsPVEVKsPEKAK	SPVKEGAK
SPAEAKsPAEVK	SPVTVKsPAEAK
sPAEAKsPAEVKsPATVK	SPVVAKsPAEAK
SPAEAKsPAEVKsPATVK	SPVVAKsPAEAKsPAEAKPPAEAK
SPAEAKsPAEVKSPATVK	SSSTDQKDSQPSEK
SPAEAKsPAEVKsPATVKsPGEAK	SSSTDQKDSQPSEKAPEDK
SPAEAKsPAEVKSPAtVKsPGEAKsPAEAK	TLDVKsPEAK
SPAEAKsPAEVKsPATVKsPVEAK	TLDVKSPEAK
SPAEAKsPAEVKsPAVAK	TLDVKsPEAKtPAKEEAK
SPAEAKsPAEVKsPAVAKsPAEVK	TLDVKSPEAKtPAKEEAK
SPAEAKsPAEVKsPAVAKsPAEVKsPAEVK	TPAKEEAK
SPAEAKsPAEVKsPVEAK	TPAtPKTEVK
SPAEAKsPAEVKSPVEAK	TTESKKPEEKPKmEAK
SPAEAKsPAEVKsPVEAKsPAEAK	VEEEKTPAtPKTEVK
SPAEAKsPAEVKsPVEAKsPAEAKsPASVK	VKSEEK
SPAEAKsPASVK	VVEKSEK
SPAEAKsPASVKsPGEAK	

Table 3.2. Tryptic-digested peptide fragments detected from MS analysis (with 4 mM ATP)

Note: S – serine, s – phosphoserine, T – threonine, t – phosphothreonine, m – methionine sulfoxide

Sequence	**Sequence**
AAAPEEETPAK	SPAEAKsPAEAKPPAEAK
AEEKEPLTEKPK	SPAEAKsPAEAKPPAEAKsPAEAK
AEEKEPLTEKPKDsPGEAK	SPAEAKsPAEAKPPAEAKsPAEAKsPAEAK
AEEKEPLTEKPKDSPGEAK	SPAEAKsPAEAKsPAEAK
AEEKEPLTEKPKDsPGEAKK	SPAEAKsPAEAKsPAEAKsPAEVKsPAVAK

AEEKEPLTEKPKDSPGEAKK	SPAEAKsPAEAKsPAEAKsPVEVK
AEEKEPLTEKPKDsPGEAKKEEAK	SPAEAKsPAEAKsPAEAKsPVEVKSPEK
AEEKEPLTEKPKDSPGEAKKEEAK	SPAEAKsPAEAKsPAEAKsPVEVKsPEKAK
AEEKEPLTEKPKDSPGEAKKEEAKEK	SPAEAKsPAEAKsPAEVKsPAVAK
AKEEDKGLPQEPSKPK	SPAEAKsPAEAKsPVEVK
AKEPPKKVEEEK	SPAEAKsPAEAKsPVEVKsPEK
AKEPPKKVEEEKTPAtPK	SPAEAKsPAEAKsPVEVKSPEK
AKEPPKKVEEEKtPAtPKTEVK	SPAEAKsPAEAKsPVEVKsPEKAK
AKEPPKKVEEEKTPAtPKTEVK	SPAEAKsPAEAKsPVEVKsPEKAKsPVKEGAK
AKEPSKPSEK	sPAEAKsPAEVKsPATVK
AKsPmKEEAK	SPAEAKsPAEVKsPATVK
AKSPmKEEAK	sPAEAKsPAEVKSPAtVKsPVEAK
AKsPmKEEAKSPEK	SPAEAKsPAEVKsPATVKsPVEAK
AKSPmKEEAKSPEK	SPAEAKsPAEVKsPAVAK
AKsPmKEEAKsPEKAK	SPAEAKsPAEVKsPVEAK
AKSPmKEEAKsPEKAK	SPAEAKsPAEVKsPVEAKsPAEAK
AKsPVKEEIKPPAEVK	SPAEAKsPAEVKsPVEAKsPAEAKsPASVK
AKSPVKEEIKPPAEVK	SPAEAKsPASVK
AKSPVKEEIKPPAEVKsPEK	SPAEAKsPVEVK
AKSPVKEEIKPPAEVKSPEK	SPAEAKsPVEVKSPEK
AKsPVKEEIKPPAEVKsPEKAK	SPAEAKsPVEVKsPEKAKsPVKEGAK
AKSPVKEEIKPPAEVKsPEKAK	SPAEAKsPVVAK
AKsPVKEEIKPPAEVKsPEKAKsPmKEEAK	SPAEAKsPVVAKsPAEAK
AKSPVKEEIKPPAEVKsPEKAKsPmKEEAK	SPAEAKsPVVAKsPAEAKsPAEAKPPAEAK
AKsPVKEGAK	SPAEVKSPAtVKsPGEAKsPAEAKsPAEVK
DSPGEAKKEEAK	sPAEVKsPATVKsPVEAK
DSPGEAKKEEAKEK	SPAEVKsPVEAKsPAEAKsPASVK
DTKEEK	sPAGAKsPAEAKsPVVAK
DTKEEKTTESK	SPAGAKsPAEAKsPVVAK
DTKEEKTTESKKPEEKPK	SPAKEEAK
EEAKSPEKEETRTEK	SPAKEEAKsPEKEETR
EEDKGLPQEPSKPK	SPAKEEAKSPEKEETR
EKAEDAK	SPAKEEAKsPEKEETRTEK
EKAEDAKAK	SPAKEEAKSPEKEETRTEK
EKPKKEEVPAAPEK	SPEAKtPAKEEAK
EKPKKEEVPAAPEKK	SPEKEETR
ESKKDEAPK	SPEKEETRTEK
ESKKDEAPKEAQKPK	SPEQVKsPAKEEAK
EtKsPVKEEAKsPAEAKSPAEAKsPAEAK	SPEQVKSPAKEEAK
GSWSHPQFEK	SPEQVKsPAKEEAKsPEKEETR
IKVVEK	SPEQVKsPAKEEAKSPEKEETR
KAAAPEEETPAK	SPEQVKsPAKEEAKSPEKEETRTEK
KAAAPEEEtPAKLGVK	SPEQVKSPAKEEAKSPEKEETRTEK
KAAAPEEEtPAKLGVKEEAKPK	sPGEAKsPAEAKsPAEVKsPVEAK
KDEAPKEAQKPK	SPmKEEAK
KEEVKsPVEEVK	SPmKEEAKSPEK
KEEVKSPVEEVK	SPmKEEAKsPEKAK

KEEVKsPVEEVKAK	SPVEEVK
KEEVKsPVEEVKAKEPPK	sPVEEVKAK
KEEVPAAPEK	SPVEEVKAK
KEEVPAAPEKK	sPVKEEAK
KEEVPAAPEKKDTKEEK	SPVKEEAK
KPEEKPK	sPVKEEAKsPAEAK
KPEEKPKmEAK	SPVKEEAKsPAEAK
KVEEEK	sPVKEEAKsPAEAKsPAEAK
KVEEEKTPAtPK	sPVKEEAKsPAEAKsPAEAKsPAEAK
KVEEEKtPAtPKTEVK	SPVKEEIKPPAEVK
KVEEEKTPAtPKTEVK	SPVKEEIKPPAEVKsPEK
LGVKEEAKPK	SPVKEEIKPPAEVKSPEK
RPADIR	SPVKEEIKPPAEVKsPEKAK
RPADIRsPEQVK	SPVKEEIKPPAEVKsPEKAKsPmKEEAK
RPADIRsPEQVKsPAKEEAK	SPVKEEIKPPAEVKsPEKAKsPmKEEAKSPEK
RPADIRsPEQVKSPAKEEAK	sPVKEGAK
RPADIRsPEQVKsPAKEEAKsPEKEETR	SPVKEGAK
RPADIRsPEQVKsPAKEEAKSPEKEETR	sPVVAKsPAEAKsPAEAKPPAEAK
RPADIRSPEQVKsPAKEEAKSPEKEEtRtEK	SPVVAKsPAEAKsPAEAKPPAEAK
SEFtSmSTHIK	SSSTDQKDSQPSEK
SEFTSmSTHIK	SSSTDQKDSQPSEKAPEDK
SEFTSMSTHIK	TEKAEK
SLAEAKsPEK	TLDVKsPEAK
SLAEAKsPEKAK	TLDVKSPEAK
SLAEAKsPEKAKsPVKEEIKPPAEVK	TLDVKsPEAKtPAKEEAK
SLAEAKsPEKAKsPVKEEIKPPAEVKsPEK	TLDVKSPEAKtPAKEEAK
SLAEAKsPEKAKsPVKEEIKPPAEVKsPEKAK	TPAKEEAK
sPAEAKPPAEAK	TPAtPKTEVK
SPAEAKPPAEAK	TTESKKPEEKPKmEAK
SPAEAKPPAEAKsPAEAK	VAPKKEEVKsPVEEVK
SPAEAKPPAEAKsPAEAKsPAEAK	VEEEKTPAtPKTEVK
SPAEAKsPAEAK	VKSEEK
sPAEAKsPAEAKPPAEAK	VVEKSEK